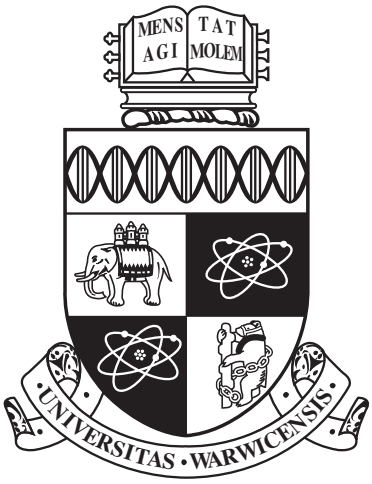

Advanced Modelling and Signal Processing in Nonlinear Coherent Optical Fibre Systems

by

Cenqin Jin

Thesis

Submitted to the University of Warwick

for the degree of

Doctor of Philosophy

School of Engineering

May 2023

THE UNIVERSITY OF WARWICK

Contents

List of Tables

List of Figures

Acknowledgments

To start with, I would like to express my heartfelt appreciation to my supervisor, Dr. Tianhua Xu, for providing me with unwavering support throughout my doctoral research, as well as for his professional guidance and generosity. Additionally, I would like to extend my thanks to my supervisor, Prof. Yunfei Chen, for his kind assistance. Without their expert advice and knowledge, completing this thesis would not have been achievable.

Furthermore, I am extremely thankful to my colleagues in the School of Engineering at University of Warwick who taught me various topics related to my research, including digital signal processing and digital communication. In particular, I owe a debt of gratitude to Dr. Nikita A. Shevchenko for his extensive knowledge of the Gaussian noise model and assistance in overcoming some challenging mathematical obstacles.

Above everything else, I am profoundly grateful to my family for their unwavering support throughout this journey. This thesis would not have been possible without their assistance.

Declarations

This thesis is submitted in partial fulfillment for the degree of Doctor of Philosophy under the regulations set out by the University of Warwick. This thesis contains research solely completed by Cenqin Jin under the supervision of Dr. Tianhua Xu and Prof. Yunfei Chen, except the parts stated. This dissertation has not been used in any form previously for a degree at other universities.

List of Publications

Journal Papers

- Jin, C., Shevchenko, N.A., Wang, J., Chen, Y., Xu, T. (2023). Wideband multichannel Nyquist-spaced long-haul optical transmission influenced by enhanced equalization phase noise. Sensors, 23(3), 1493.

- Jin, C., Shevchenko, N. A., Li, Z., Popov, S., Chen, Y., and Xu, T. (2021). Nonlinear coherent optical systems in the presence of equalization enhanced phase noise. Journal of Lightwave Technology, 39(14), 4646-4653.

- Liu, Z., Xu, T., Jin, C., Xu, T., Tan, M., Zhao, J., and Liu, T. (2022). Analytical optimization of wideband nonlinear optical fiber communication systems. Optics Express, 30(7), 11345-11359.

- Xu, T., Shevchenko, N. A., Zhang, Y., Jin, C., Zhao, J., and Liu, T. (2021). Information rates in Kerr nonlinearity limited optical fiber communication systems. Optics Express, 29(11), 17428-17439.

- Ding, J., Xu, T., Jin, C., Wang, Z., Zhao, J., and Liu, T., (2020) Impact of equalization-enhanced phase noise on digital nonlinearity compensation in high-capacity optical communication systems, Sensors, 20(15), 4149.

- Xu, T., Jin, C., Zhang, S., Jacobsen, G., Popov , S., Leeson, M., and Liu, T., (2019). Phase noise cancellation in coherent communication systems using a radio frequency pilot tone, Applied Sciences, 9(21), 4717.

Conference Papers

- Jin, C., Tan, M., Chen, Y., and Xu, T. (2022, November).Kalman filter based impairment mitigation in nonlinear optical systems with equalization enhanced phase noise. In 2022 IEEE Photonics Conference (IPC). IEEE.

- Jin, C., Tan, M., Shevchenko, N. A., Liu, Z., Li, Z., Popov, S., Chen, Y., and Xu, T. (2022, July). High-speed long-haul multi-channel nonlinear optical communication systems influenced by equalization enhanced phase noise. In 2022 14th International Conference on Advanced Infocomm Technology (ICAIT). IEEE.

- Ding, J., Xu, T., Zhang, Y., Liu, Z., Jin, C., Zhao, J., and Liu, T. (2021, October). Influence of equalization enhanced phase noise on digital nonlinearity compensation in Nyquist-spaced superchannel transmission systems. In Semiconductor Lasers and Applications XI (Vol. 11891, pp. 38-45). SPIE.

Under Preparation

- Jin, C., Tan, M., Shevchenko, N. A., Liu, Z., Leeson, M. S., Chen, Y., and Xu, T. (2023).Kalman filters in long-haul nonlinear terrestrial and submarine optical communication systems.

Abstract

The importance of optical fibres in the global information society has increased significantly over the past four decades. However, the ever-growing demand for high-capacity data transmission poses a significant challenge, as the fibre channel's nonlinear properties limit the achievable capacities, spectral efficiencies, and distances. This thesis aims to address this challenge by investigating advanced modelling and signal processing in nonlinear coherent optical fibre systems to predict and improve overall system performance.

The first part of the thesis examines the effectiveness of nonlinear compensation (NLC) techniques, such as digital back-propagation (DBP) and optical phase conjugation (OPC), in enhancing achievable information rates (AIRs) in C-band systems that use both EDFA and distributed Raman amplification. Results indicate that the effectiveness of NLC techniques in enhancing AIRs depends heavily on the signal modulation formats and target transmission distances, with NLC being more effective for higher-order modulation formats at shorter system distances. The second part investigates the performance of long-haul Nyquist-spaced wavelength division multiplexing (WDM) optical communication systems with electronic dispersion compensation (EDC) and digital NLC with significant laser linewidths, and presents an analytical model based on the Gaussian noise model to predict the system performance considering the impact of equalisation enhanced phase noise (EEPN). A reduction up to 1.41 dB in SNR was observed in a 32-GBd 2000-km 5-channel system using NLC due to EEPN. This thesis also conducts a comprehensive analysis to study the performance of Kalman filter (KF) under realistic long-haul optical link conditions. The effectiveness of the KF in mitigating phase distortions has been thoroughly analysed. Numerical simulations were conducted on both dispersion-unmanaged and dispersion-managed nonlinear long-haul transmission systems. The joint application of KF and NLC significantly improved system performance, achieving approximately 4 dB higher SNRs than pilot-aided CPE. The findings of this thesis could help advance the design of nonlinear coherent optical fibre systems influenced by laser phase noise for high-capacity data transmission.

Abbreviations

ADC	Analogue-Digital Converter
ASE	Amplifier Spontaneous Emission
AWGN	Additive White Gaussian Noise
BER	Bit Error Rate
BPS	Blind Phase Search
BTB	Back-to-Back
CD	Chromatic Dispersion
CPE	Carrier Phase Estimator
CPR	Carrier Phase Recovery
CW	Continuous Wave
CMOS	Complementary Metal-Oxide-Semiconductor
DAC	Digital-to-Analogue Converter
DBP	Digital Back-Propagation
DCF	Dispersion Compensating Fibre
DFB	Distributed Feedback
DP-QPSK	Dual-Polarisation Quadrature Phase Shift Keying

DP-16QAM	Dual-Polarisation 16-*ary* Quadrature Amplitude Modulation
DRA	Distributed Raman Amplifier
DSP	Digital Signal Processing
ECL	External Cavity Lasers
EDC	Electronic Dispersion Compensation
EDFA	Erbium-Doped Fibre Amplifier
EEPN	Equalisation Enhanced Phase Noise
EOM	Electro-Optic Modulator
FDE	Frequency Domain Equalizer
FEC	Forward-Error-Correction
FFT	Fast Fourier Transform
FF	Full-Field
FIR	Finite-Impulse-Response Filter
FWM	Four-Wave Mixing
GN	Gaussian Noise
GVD	Group-Velocity Dispersion
IFFT	Inverse Fast Fourier Transform
KF	Kalman Filter
LED	Light-Emitting Diode
LO	Local Oscillator
LPN	Laser Phase Noise

MMA	Multiple Modulus Algorithm
MSE	Mean-Squared Error
MZM	Mach-Zehnder Modulator
M-PSK	M-ary Phase Shift Keying
NLC	Nonlinearity Compensation
NLI	Nonlinear Interference
NPS	Nyquist Pulse Shaping
NLSE	Nonlinear Schrödinger Equation
ODC	Optical Dispersion Compensation
OPC	Optical Phase Conjugation
PA	Pilot-Aided
PBC	Polarisation Beam Combiner
PBS	Polarisation Beam Splitter
PDM	Polarisation Division Multiplexing
PM	Polarisation-Multiplexed
PMD	Polarisation Mode Dispersion
PRBS	Pseudo Random Bit Sequence
PSD	Power Spectral Density
QAM	Quadrature Amplitude Modulation
QPSK	Quadrature Phase Shift Keying
RRC	Root-Raised Cosine

Rx	Receiver
SNR	Signal-to-Noise Ratio
SPM	Self-Phase Modulation
SSFM	Split-Step Fourier Method
SSMF	Standard Single Mode Fiber
TOD	Third Order Dispersion
TRx	Transceiver
Tx	Transmitter
VV	Viterbi-Viterbi
WDM	Wavelength-Division Multiplexing
XPM	Cross-Phase Modulation

Chapter 1

Introduction

1.1 Development of Optical Fibre Communication

Optical communication refers to the technology that uses light to transmit information. Optical fibre communication systems rely on light passing through optical fibres. Since 1980, optical fibre communication systems have been deployed worldwide, and optical communication has made great strides. Today, it is one of the most effective and reliable means of communication.

The use of optical fibres was initially limited to short-distance applications such as endoscopes when they were first developed in the 1960s [1]. The fibres available at the time had high losses and were therefore unsuitable for long-distance communication, which required the transmission of light over several kilometres. In 1966, it was proposed that by purifying the silica glass used to make the fibres, their losses could be greatly reduced, and Charles Kao and George Hockham suggested the use of glass fibres for long-distance infor-

mation transmission [2]. A paper published by three scientists from Corning in 1970 reported that they were able to reduce the losses in fiber to less than 20 dB·km^{-1} at a wavelength of approximately 630 nm [3]. In 1979, a Japanese group further reduced fibre losses to nearly 0.2 dB·km^{-1} at a wavelength of 1.55 μm [4]. Additionally, a compact and efficient semiconductor laser that can modulate information for transmission on low-loss optical fibres is necessary. GaAs semiconductor lasers were demonstrated by two Russian groups [5] and Bell Labs [6] around the time that Corning announced their low-loss optical fibre.

The availability of compact light sources and optical fibres with low transmission losses prompted efforts to develop optical fibre communication systems worldwide. Since the 1970s, the adoption of optical fibres in communication has grown exponentially. In the 1980s, the progress made in optical transmission was significantly boosted by the development of optical amplifiers. These are used to amplify optical signals without converting them to electrical signals. This allows signals to be transmitted over longer distances and at higher data rates. The development of wavelength-division multiplexing (WDM) in the 1990s was another major advance in optical transmission. WDM technology permits the transmission of multiple signals with various wavelengths over a single fibre. This increases the bandwidth of optical fibres and allows multiple data streams to be transmitted simultaneously. In WDM systems, erbium-doped fibre amplifiers (EDFAs), which were developed after 1985 and commercialised in 1990, are periodically employed for loss compensation, greatly increasing the transmission distance and making intercontinental communication possible. Submarine cables now connect all continents and allow large amounts of data to be transmitted between countries. Fig. 1.1 [7]

shows the global submarine cable deployment of optical fibre communication systems around 2015.

During the latter half of the 20th century, the development of lasers, optical fibres, and optical amplifiers completely changed optical transmission. The progress of WDM, submarine fibre optic cables, and coherent optical communications has made it possible to transmit large amounts of data over long distances. Taking into account the benefits of high bandwidth, resistance to electromagnetic interference, and low attenuation, optical fibre communications have become an indispensable part of modern life and is expected to maintain its crucial role in future communication technologies.

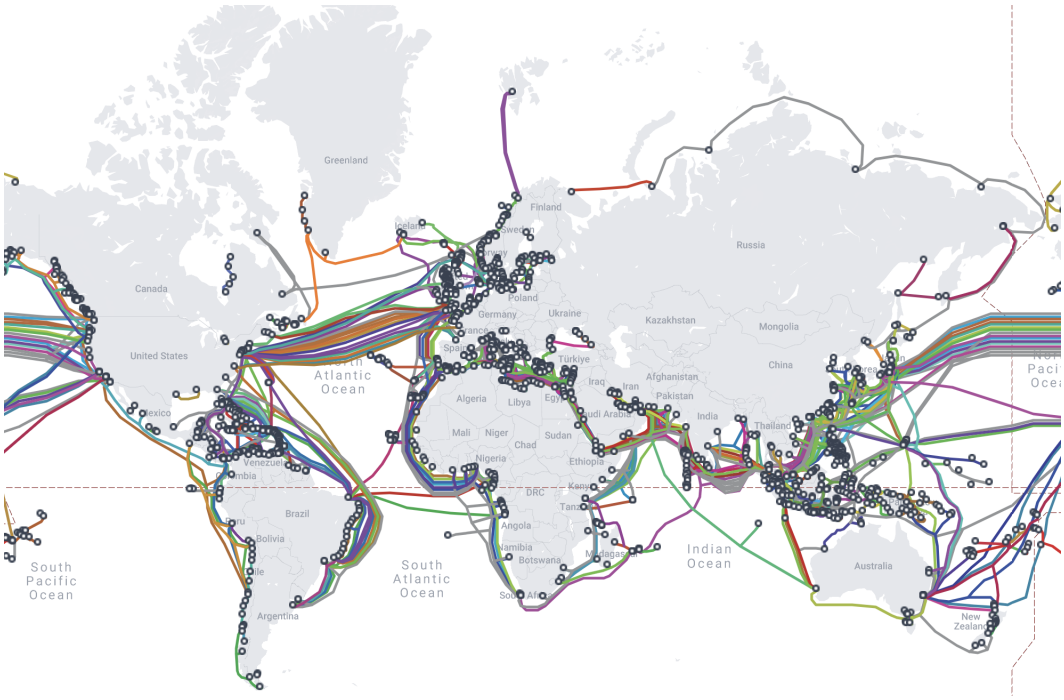

Figure 1.1: Global submarine cable deployment of optical fibre communication systems [7].

1.2 Issues and Challenges

1.2.1 Optical Transmission Capacity Crunch

The past four decades have witnessed an incredible development in optical fibres, which serve as the foundation of the worldwide information society. Single-mode fibres, which are utilized in current commercial systems, are capable of transmitting data rates exceeding 10 Tb/s per fibre. They are extensively used in global communication infrastructure and carry more than 95% of the world's Internet traffic [8, 9]. Moreover, they constitute an essential element in the backbone networks for both mobile telephony and the Internet.

Recently, demands on high-capacity data transmission have drastically increased [8, 10]. The ever-growing demand for capacity poses higher requirements for optical transmission systems. To meet the requirements, Nyquist-spaced transmission is implemented to enhance spectral efficiencies, as well as optical signal distortions are strictly mitigated to ensure sufficient signal quality. However, the optical fibre channel is nonlinear, that is, its properties, namely its refractive index, are dependent on optical intensity, and at high power densities, the combination of nonlinear effects and dispersion leads to nonlinear distortion, limiting both achievable capacities, spectral efficiencies, and distances. Despite the fibre nonlinearity, optical fibre system performance can be adversely affected by a variety of factors such as amplifier spontaneous emission (ASE) noise, chromatic dispersion (CD), transceiver (TRx) noise, equalisation enhanced phase noise (EEPN), laser phase noise (LPN) and polarisation mode dispersion (PMD). These factors can lead to signal distortion, degradation, and inter-symbol interference, which can impact overall system performance. To be specific, the performance of an uncompensated optical

transmission system can be severely suppressed by CD, PMD, LPN, EEPN, ASE noise, nonlinear interference (NLI) due to the optical Kerr effect, as well as signal-EEPN and signal-ASE noise interactions [11–19]. In the case of dispersion-compensated submarine systems, the transmitted signals can be seriously distorted by PMD, LPN, ASE noise, NLI, and signal-ASE noise interaction, since CD has been compensated by dispersion compensating fibres (DCFs) within the transmission links [20]. Therefore, given the importance of meeting the demands of high-capacity data transmission, there is a need for continued research on advanced modelling and signal processing in nonlinear coherent optical fibre systems that can predict overall system performance and mitigate the impacts of these distortions.

1.2.2 Modelling of Nonlinear Optical Systems

The development of advanced modelling techniques for nonlinear coherent optical fibre systems can help researchers to gain a better understanding of the complex interactions between the signal and the fibre. These interactions can be modelled using various techniques such as the nonlinear Schrödinger equation (NLSE) [21], which provides a comprehensive description of the propagation of optical signals in a fibre. The NLSE takes into account the effects of CD, nonlinearity, and attenuation, which are the main factors that affect signal transmission in optical fibres. The NLSE can be solved by employing the split-step Fourier method, which involves dividing the fibre into small sections and applying the Fourier transform to each section. This technique enables researchers to simulate the propagation of optical signals in a fibre over a long distance and to study the impact of various factors such as dispersion,

nonlinearity, and attenuation on signal transmission.

Although the split-step Fourier method of the NLSE is accurate and widely used for numerical simulations, analytical models have been used to evaluate and predict the performance of coherent optical transmission systems for its simplicity and convenience. Among them, the family of GN models (see, e.g., [22–24]) has become popular owing to its sufficiently accurate prediction and relatively low complexity. This model assumes that the NLI is additive GN, and the signal itself is also assumed to be Gaussian due to the significant dispersion accumulation after a long-distance transmission. Modern coherent optical fibre communications can satisfy the above assumptions in most cases. For ease of calculation, [25–28] proposed the closed-form expression of the GN model. In recent years, the GN model has also been continuously developed and studied for applications in more specific scenarios [29–35]. [35] proposed the inter-channel stimulated Raman scattering (ISRS) GN model for Raman amplifier system assessment. GN models have also been developed for systems in the presence of TRx noise [33, 34].

The prediction of the GN model is in terms of SNR, which can also be converted to bit error rate (BER) and utilised for calculating the achievable information rate (AIR). AIR is presented as a measure of the net data rates in coded communication systems after error corrections [36–39]. The AIRs in optical communication systems are limited by nonlinear distortions caused by the Kerr effect in optical fibres, which become more significant for communication systems with wider bandwidths, closer channel spacing, and higher-order modulation formats [40–43]. The effectiveness of multi-channel nonlinearity compensation (MC-NLC) has been investigated from the perspective of AIRs in EDFA-amplified $C-$band optical fibre transmissions [44]. Conducting a

comprehensive analysis of SNR, BER, and AIR in nonlinear optical transmission systems is essential for improving their performance and reliability, particularly when considering practical scenarios. Therefore, advanced modelling techniques should be employed to predict these systems accurately, taking into account real-world factors such as CD, ASE noise, TRx noise, and LPN. However, no research has ever been reported on the GN model accounting for the EEPN. In addition to CD, LPN, and NLI, the signal propagation in the fibre will be further distorted in the presence of EEPN. In such instances, theoretical predictions based on the conventional GN models may greatly overestimate the real system performance.

1.2.3 Signal Processing of Nonlinear Optical Systems

Another important area of research is signal processing in nonlinear coherent optical fibre systems. Signal processing techniques are used to enhance optical fibre system performances by reducing signal distortion, improving signal quality, and increasing the SNR.

For the cases of optical compensations, dispersion compensating fibres (DCF) have been specifically designed to compensate for dispersion. Optical phase conjugation (OPC) has also been developed as a nonlinearity compensation (NLC) method for the nonlinear noise mitigation in coherent optical fibre transmission [14, 42, 43, 45–48]. Advanced digital signal processing (DSP) approaches have been developed for distortion mitigation [11, 49], such as electronic dispersion compensation (EDC) for CD compensation, digital backpropagation (DBP) [43, 50–53] for NLC, Viterbi-Viterbi (VV) estimator [54] and blind phase search (BPS) algorithm [55–60] for LPN compensation. The

ASE noise generated from the amplifiers, the EEPN caused by the interaction between LPN and CD [61–65], signal-EEPN and signal-ASE noise nonlinear interactions cannot be perfectly compensated using DSP [11, 13]. Among these distortions, the EEPN and the ASE noise limit the system performance, while the signal-ASE noise and the signal-EEPN interactions constrain the performance of the NLC [16, 66, 67]. Furthermore, these distortions scale with distance, symbol rate, and modulation format [12, 62, 68–73]. As it has been studied in [61,62,74], EEPN effects may significantly degrade the performance of optical fibre transmission systems.

Except for VV and BPS estimators, over the past few years, the utilization of Kalman filter (KF) estimators in the area of optical communication systems has been extensively investigated [75–80, 80–86] for their capability of phase noise mitigation with low computational complexity. The KF, which was initially reported by R.E. Kalman [87], provides a recursive method for evaluating states of discrete-time controlled processes via minimizing the mean-squared error (MSE). A single-tap KF-based carrier phase estimator (CPE) has been studied in [75] to evaluate and track the LPN and the nonlinear phase noise in 100 Gb/s single-channel QPSK dispersion-managed coherent transmission systems. The polarisation tracking scheme and the frequency offset estimation have also been explored based on the KF in [77, 83–86].

Additionally, apart from the EDFA-lumped amplification scheme for the attenuation compensation, the use of Raman amplifiers in optical communication systems has attracted considerable interest in recent years. However, the presence of nonlinear distortions, such as cross-phase modulation and self-phase modulation, still limits performance of Raman-amplified systems. The study of NLC in $C-$band Raman-amplified WDM systems employing different

modulation formats is important for designing and optimizing optical transmissions with high capacity.

1.3 Thesis Outline

This research investigates the AIRs enhanced by NLCs of DBP and optical phase conjugation. Additionally, a general expression accounting for EEPN based on the GN model will be presented to evaluate the performance of multi-channel optical communication systems using EDC and digital NLC. Furthermore, the performance of KF-based CPE has been studied in dispersion-uncompensated terrestrial and legacy dispersion-managed submarine long-haul optical fibre communication systems, in comparison with VV CPE, BPS CPE, and pilot-aided (PA) CPE.

The research aims to provide important insights and solutions for improving the performance and capacity of optical communication systems, thus meeting the increasing demands for high-capacity data transmission. By addressing the limitations of existing methods, this research has the potential to contribute to the development of more efficient and reliable optical transmission systems.

The structure of the thesis is as follows.

Chapter 2 presents essential theoretical concepts to comprehend engineering challenges related to optical fibre communication. It outlines the optical fibre transmission systems that were utilised in this research, along with the physical characteristics of fibre propagation, associated impairments, and some compensation methods. The chapter also covers the commonly employed analytical models and numerical techniques for optical fibre propagation.

In Chapter 3, the achievable information rates enhanced by NLCs of digital back-propagation (DBP) and optical phase conjugation (OPC) in fully-loaded $C-$band systems amplified by EDFA and distributed Raman amplification with the consideration of the limitation of practical TRx noises are investigated. Research has indicated that the effectiveness of NLC methods in increasing AIRs is significantly influenced by the modulation formats of the signal and the transmission distances.

In Chapter 4, a general expression accounting for EEPN is presented based on the GN model to evaluate the performance of multi-channel optical communication systems using EDC and digital NLC. The nonlinear interaction between the signal and the EEPN is analysed. Numerical simulations are carried out in nonlinear Nyquist-spaced WDM coherent transmission systems. Significant performance degradation due to EEPN in the cases of EDC and NLC is observed, with and without the consideration of TRx noise. The validation of the analytical approach has been done via split-step Fourier simulations. The maximum transmission distance and the laser linewidth tolerance are also estimated to provide important insights into the impact of EEPN. Both lumped EDFA amplification and backwards-pumped distributed Raman amplification are considered. The performance of the $C-$band transmission has been studied based on the model as well. The results reveal that the growth of symbol rates and transmission distances aggravates the distortions in the $C-$band system.

In Chapter 5, the performance of KF-based CPE has been studied in dispersion-uncompensated terrestrial and legacy dispersion-managed submarine long-haul optical fibre communication systems, when significant LPN and amplifier distortions are taken into account. The performance of VV CPE,

BPS CPE, and PA CPE are investigated in the same scenarios for comparison. The impacts of modulation formats, including dual-polarisation quadrature phase shift keying (DP-QPSK) and dual-polarisation 16-*ary* quadrature amplitude modulation (DP-16QAM), the linear dispersion compensation, the NLC, the TRx noise are considered.

Chapter 6 provides an overview of the main findings of the study and emphasizes the areas that require further investigation.

1.4 Key Contributions of the Thesis

The main original contributions in this thesis are outlined as follows:

- In Chapter 3, the impacts of NLCs of DBP and optical phase conjugation on enhancing the achievable information rates in fully-loaded $C-$band systems were investigated. This comprehensive study was published in [15].

- In Chapter 4, the performance of multi-channel optical communication systems using EDC and digital NLC influenced by significant LPN was comprehensively investigated, and the analytical model based on the GN model accounting for EEPN is presented. This study was published in [12].

- In Section 4.8, the performance of the $C-$band transmission influenced by EEPN was studied based on both analytical models and numerical simulations. The impacts of symbol rate and transmission bandwidth have been discussed. The study was included in [88, 89]

- In Chapter 5, the efficiency of KF-based CPE on phase noise mitigation was studied in both dispersion-uncompensated terrestrial and legacy dispersion-managed submarine long-haul optical fibre communication systems with a comparison of VV CPE, BPS CPE and PA CPE. Some of the results were included in [90].

Chapter 2

Theory and Literature Review

This chapter introduces the basic theories and concepts in optical fibre communications, which is necessary to understand the work of this thesis. This chapter systematically introduces the coherent optical communication system, including its structure, propagation process, impairment and its compensation method, numerical simulation method, and analytical model for system performance estimation.

2.1 Coherent Optical Fibre Communication Systems

Optical fibre communication systems generally consist of transmitters, optical fibres as communication channels, optical receivers, and some DSP modules as shown in Fig. 2.1. In fibre optic communications, optical transmitters convert electrical signals into optical signals, which are then transmitted into the fibre. After receiving optical signals from the transmitting end, the optical fibre acts as a communication channel and transmits it to the receiver. The receiver

terminates optical signals from the fibre optic output and converts them into original electrical signals. Some DSP modules are applied for the improvement of system performance.

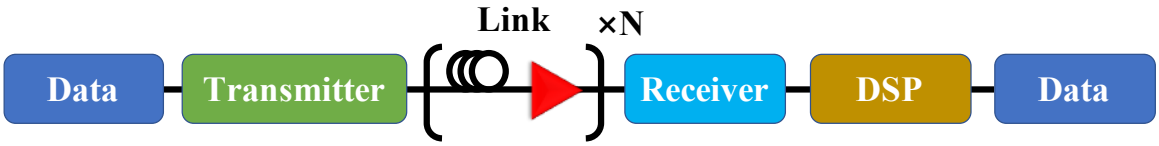

Figure 2.1: Optical fibre system.

2.1.1 Optical Transmitters

An optical transmitter is employed for converting electrical signals into optical signals and sending the optical signals into the fibre. The optical transmitter includes a modulator, an optical source and associated electronic circuits as shown in Fig. 2.2. Semiconductor lasers are usually the preferred optical source for most applications, even though light-emitting diodes (LEDs) may suffice in some less challenging scenarios. The electromagnetic wave generated by the optical source has a constant amplitude. The modulator is used for imposing electrical signals on optical carriers by modifying its phase or amplitude (or both). Once the modulation process is complete, the optical signals are conveyed to the fibre using a coupler.

The amount of launched power is a critical factor to consider during the design process, as augmenting it can extend the amplifier spacing. However, several nonlinear effects restrict the extent to which the input power can be increased. The standard unit of measurement for launched power is usually "dBm", which references 1 milliwatt as the baseline level. The definition is

commonly accepted as:

$$\text{power(dBm)} = 10\lg(\frac{\text{power}}{1\text{mW}}). \tag{2.1}$$

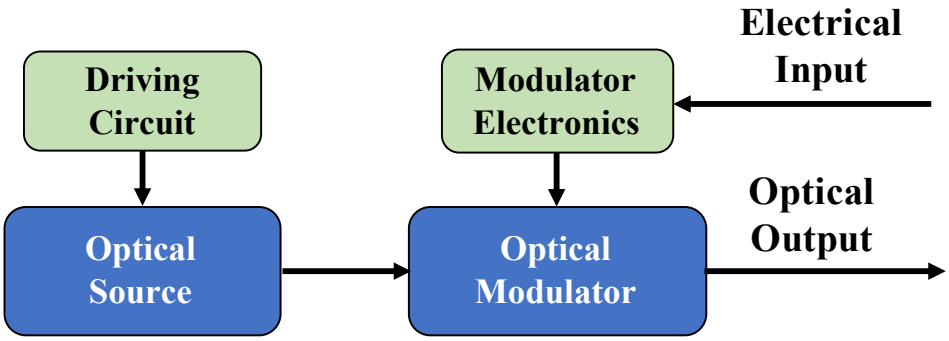

Figure 2.2: Optical transmitter.

Modulator

The phase modulator is a basic type of modulator that operates by passing the optical signal through an electro-optic modulator (EOM), as shown in Fig. 2.3. By applying a voltage to the EOM material, the refractive index is altered, leading to a change in the speed of the light being propagated. This change in speed results in phase modulation of the signal. The input optical signal A_{in} and output phase modulated signal A_{out} can be expressed by

$$A_{\text{out}} = A_{\text{in}}e^{j\varphi} = A_{\text{in}}e^{j\frac{\pi}{V_\pi}V}, \tag{2.2}$$

where the voltage needed to cause a phase shift of π is represented as V_π, and V signifies the applied electrical field. Phase modulators are capable of generating various M-ary phase shift keying (M-PSK) signals.

The Mach-Zehnder modulator (MZM), as shown in Fig. 2.4, is con-

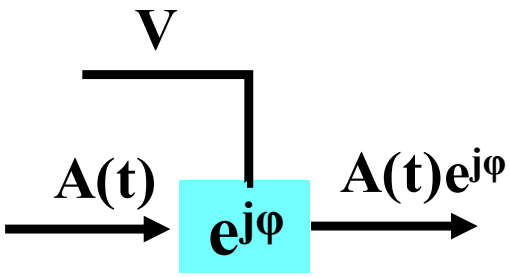

Figure 2.3: Phase modulator.

structed of two arms that introduce a phase shift via EOM. The two optical paths are then recombined with varying phases. After this, a constructive or destructive interference is generated between the two paths, leading to an alteration in amplitude, which enables modulation of the input continuous wave (CW) laser's amplitude.

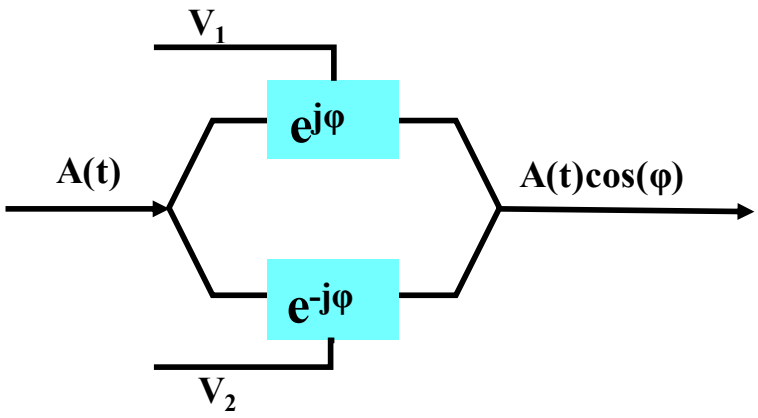

Figure 2.4: Mach-Zehnder modulator.

Optical IQ modulators are utilised to modulate an optical carrier in both I and Q components by two MZMs. Subsequently, the Q channel is phase-shifted by 90 degrees, and the two optical paths are recombined to produce a 2D modulated signal. The configuration of an IQ modulator is shown in

Fig. 2.5.

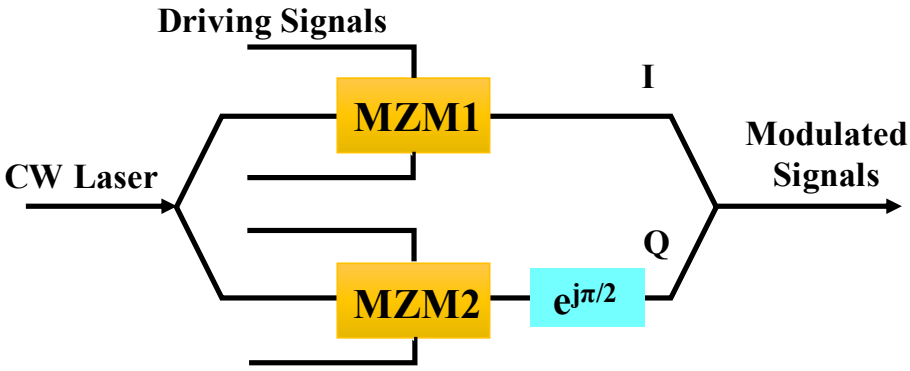

Figure 2.5: Schematic of IQ modulator.

To produce a polarisation-multiplexed (PM) signal, the IQ modulator structure is duplicated over two separate branches where the two orthogonal states of polarisation are modulated, as shown in Fig. 2.6. A polarisation rotator is used to rotate the state of polarisation in one of the two arms for the modulation of dual-polarisation signals.

Additionally, spectral efficiency can be enhanced by adjusting two parameters of the modulator: the constellation cardinality and the ratio R/B with transmitted symbol rate R and bandwidth B. The Nyquist criterion places a maximum restriction on the ratio, which cannot exceed one when there is no intersymbol interference [91]. When the symbol rate R equals the bandwidth B, it is referred to as operating at the Nyquist rate. Nyquist-spaced system has been investigated in this thesis, where the separation between adjacent channels is equal to the symbol rate of the transmitted signal. In Nyquist-spaced WDM systems, multiple optical signals carrying different information are combined and transmitted through the same optical fiber using different wavelengths. Each wavelength channel represents an independent data stream, allowing for a significant increase in overall data capacity and

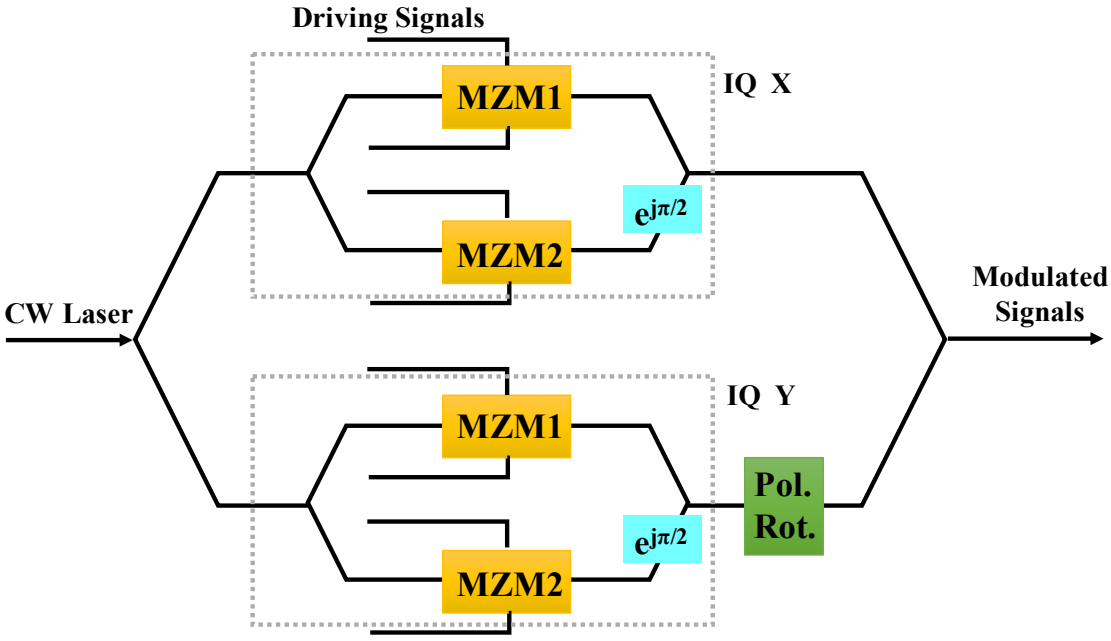

Figure 2.6: Schematic of DP IQ modulator.

enhancing the overall efficiency of the optical communication system.

2.1.2 Coherent Optical Receivers

In the 1980s [92], the initial investigation of coherent detection was prompted by its capacity to enhance receiver sensitivity and extend transmission distances. The development of the EDFA provided practical amplification, which helped overcome the limitations of receiver sensitivity. With the recent advancements in complementary metal-oxide-semiconductor (CMOS) technology, high-speed ADCs/DACs and DSP have become possible, facilitating digital coherent detection.

The detection of the optical field's envelope can be achieved by a single photodiode, where the photocurrent is proportional to the electrical field. However, this type of receiver only captures information about the amplitude.

In the case of coherent detection, a local oscillator (LO) laser is combined with the incoming optical signal to convert the received signal to a baseband frequency, which can then be detected. The second photodiode is used for a 90° phase shift field detection, thereby both amplitude and phase components are captured. Furthermore, polarisation beam splitters (PBSs) can be employed to capture both polarisations of the signal. The current components generated by the coherent polarisation-diverse receiver are proportional to

$$\begin{pmatrix} X_I \\ X_Q \\ Y_I \\ Y_Q \end{pmatrix} \propto \frac{1}{4} \begin{pmatrix} 2\,|A_X|^2 + |\,A_{LO}|^2 \\ 2\,|A_X|^2 + |\,A_{LO}|^2 \\ 2\,|A_Y|^2 + |\,A_{LO}|^2 \\ 2\,|A_Y|^2 + |\,A_{LO}|^2 \end{pmatrix} + \begin{pmatrix} \Re(A_X A_{LO}^*) \\ \Im(A_X A_{LO}^*) \\ \Re(A_Y A_{LO}^*) \\ \Im(A_Y A_{LO}^*) \end{pmatrix}, \tag{2.3}$$

where X and Y denote the two polarisations of the received signals, I and Q represent the in-phase and quadrature components, and A_{LO} denotes the field of the LO. The desired coherently detected terms are represented by the right-side second term, and the first term is the direct detection term.

The use of a direct current (DC) block can eliminate the $|A_{\mathrm{LO}}|^2$ component, but the $|A_{\mathrm{X}}|^2$ term cannot be eliminated. To prevent the influence of this term, the power of the LO laser can be increased, and then the term $|A_{\mathrm{X}}|^2$ will be relatively small. Since the fluctuations of the LO laser can affect the performance as well, an optimal ratio must be determined.

Alternatively, balanced detection can be achieved by doubling the photodiodes and using an optical hybrid to achieve a 90° phase shift. A 180°-phase-shift secondary output can be achieved. The signals at the output of the balanced diodes are shown in Eq. (2.4) and Eq. (2.5). By the detection of

both outputs with a second photodiode and using a transimpedance amplifier (TIA), the term of direct detection can be efficiently suppressed as shown in Eq. (2.6). The schematic of a balanced dual-polarisation coherent receiver is depicted in Fig. (2.7).

$$X_{I+} \propto \frac{1}{4}(2\left|A_X\right|^2+\left|A_{LO}\right|^2) + \Re(A_X A_{LO}^*), \tag{2.4}$$

$$X_{I-} \propto \frac{1}{4}(2\left|A_X\right|^2+\left|A_{LO}\right|^2) - \Re(A_X A_{LO}^*), \tag{2.5}$$

$$X_{I+} - X_{I-} \propto 2\Re(A_X A_{LO}^*). \tag{2.6}$$

Eq. (2.7) is obtained when balanced detection is utilised, and it results in the elimination of non-coherent terms.

$$\begin{pmatrix} X_I \\ X_Q \\ Y_I \\ Y_Q \end{pmatrix} \propto \begin{pmatrix} \Re(A_X A_{LO}^*) \\ \Im(A_X A_{LO}^*) \\ \Re(A_Y A_{LO}^*) \\ \Im(A_Y A_{LO}^*) \end{pmatrix}. \tag{2.7}$$

2.1.3 Fibres and Cables

The structure of optical fibres is shown in Fig. 2.8, and the components are marked. The core made of silica glass provides the path of light propagation, and the larger its size, the greater the amount of light allowed to enter the fibre. The range of the acceptable incident light angle depends on the fibre numerical aperture of the core. The cladding, also made of silica glass, has

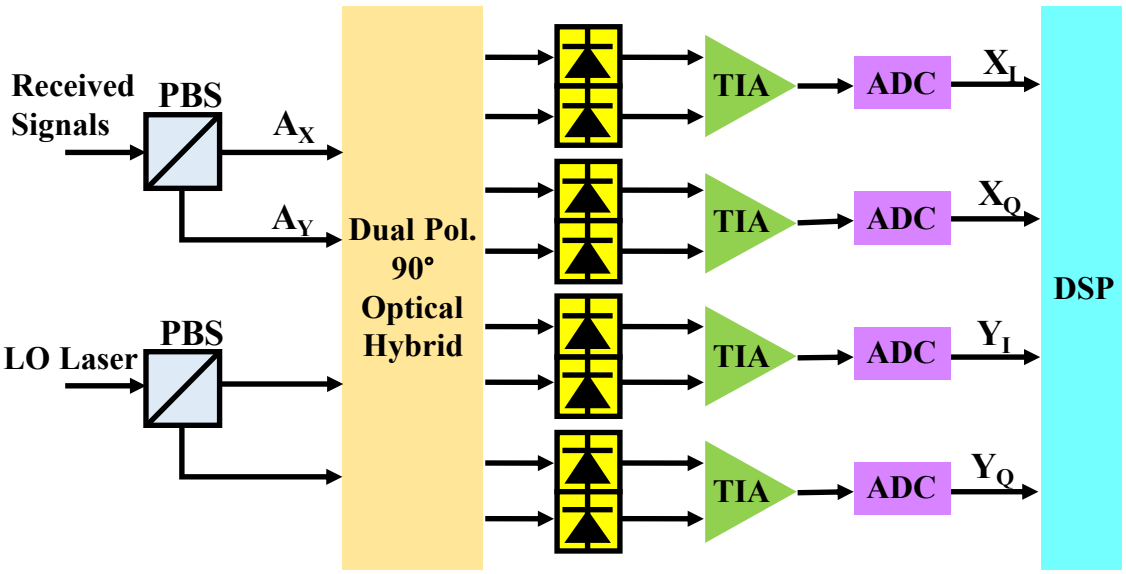

Figure 2.7: Schematic of the balanced dual-polarisation coherent receiver.

a slightly lower refraction index than the core, preventing light from leaving the core. Coatings or buffers protect the core and the cladding and provide strength. When an optical fibre is made into a cable, a material, such as Kevlar, can give the cable strength to prevent stress damage. The outermost jacket provides the final layer of protection and adds strength to cables as well. These jackets usually are coloured for the identification of fibre types.

2.2 Fibre Propagation and Impairments

This section introduces the fibre propagation and impairments including fibre loss, CD, ASE noise, PMD, EEPN, LPN and nonlinear distortions due to the Kerr effect.

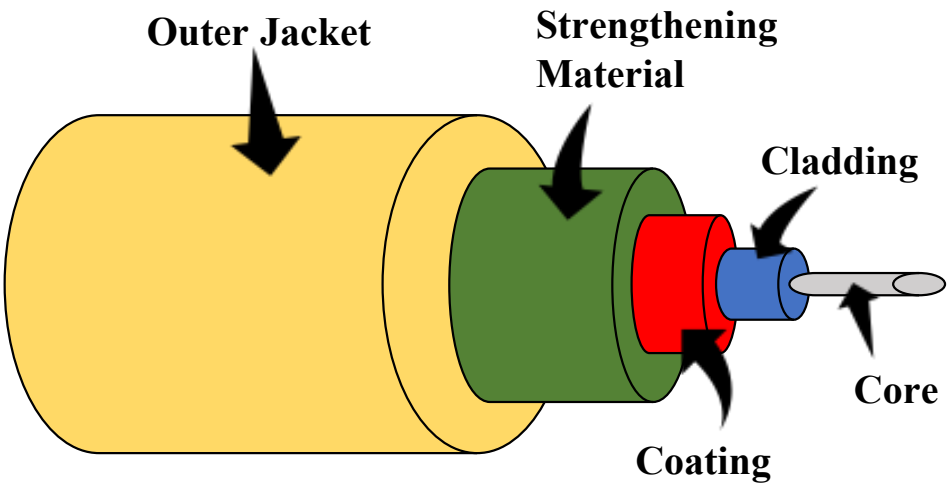

Figure 2.8: Optical fibre structure.

2.2.1 Fibre Loss

As the power of signals is reduced in the fibre link and a minimum amount of received signal power is required for the accuracy of signal detection, the fibre loss limits the reachable maximum transmission distance. The propagation of the optical field amplitude in fibre considering only fibre losses can be expressed by

$$\frac{\partial A}{\partial z} + \frac{\alpha}{2} A = 0, \tag{2.8}$$

where A is the optical field amplitude along the transmission distance z, α is the attenuation coefficient. The signal power reduced by fibre losses is given by

$$P_{\text{out}} = P_{\text{in}} \exp(-\alpha L), \tag{2.9}$$

where P_{out} is the output power at the end of fibres, P_{in} is the input signal power, and L is the fibre length. Customarily, the unit of α is converted to

dB/km by

$$\alpha(\text{dB/km}) = -\frac{10}{L}\log_{10}(\frac{P_{\text{out}}}{P_{\text{in}}}) \approx 4.343\alpha. \tag{2.10}$$

The attenuation parameter depends on wavelength. The loss profile of typical standard single mode fibre (SSMFs) is shown in Fig. 2.9 [93]. The short-wavelength band (S-band) from 1460 to 1530 nm, conventional-wavelength band (C-band) from 1530 to 1565 nm, and long-wavelength band (L-band) from 1565 to 1625 nm are highlighted in the figure. The typical value of α is 0.2 dB/km for SSMFs at the wavelength of ∼1550 nm.

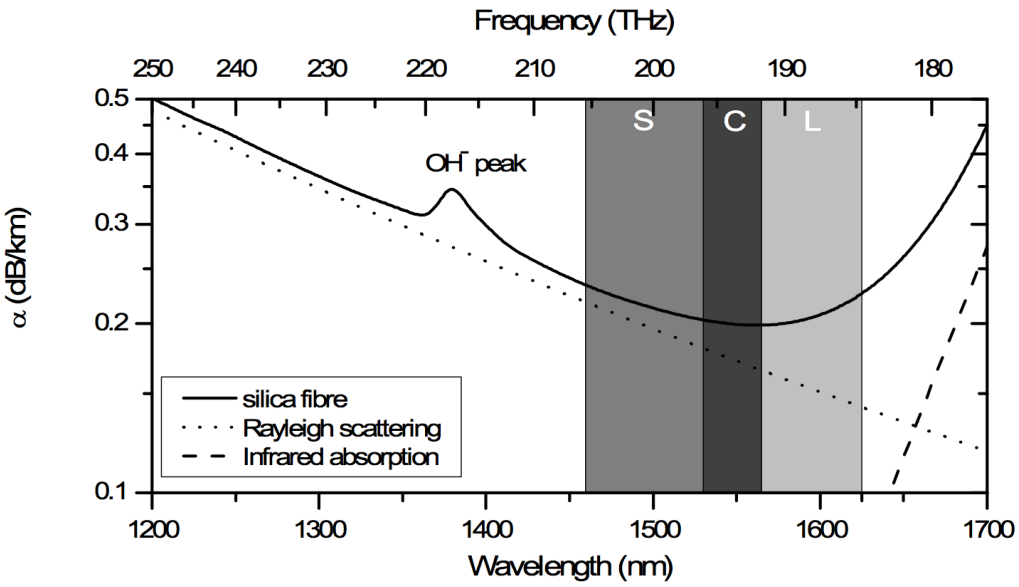

Figure 2.9: Attenuation parameter α of SSMFs as a function of frequency and wavelength. [91]

2.2.2 Chromatic Dispersion

The performance of long-haul optical fibre communication systems is also limited by CD apart from the fibre loss. Signals of different frequency components propagate through the optical fibre with different group velocities, which leads

to signal pulse broadening at the output of the fibre. This phenomenon is called the CD effect, group-velocity dispersion (GVD) or fibre dispersion. The propagation of the amplitude of optical fields along the fibre considering the CD effect and the fibre loss can be simply expressed by

$$\frac{\partial A}{\partial z} + \frac{\alpha}{2}A + \frac{j\beta_2}{2}\frac{\partial^2 A}{\partial t^2} = 0, \tag{2.11}$$

where β_2 is the GVD parameter, and it can be given by

$$\beta_2 = \frac{\partial^2 \beta}{\partial \omega^2}, \tag{2.12}$$

where β is the propagation constant, ω is the angular frequency.

The CD effect of fibre is usually estimated by the dispersion parameter D (the units is ps/nm/km), which can be expressed as

$$D = -\frac{2\pi c \beta_2}{\lambda^2}, \tag{2.13}$$

where c is the light speed in vacuum and λ is the reference wavelength. The value of D for SSMFs is about 17 ps/nm/km at 1550 nm wavelength. CD effects scale with transmission distance and symbol rate, because of the accumulated dispersion and more transmitted frequency components respectively.

It can be found in Eq. (2.13), that the value of D is wavelength dependent. A dispersion slope $S = dD/d\lambda$, which is also called a differential dispersion parameter, is used to assess higher-order dispersive effects. Based on Eq. (2.13), the parameter S can be written as

$$S = (2\pi c/\lambda^2)^2 \beta_3 + (4\pi c/\lambda^3)\beta_2, \tag{2.14}$$

where $\beta_3 = \frac{d\beta_2}{d\omega} \equiv \frac{d^3\beta}{d\omega^3}$ is the third-order dispersion (TOD) parameter.

Since $S > 0$ for most types of fibres, the values of CD effects for different transmission channels are different. Therefore, simultaneous dispersion compensation for all channels is difficult due to higher-order dispersive effects. The value of S for SSMFs is about 0.067 ps/nm^2/km at 1550 nm wavelength. For wideband nonlinear optical transmission systems, the higher-order dispersive effects are significant and need to be considered. The propagation expression of optical field amplitude considering the third-order-dispersion (TOD) is given by

$$\frac{\partial A}{\partial z} + \frac{\alpha}{2}A + \frac{j\beta_2}{2}\frac{\partial^2 A}{\partial t^2} - \frac{\beta_3}{6}\frac{\partial^3 A}{\partial t^3} = 0. \tag{2.15}$$

2.2.3 Amplification Scheme and Amplified Spontaneous Emission Noise

This section concerns fibre loss management and the impact of amplifier noise on the transmitted signal. Common techniques for the periodic use of optical amplifiers along fibre links include two schemes, lumped and distributed amplification schemes. EDFAs are commonly used as lumped amplifiers, while Raman amplifiers can amplify optical signals in a distributed manner. Fig. 2.10 shows the (a) lumped and (b) distributed amplification schemes.

Lumped EDFA Amplification Scheme

The EDFA is widely used in the telecommunications industry, providing a reliable means of amplifying optical signals. EDFAs offer high gain, low noise, and a flat amplification response over a wide bandwidth, making them an ideal choice for long-haul transmission systems. Furthermore, because the ampli-

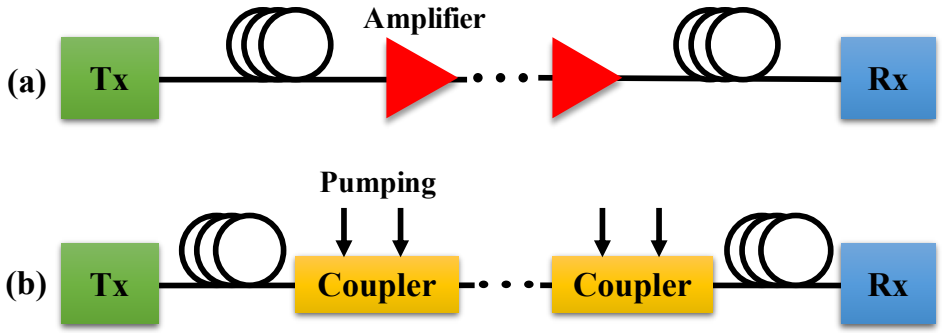

Figure 2.10: Schematic of (a) lumped and (b) distributed amplification. Optical transmitters and receivers are denoted by Tx and Rx, respectively.

fication takes place entirely within the optical domain, there is no need for electrical regeneration of the signals, which can simplify the design of communication systems and reduce costs. An EDFA has become an essential component of modern fibre optic communication systems, providing reliable and efficient amplification of optical signals across a broad range of wavelengths.

The primary factor that restricts the effectiveness of system applications is amplifier noise [94–96]. Amplifiers diminish the SNR of the signal they amplify by introducing noise through spontaneous emission during amplification. This ASE noise results in a decrease in SNR, which is measured by the amplifier noise factor F_n. The amplifier noise factor is given by

$$F_{\mathrm{n}} = \frac{\mathrm{SNR}_{\mathrm{in}}}{\mathrm{SNR}_{\mathrm{out}}}, \tag{2.16}$$

where $\mathrm{SNR}_{\mathrm{in}}$ and $\mathrm{SNR}_{\mathrm{out}}$ are the SNR at the input and the output of the EDFA, respectively. The noise figure NF is defined as the noise factor in units of dB, and is given by

$$\mathrm{NF} = 10 \log_{10} F_n. \tag{2.17}$$

The regularly spaced discrete EDFAs produce linear ASE noise, and this noise remains constant (white noise) within each span of the link. The power spectral density (PSD) of ASE noise is given by [97, 98]

$$S_{\mathrm{ASE}}(f) = N_{\mathrm{pol}} n_{\mathrm{sp}} [G(f) - 1] \cdot h f_0, \tag{2.18}$$

where N_{pol} is the number of polarisation states, n_{sp} is the spontaneous emission factor, h is the Planck constant, f_0 is the laser center frequency, and $G(f)$ is the gain of EDFA, which is defined as the ratio of output power and input power ($G = P_{\mathrm{out}}/P_{\mathrm{in}}$). Commonly it is assumed that the single fibre span loss is compensated by each EDFA, and the EDFA gain can be expressed by

$$G = \exp(\alpha L). \tag{2.19}$$

The overall power of ASE noise can be determined by integrating Eq. 2.18 across the entire optical bandwidth B_{tot} and is expressed by

$$\begin{aligned} P_{\mathrm{ASE}} &= \int_{-B_{\mathrm{tot}}/2}^{B_{\mathrm{tot}}/2} S_{\mathrm{ASE}}(f) H(f) df \\ &= N_{\mathrm{pol}} n_{sp} h f_0 \int_{-B_{\mathrm{tot}}/2}^{B_{\mathrm{tot}}/2} [G(f) - 1] H(f) df, \end{aligned} \tag{2.20}$$

where $H(f)$ refers to the response function of the matched filter applied at the receiver. Since ASE noise is essentially a linear noise, its accumulation occurs linearly with transmission distance.

It is assumed that the optical gain G of each EDFA remains constant within the reference bandwidth B, and the applied 0.1% roll-off RRC filter

makes the channel effectively rectangular. The ASE noise power generated after each fibre span can be calculated as follows:

$$P_{\mathrm{ASE}} = N_{\mathrm{pol}}(G-1)n_{\mathrm{sp}}hf_0 \cdot B. \tag{2.21}$$

The relationship between the factor n_{sp} and the EDFA noise factor F_n can be expressed as [11]

$$F_n = 2n_{\mathrm{sp}}(1-\frac{1}{G}) + \frac{1}{G}. \tag{2.22}$$

Since normally the gain G is significantly higher than 1, the noise factor F_n can be simply approximated as follows:

$$F_n \approx 2n_{\mathrm{sp}}. \tag{2.23}$$

By substituting Eq. (2.23) into Eq. (2.21), the ASE noise power for each span can be calculated by the following expression:

$$P_{\mathrm{ASE}} \approx \frac{1}{2}N_{\mathrm{pol}}\,(G-1)\,F_n\,hf_0 \cdot B\,. \tag{2.24}$$

Distributed Raman Amplification Scheme

Considering a length of fibre that is counter-pumped with pump powers P_p, the signal power profile of distributed Raman amplifiers (DRAs) is defined by the differential equations as follow [99]

$$\frac{dP}{dz} = -\alpha_s P + C_R P_p P, \tag{2.25}$$

$$-\frac{dP_p}{dz} = -\alpha_p P_p - (\frac{\lambda_s}{\lambda_p}) C_R P P_p, \tag{2.26}$$

where P represents optical power from signals, α_s and α_p are attenuation coefficients at the signal and pump wavelength respectively (λ_s and λ_p), C_R is the Raman gain coefficient normalised to the effective area of the fibre ($C_R = g_R/a_p$).

When the signal power is small enough ($P \ll \alpha_p/C_R$), the last term in the differential equation can be ignored. In this case, the signal power at the output of an amplifier of length L is given by

$$P(L) = P(0) \exp(C_R L_{p,\text{eff}} P_p(L) - \alpha_s L), \tag{2.27}$$

where $L_{p,\text{eff}}$ is an effective length, within which signals are amplified by most of the Raman gain, and it is given by $[1 - \exp(-\alpha_p L)]/\alpha_p$. The output signal power in this equation does not include spontaneous Raman scattering generated inside the amplifier. According to Eq. (2.27) and Eq. (2.9), Fig. 2.11 shows the calculated power profile in each span of a backward distributed-Raman-amplified optical fibre transmission with the solid line, and the lumped-amplified case of the EDFA is shown by the dashed line for comparison.

For multi-span dual-polarisation Nyquist-spaced WDM transmission systems, the overall ASE noise exhibits as an additive white Gaussian noise (AWGN) arising either from optical backwards-pumped DRA can be respectively evaluated as follows as

$$P_{\text{ASE}} = 2N \left(\kappa_T + 1\right) \mathcal{N}_{\text{phot}} \cdot h f_0 \cdot R, \tag{2.28}$$

where N is the total number of fibre spans in the link, and R denotes the

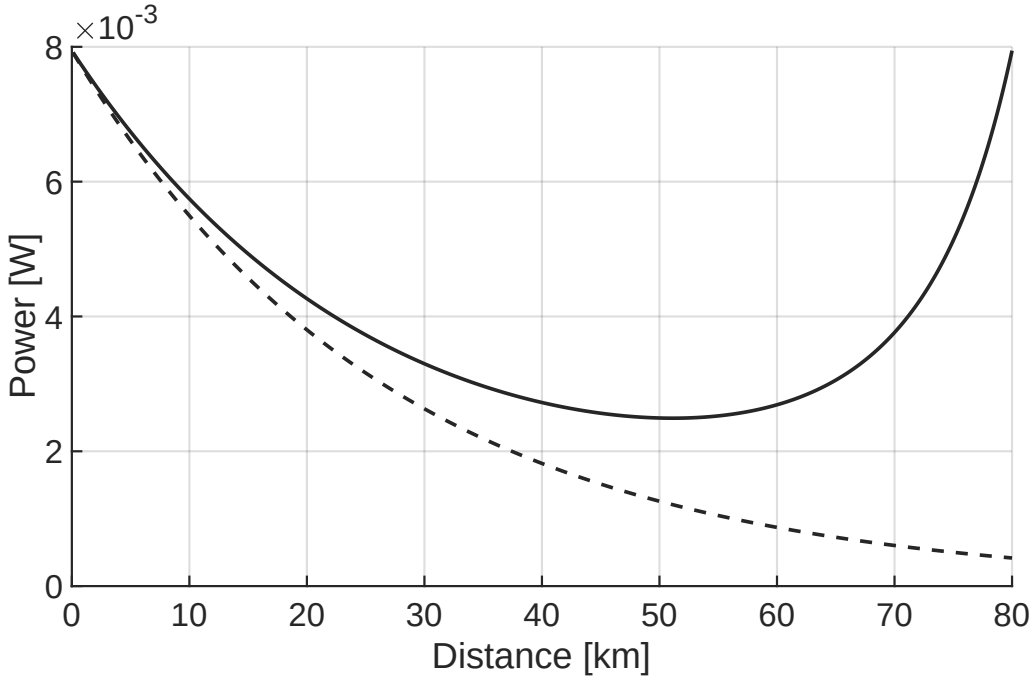

Figure 2.11: Power profile in each span of a backwards distributed-Raman-amplified optical fibre transmission (solid line). The lumped-amplified case of the EDFA is shown by the dashed line.

symbol rate of the transmitted signal, κ_T is the temperature-dependent phonon occupancy factor, and $\mathcal{N}_{\text{phot}}$ denotes the number of spontaneously emitted photons, which has the following closed-form expression

$$\mathcal{N}_{\text{phot}} = \left(\frac{\alpha_{\text{p}}}{C_R P_{\text{p}}}\right)^{\frac{\alpha_{\text{s}}}{\alpha_p}} \left[\Gamma\left(1+\frac{\alpha_{\text{s}}}{\alpha_{\text{p}}}, \frac{C_R P_{\text{p}}}{\alpha_{\text{p}}} e^{-\alpha_{\text{p}} L}\right) - \Gamma\left(1+\frac{\alpha_{\text{s}}}{\alpha_{\text{p}}}, \frac{C_R P_{\text{p}}}{\alpha_{\text{p}}}\right)\right] \exp\left(\frac{C_R P_{\text{p}}}{\alpha_{\text{p}}}\right), \tag{2.29}$$

where $\Gamma(\cdot, x)$ denotes the upper incomplete Gamma function.

2.2.4 Nonlinear Impairments (Kerr Effect)

The refractive index profile of an optical fibre is dependent on the signal optical intensity, which is called the Kerr effect. The nonlinear refractive index is given by

$$n' = n + n_2 \frac{P}{a_{\text{eff}}}, \tag{2.30}$$

where n_2 is the nonlinear-index coefficient, and a_{eff} is the effective mode area. In a strong electromagnetic field, the dielectric produces a nonlinear response to light due to the Kerr effect, which leads to the optical fibre nonlinear effects [21]. The nonlinear effects of optical fibre are enhanced with the increase of transmission power. The major nonlinear effects including self-phase modulation (SPM), cross-phase modulation (XPM), and four-wave mixing (FWM) are considered here [21].

SPM originates from the Kerr effect. The nonlinear phase shift produced by SPM can be described as $\varphi_{\text{NL}} = \gamma P_0(t) L_{\text{eff}}$ where the input power profile $P_0(t)$ depends on the pulse shape, $L_{\text{eff}} = (1 - e^{-\alpha L})/\alpha$ is the effective propagation distance, α and γ are the attenuation and nonlinear coefficients of the fibre. The phase is time-varying, which leads to frequency chirping and spectral broadening through the signal propagation in fibre.

For WDM systems, multiple channels of different wavelengths are transmitted simultaneously in the fibre, which makes the XPM effect significant and causes signal distortion. Considering SPM and XPM, the nonlinear phase shift of the j_{th} channel can be described as $\varphi_{\text{NL}} = \gamma L_{\text{eff}}(P_j(t) + 2\sum_{m \neq j} P_m(t))$. The total phase shift depends on the power of all channels and is affected by the transmission mode of the adjacent channel.

When three channels of frequencies ω_1, ω_2 and ω_3 with optical field

amplitudes of A_1, A_2 and A_3 are simultaneously transmitted, a fourth optical field with the carrier frequency of $\omega_4 = \omega_1 \pm \omega_2 \pm \omega_3$ is generated in the optical fibre. This is the nonlinear phenomenon of FWM. FWM shifts the transmission power between adjacent channels, which leads to channel power loss and crosstalk between channels.

The nonlinear Schrödinger equation (NLSE) considering nonlinear optical impairments including SPM, XPM and FWM can be represented by

$$\frac{\partial A_1}{\partial z} + \frac{\alpha}{2}A_1 + \frac{j}{2}\beta_2\frac{\partial^2 A_1}{\partial t^2} = \underbrace{j\gamma|A_1|^2 A_1}_{\text{SPM}} + \underbrace{2j\gamma(\big|A_2\big|^2 + \big|A_3\big|^2)A_1}_{\text{XPM}} + \underbrace{j\gamma A_2^2 A_3^*}_{\text{FWM}}, \quad (2.31)$$

where γ is the nonlinear coefficient, and is given by

$$\gamma = \frac{2\pi n_2}{a_{\text{eff}}\lambda}. \quad (2.32)$$

To reduce the computational complexity of numerical simulations, Eq. (2.31) can be simplified by combining all optical fields into one optical field, i.e., $A = A_1 + A_2 + A_3$. The simplified optical propagation expression considering the Kerr effect is as follows:

$$\frac{\partial A}{\partial z} + \frac{\alpha}{2}A + \frac{j}{2}\beta_2\frac{\partial^2 A}{\partial t^2} = j\gamma|A|^2 A. \quad (2.33)$$

2.2.5 Polarisation Mode Dispersion

Polarisation division multiplexing (PDM) technology has been widely used in modern optical fibre transmission. Practically, due to manufacturing and stresses experienced by fibre cables, they may exhibit slight asymmetry in their transversal geometry, which can lead to the occurrence of fibre birefringence.

This birefringence can lead to two non-degenerate modes of polarisation corresponding to the two ellipse axes. This can cause the random polarisation evolution of a continuous-wave (CW) optical field. When two different polarisation modes with different effective refractive indices propagate through a fibre with birefringence, they experience different propagation delays. This differential delay results in PMD, which can lead to signal distortion and degradation, and limit the data transmission rate over long-haul fibre-optic communication systems.

Considering the average effect of a fast birefringence, the signal propagation in nonlinear fibre can be described by the Manakov equation [100], which is given by

$$\frac{\partial A}{\partial z} = -\frac{\alpha}{2}A + \frac{j\beta_2}{2}\frac{\partial^2 A}{\partial t^2} + j\frac{8}{9}\gamma|A|^2. \tag{2.34}$$

For a fibre of length L and constant birefringence B_m, PMD can be estimated by [101]

$$\sigma_T^2 = \langle(\Delta T^2)\rangle = 2(\Delta\beta_1 l_c)^2[\exp(-\frac{L}{l_c}) + \frac{L}{l_c} - 1], \tag{2.35}$$

where ΔT is the time delay generated between the two polarised transmission components, $\Delta\beta_1$ is related to group-velocity mismatch [21], l_c is the correlation length of two polarisation components. When $L > 0.1$ km, $l_c \ll L$ can be used to get

$$\sigma_T \approx \Delta\beta_1\sqrt{2Ll_c} \equiv D_p\sqrt{L}, \tag{2.36}$$

where D_p is the PMD parameter, whose value is between 0.1 to 1 ps/$\sqrt{\text{km}}$ for most fibres. Although pulse broadening caused by PMD is relatively small in

comparison to that induced by CD as σ_T is proportional to $\sqrt{L}$.

The Jones matrix [11] $J(\omega)$ for a random rotation by an angle θ and a random phase shift φ can be used to describe the polarisation transformations of signals which propagate in optical fibres, where the relationship between the input optical field and the output optical field in the absence of CD, attenuation and nonlinearity, is given by

$$A_{out}(\omega) = J(\omega)A_{in}(\omega). \tag{2.37}$$

The considered signal propagation process is divided to N_{PMD} sections producing

$$J(\omega) = \prod_{k=1}^{N_{\mathrm{PMD}}} T_k, \tag{2.38}$$

where the k_{th} step of T is given by

$$T_k(\omega) = \begin{pmatrix} e^{-j\frac{\varphi_k}{2}}\cos\theta_k & e^{-j\frac{\varphi_k}{2}}\sin\theta_k \\ e^{j\frac{\varphi_k}{2}}\sin\theta_k & e^{j\frac{\varphi_k}{2}}\cos\theta_k \end{pmatrix} \cdot \begin{pmatrix} e^{-j\frac{\left|\beta_{1k}^x-\beta_{1k}^y\right|}{4}\Delta z\omega} & 0 \\ 0 & e^{j\frac{\left|\beta_{1k}^x-\beta_{1k}^y\right|}{4}\Delta z\omega} \end{pmatrix}. \tag{2.39}$$

Considering the PMD effect, it is necessary to expand the Manakov equation to accommodate the independent evolution of the state of polarisations for the various frequency components of the propagating signal. When the nonlinear PMD is discarded, the Manakov-PMD equation is derived as [100, 102]

$$\frac{\partial A}{\partial z} + \frac{\alpha}{2}A - \frac{j\beta_2}{2}\frac{\partial^2 A}{\partial t^2} - j\frac{8}{9}\gamma|A|^2 = -\frac{|\beta_{1k}^x - \beta_{1k}^y|}{2}T^H \begin{pmatrix} 1 & 0 \\ 0 & -1 \end{pmatrix} T\frac{\partial A}{\partial t}. \tag{2.40}$$

2.2.6 Laser Phase Noise

Coherent systems modulate the amplitude and phase of light to transmit signals, which requires lasers employed in the transmission to generate perfect sinusoidal waves. However, even a single-frequency laser can not generate a perfect sinusoidal oscillation. The phase fluctuation in the optical field generated by lasers causes a non-zero linewidth of the laser output [103]. The signals experience linear phase rotations. Statistical independence of the fluctuations arises from the fact that they originate from the spontaneous emission within the laser. According to the central limit theorem [104], these phase fluctuations are approximately Gaussian distributed. Therefore, LPN can be modelled as the following process

$$\theta_k = \theta_{k-1} + w_k, \tag{2.41}$$

where θ_k is the LPN at the time index of k. The variable w_k follows a Gaussian distribution with the mean of zero and the variance of $2\pi f_{3dB}/R$, and f_{3dB} is the 3-dB laser linewidth [105], where the width of the distribution at a level that corresponds to half of the maximum height of the peak. Laser linewidths vary from a few kHz to MHz [106, 107]. A typical order of the laser linewidth value is around 100 kHz.

2.2.7 Equalisation-Enhanced Phase Noise

The EEPN effect originates from the non-zero net dispersion experienced by the transmitter (Tx) or the LO LPN [62, 108]. Fig. 2.12 illustrates the origin of EEPN in optical fibre communication systems. In a coherent optical transmission system without optical dispersion compensation (ODC), CD compensation and CPE are applied using DSP on the receiver (Rx) side. The matched

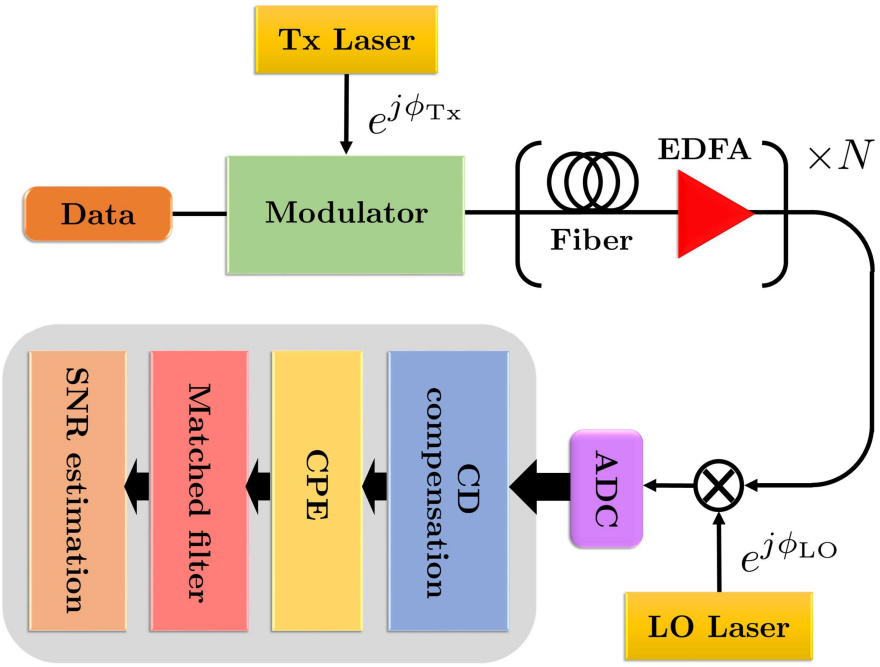

Figure 2.12: Principle of EEPN in an optical fibre communication system.

filter is applied before the SNR estimation for selecting the observed channel. The Tx and the LO lasers provide phase fluctuations of $e^{j\varphi_{\mathrm{Tx}}}$ and $e^{j\varphi_{\mathrm{LO}}}$, respectively. The LPN from the Tx laser is firstly dispersed in the optical fibre and then experiences the CD compensation at the Rx. The net dispersion experienced by the Tx LPN is close to zero. However, the LPN from the LO laser passes through CD compensation only and will be severely dispersed. In this scenario, EEPN is generated due to the interaction between the CD compensation module and the LO LPN [61]. EEPN can also be produced from the interaction between fibre dispersion and the Tx LPN [108, 109]. However, the LO LPN-induced EEPN is more common and all analyses in this paper are performed in this scenario.

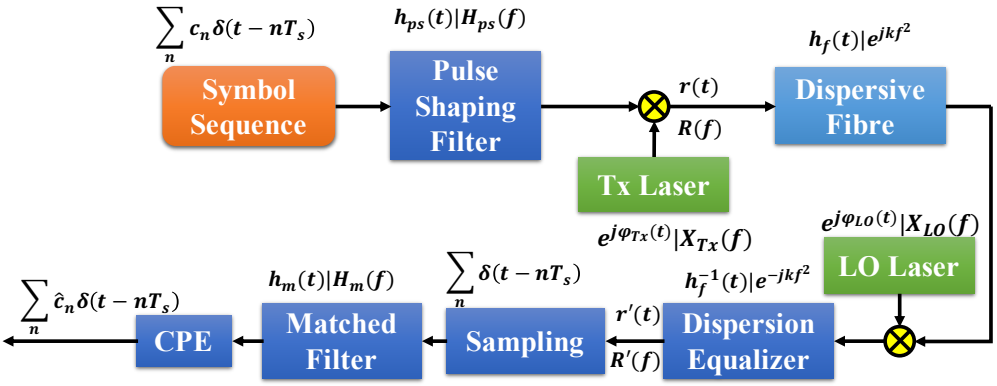

Figure 2.13: System model of a coherent optical system influenced by EEPN effects.

Frequency and Time Domain Response

The influence and principle of EEPN can be analysed by a mathematical model of coherent systems as well. The baseband equivalent representation of a coherent system is utilised for a general analysis. The system model of a coherent optical system influenced by EEPN effects is shown in Fig. 2.13.

In a coherent digital transmission system, signal symbols c_n are shaped for generating band-limited signals by a pulse shaping filter, which is represented by the Fourier transform pair $h_{ps}(t)|H_{ps}(f)$. The Tx laser then is employed for generating the output signal. The Tx LPN is represented by $e^{j\varphi_{\mathrm{Tx}}(t)}|X_{\mathrm{Tx}}(f)$. The output signals at Tx can be represented as $r(t)|R(f)$. Only the impacts of CD $(h_f(t)|e^{jkf^2})$ are considered for the fibre link. The transmitted signals are then detected with an LO with LPN represented as $e^{j\varphi_{\mathrm{LO}}}(t)|X_{\mathrm{LO}}(f)$. The dispersion equalizer is modelled as $h_f^{-1}|e^{-jkf^2}$. The received signal after the dispersion equalizer $r'(t)|R'(f)$ pass through a sampling

module, a matched filter, and a carrier phase recovery (CPR) module. It is hard to mitigate EEPN effects via CPR modules, as EEPN is complex additive noise. Therefore, ideal CPR compensating for only the pure phase noise is considered for a general analysis.

The received signal $R'(f)$ after the dispersion equalizer in Fig. 2.13 can be expressed as

$$R'(f) = [R(f) \cdot e^{jkf^2} \otimes X_{LO}(f)] \cdot e^{-jkf^2}, \tag{2.42}$$

where $k = 2\pi^2\beta_2 l = \pi D l c f_0^{-2}$ calculates accumulate dispersion, l is the fibre length. The Eq. (2.42) can be rewritten as the following expression by reordering the multiplication and convolution operations [61].

$$R'(f) = \int_{-\infty}^{\infty} R(f - f_1) \cdot e^{jk(f_1^2 - 2ff_1)} \cdot X_{LO}(f_1) df_1. \tag{2.43}$$

The above analysis based on the frequency domain indicates that although the linear signal dispersion e^{jkf^2} can be moved by the dispersion equalizer e^{-jkf^2}, the beating term between signals and the LO LPN is not been compensated in the dispersion recovery module, which leads to the enhanced noise.

By taking the inverse Fourier transform of the frequency response shown in Eq. (2.43), the time response of transmitted signals can be derived as

$$\begin{aligned} r'(t) &= IFT\{R'(f)\} \\ &= \int_{-\infty}^{\infty} \left[\int_{-\infty}^{\infty} R(f - f_1) \cdot e^{jk(f_1^2 - 2ff_1)} \cdot X_{LO}(f_1) df_1 \right] \cdot e^{j2\pi ft} df. \end{aligned} \tag{2.44}$$

The time domain response of the received in Eq. (2.44) can be simply rewritten as the following expression [61]

$$r'(t) = \int_{-\infty}^{\infty} X_{LO}(f_1) \cdot e^{-jkf_1^2} \cdot \left[r(t - \frac{kf_1}{\pi}) \cdot e^{j2\pi f_1 t} \right] df_1. \tag{2.45}$$

For cases of digital modulation, the time domain response of received signal $r'(t)$ in Eq. (2.45) can be rewritten as,

$$\begin{aligned} r'(t) = \sum_{n=-\infty}^{\infty} c_n \int_{-\infty}^{\infty} X_{LO}(f_1) \cdot h_{ps}(t - nT_s - \frac{kf_1}{\pi}) \\ \cdot e^{-jkf_1^2} \cdot e^{j\varphi_{\mathrm{Tx}}(t - \frac{kf_1}{\pi})} \cdot e^{j2\pi f_1 t} df_1. \end{aligned} \tag{2.46}$$

For Eq. (2.46), $n = 0$ gives the intra-symbol interference, and $n \neq 0$ gives the inter-symbol interference.

Variance of EEPN

The variance of EEPN is proportional to the accumulated CD, the 3-dB linewidth of the LO (or Tx) laser, and the transmission bandwidth and can be calculated as [62, 63]

$$\sigma^2_{\mathrm{EEPN}} = N \frac{\pi c\, D\, L\, f_{3\mathrm{dB}}}{2 f_0^2} \cdot R\,, \tag{2.47}$$

where N is the number of fibre spans in a link, c is the speed of light in vacuum, D is the CD coefficient, L is the fibre span length, $f_{3\mathrm{dB}}$ is the 3-dB laser linewidth, and f_0 is the laser center frequency, R is the signal symbol rate.

2.3 Numerical Solution for Fibre Propagation: Split-Step Fourier Method

The split-step Fourier method (SSFM) has been widely employed to address the NLSE or Manakov equation [110] and is employed in the numerical simulation in this thesis. The SSFM is based on the idea of breaking up the NLSE or Manakov equation into two parts, one of which is linear and the other nonlinear, and then using the fast Fourier transform (FFT) to switch between the time and frequency domains [111].

According to the SSFM, the exponential operator can be used to express the solution of Eq. (2.34), and the Manakov equation has been re-written as

$$A(t,z) = A(t,0)\exp(\hat{D}z + \hat{N}z), \tag{2.48}$$

where the linear operator $\hat{D}$ and nonlinear operator $\hat{N}$ are

$$\hat{D} = j\frac{\beta_2}{2}\frac{\partial^2}{\partial t^2}, \tag{2.49}$$

$$\hat{N} = j\frac{8}{9}\gamma|A|^2 - \frac{\alpha}{2}. \tag{2.50}$$

The SSFM relies on dividing the integral solution into sufficiently small sections. Therefore, based on Eq. (2.48), the signal propagation in the fibre of each step length Δz is estimated by

$$A(t,z+\Delta z) = \exp[(\hat{D}+\hat{N})\Delta z]A(t,z) \approx \exp(\hat{D}\Delta z)\exp(\hat{N}\Delta z)A(t,z). \tag{2.51}$$

When the step length Δz is close to zero, the solution described in Eq. (2.51)

converges to the accurate solution at left hand side of Eq. (2.51) with dominant error term $\frac{\Delta z^2}{2}(\hat{D}\hat{N} + \hat{N}\hat{D})$ according to the Baker-Campbell-Hausdorff formula [112].

To enhance the precision of Eq. (2.51), the iterative symmetric SSFM can be used by dividing the dispersion operator $\hat{D}$ into two equal parts and applying them before and after the nonlinear operator $\hat{N}$, which is described by [113]

$$\begin{aligned} A(t, z + \Delta z) &= \exp[(\hat{D} + \hat{N})\Delta z]A(t, z) \\ &\approx \exp(\hat{D}\frac{\Delta z}{2}) \exp(\hat{N}\Delta z_{\text{eff}}) \exp(\hat{D}\frac{\Delta z}{2})A(t, z), \end{aligned} \tag{2.52}$$

where

$$\Delta z_{\text{eff}} = \int_{z}^{z+\Delta z} dz' \exp(-\alpha z') = \frac{(1 - \exp(-\alpha\Delta z)) \exp(-\alpha z)}{\alpha}. \tag{2.53}$$

Fig 2.14 provides a summary of the numerical implementation of the symmetric SSFM. The SSFM for a one-step size of Δz consists of the following steps: 1) transform the time-domain signal sequence at a distance of z into the frequency domain with the FFT; 2) multiply the transformed signal by $\exp(\hat{D}\frac{\Delta z}{2})$ to account for the effects of dispersion; 3) transform the result back into the time domain with the inverse FFT (IFFT); 4) multiply the signal by $\exp(\hat{N}\Delta z_{\text{eff}})$ to account for the nonlinear effects of the fibre; 5) transform the signal back into the frequency domain with the FFT; 6) propagate the linear part of the SSFM for the remaining $\frac{\Delta z}{2}$ step size, taking into account the effects of dispersion; 7) transform the signal back into the time domain with the IFFT to obtain the time-domain signal sequence at a distance of $z + \Delta z$.

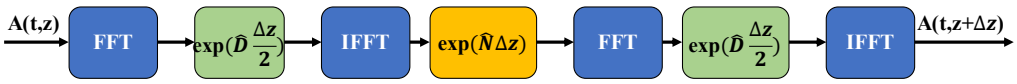

Figure 2.14: Structure of an SSFM segment of a step length Δz

2.4 Digital Signal Processing

After the signal detection and digitisation through the coherent receiver and the analogue-digital converter (ADC), the transmitted signals can be further processed by advanced DSP. The principle of EDC, DBP and CPE is introduced in this section.

Electronic Dispersion Compensation

The impairments of CD introduced in Section 2.2.2 is time independent and can be compensated in the frequency domain via a linear non-adaptive filter, whose response is as follows:

$$H(f) = \exp(-jf^2 d_a/2), \tag{2.54}$$

$$d_a = \int_0^L \beta_2(z)dz. \tag{2.55}$$

The CD could also be compensated in the time domain by the inverse Fourier transform of Eq. (2.54):

$$h(t) = \sqrt{\frac{2\pi}{jd_a}} \exp(-\frac{jt^2}{2d_a}). \tag{2.56}$$

Operating the impulse response digitally is complicated due to the infinite duration. A finite-impulse-response filter (FIR) could be employed for

implementing the impulse response when it is truncated appropriately, and the taps depend on d_a and the symbol rate. The EDC was implemented in the frequency domain in this thesis.

Digital Back-Propagation

DBP is a technique used to compensate for linear and nonlinear signal transmission impairments in optical communication systems [114, 115]. The principle of DBP is to estimate the transmitted signal by a DBP algorithm based on the received signal. The computational complexity of DBP can be reduced by using the SSFM [11, 114] to solve the inverse Manakov equation or NLSE of the optical fibre link. This is equivalent to passing the received signal again through the fibre with the opposite sign parameter. The principle of DBP was briefly illustrated in Fig. 2.15.

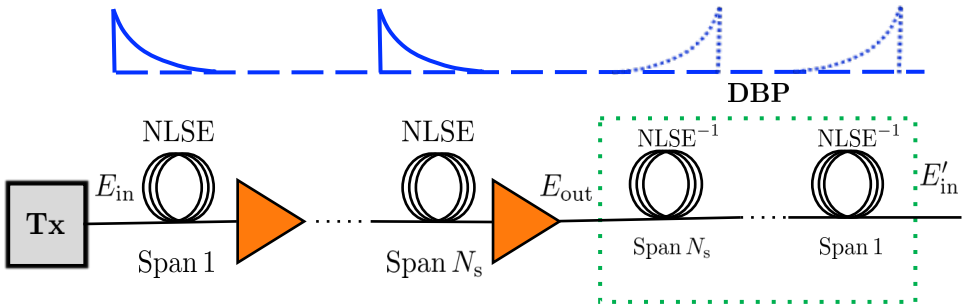

Figure 2.15: The principle of digital back-propagation

The main disadvantage of DBP is that its higher computational requirement leads to the difficulty of real-time implementation in a practical optical nonlinear communication system. Moreover, theoretically, DBP can completely reverse the effects of optical fibre nonlinear propagation, but in practice, it can be significantly affected by some stochastic impairments, such as ASE noise, LPN, PMD, etc.

Kalman Filter

A KF is a single-tap filter which can estimate using only one previous value of the observed data without the requirement of storing the past symbols. It was first developed by R. E. Kalman in 1960 [87] and has been considered for application in the field of optical communication systems in recent years, due to its potential ability to compensate and track some optical transmission distortions, especially the phase noise, simultaneously. KF can improve coherent optical communication system performance significantly with low computational complexity, and few required parameters of transmission channels. Therefore, a KF has great advantages and practical application prospects in the field of the optical nonlinear communication system.

The KF uses feedback control to estimate the process. To be specific, the filter estimates the process state first and then uses noise-included measurements as feedback. Thus, the calculation procedure of the KF can be divided into two parts: the time update process and the measurement update process. The time update equations are used to project forward the state and error covariance. The measurement update equations are used to obtain feedback and improve the former state and error covariance estimate. The result of the time update process is a priori estimate, and the result of the measurement update process is a posteriori estimate. The operation of the discrete KF can be illustrated briefly by Fig. 2.16. Where x is the state of a discrete-time controlled process, $\widetilde{z}$ is the measurement value. $\hat{x}_k^-$ is the priori state estimate at step k, and $\hat{x}_k$ is the posteriori state estimate at step k with a given measurement $\widetilde{z}_k$. $\widetilde{P}_k^-$ is a priori estimate error covariance, and $\widetilde{P}_k$ is a posteriori estimate error covariance. $\widetilde{Q}$ is the process noise covariance and $\widetilde{R}$

is the measurement noise covariance. $\widetilde{H}$ relates the state to the measurement $\widetilde{z}_k$. K_k is the Kalman gain.

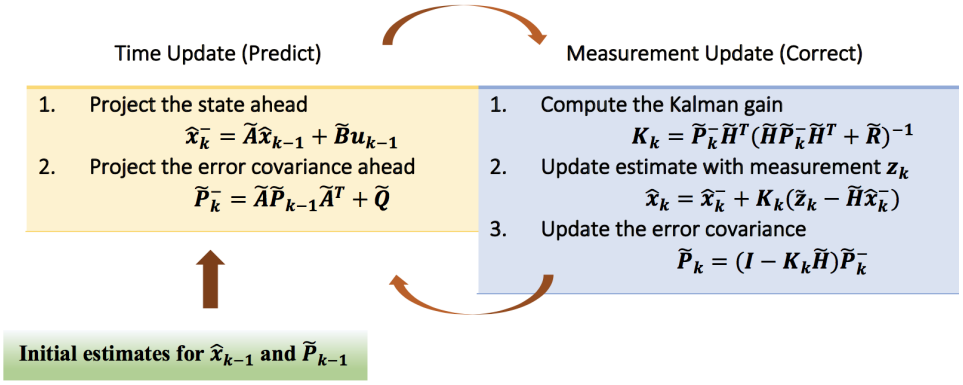

Figure 2.16: The operation of the discrete KF

In recent years, the KF is under wide investigation in the field of optical nonlinear communication systems for its capability of reducing frequency offsets [116, 117] and phase noise [75, 83, 118–120], as well as polarisation demultiplexing [84–86, 121].

2.5 Analytical Modelling

Because of the high computational complexity of the Manakov solution of NLSE, modelling of nonlinear optical fibre transmission for a quick and simple performance estimation attracts great research interest. Analytical models and the closed-form approximation of predicting equations are explored and derived, especially considering the impact of fibre nonlinearities. Among them, the family of Gaussian noise (GN) models (see, e.g., [22–24]) has become widely popular owing to its sufficiently accurate predictions and relatively low complexity. The latest GN models have also been developed for systems in the presence of TRx noise [33, 34]. In the following, the GN model and its recent

developments are introduced and discussed.

2.5.1 Gaussian Noise Model

The GN-model was first reported by Carena *et al.* in [69], and further developed in [22, 28, 122]. The GN-model is mainly based on two hypotheses: perturbative hypothesis (impacts of fibre nonlinearities is low); and transmitted signals are modelled as Gaussian process (the Gaussianity of optical signals is assumed due to the large accumulated CD and the dense modulation format [70]).

To predict the performance of a coherent nonlinear optical fibre transmission system, basically considering the distortion caused by the fibre nonlinearity and the ASE noise, and assuming that they are statistically independent AWGM noises, the SNR of the received signals after coherent detection and EDC can be given by [25, 28]

$$\mathrm{SNR} = \frac{P}{P_{\mathrm{ASE}} + P_{\text{s-s}}}\,, \tag{2.57}$$

where P is the optical launch power per channel, P_{ASE} is the ASE noise power arising from the optical amplifier, $P_{\mathrm{s-s}}$ is the signal-signal interaction caused by the optical Kerr effect. As Eq. (2.57) assumes that the noise sources are AWGN, the total power of the noise can be calculated by the sum of the contributions from the individual noise sources. The contribution of the signal-signal nonlinear interaction is given by

$$P_{\text{s-s}} = \eta\,(N, B) \cdot P^3\,, \tag{2.58}$$

where $\eta\left(N,B\right)$ is the NLI distortion coefficient with the number of fibre spans N and the transmitted bandwidth B, and is given by the following double integral [22, 28, 70, 71]

$$\begin{aligned}\eta\left(N,B\right) =& \frac{16\gamma^2}{27\,R^2}\int_{-B/2}^{B/2}\int_{-B/2}^{B/2} df_1 df_2 \mid \varphi\left(f,f_1,f_2 \mid L,N\right) \\ & \cdot\rho\left(f,f_1,f_2 \mid L\right)\mid^2 \mathrm{rect}\left(\frac{f_1+f_2}{B}\right),\end{aligned} \tag{2.59}$$

where γ is the fibre nonlinear coefficient, $\mathrm{rect}\left(x\right)$ stands for the rectangular function, the factor $\varphi\left(f,f_1,f_2 \mid L,N\right)$ accounts for the NLI distance evolution over multi-span fibre transmission, and $\rho\left(f,f_1,f_2 \mid L\right)$ is the FWM efficiency factor. These factors have the following expressions:

$$\varphi\left(f,f_1,f_2 \mid L,N\right) = \frac{1-\exp\left(j\,\Delta\beta\left(f,f_1,f_2\right)\cdot NL\right)}{1-\exp\left(j\,\Delta\beta\left(f,f_1,f_2\right)\cdot L\right)}, \tag{2.60}$$

$$\rho\left(f,f_1,f_2 \mid L\right) = \int_0^L dz P(z)\exp(j\Delta\beta(f,f_1,f_2)z), \tag{2.61}$$

where $j \triangleq \sqrt{-1}$ denotes the imaginary unit, $P(z)$ is the signal power profile along the fibre, and the FWM phase-mismatch $\Delta\beta\left(f,f_1,f_2\right)$ can be approximated as (see, e.g., [123])

$$\Delta\beta\left(f,f_1,f_2\right) \approx 4\pi^2\left[\,\beta_2+\pi\left(f_1+f_2\right)\beta_3\,\right]\cdot\left(f_1-f\right)\left(f_2-f\right), \tag{2.62}$$

where β_2 and β_3 are the $2^{\mathrm{nd}}-$ and $3^{\mathrm{rd}}-$ dispersion coefficients, respectively [21, 22].

The FWM efficiency factor $\rho\left(f,f_1,f_2 \mid L\right)$ in Eq. (2.59) has a different expression depending on the optical amplification scheme used.

Lumped EDFA Scheme

When lumped EDFAs are applied in the system, the signal power profile is $P(z) = e^{-\alpha z}$. The closed-form expression of the FWM efficiency factor is given by

$$\rho\left(f, f_1, f_2 \,|\, L\right)_{EDFA} = \frac{1 - \exp\left[-\left(\alpha + j\,\Delta\beta\left(f, f_1, f_2\right)\right) \cdot L\right]}{\alpha - j\,\Delta\beta\left(f, f_1, f_2\right)}. \tag{2.63}$$

Distributed Raman Amplifier Scheme

For backwards-pumped DRA, it can be respectively given by

$$\begin{aligned}\rho\left(f, f_1, f_2 \,|\, L\right)_{DRA} =& \frac{\Xi\left(f, f_1, f_2\right)}{\alpha_{\mathrm{p}}} \left(-\frac{C_R P_{\mathrm{p}}}{\alpha_{\mathrm{p}}}\right)^{\frac{\alpha - j\,\Delta\beta(f, f_1, f_2)}{\alpha_{\mathrm{p}}}} \\ & \cdot \exp\left(-\frac{C_R P_{\mathrm{p}}}{\alpha_{\mathrm{p}}}\right),\end{aligned} \tag{2.64}$$

$$\begin{aligned}\Xi\left(f, f_1, f_2\right) \triangleq& \Gamma\left(-\frac{\alpha - j\,\Delta\beta\left(f, f_1, f_2\right)}{\alpha_{\mathrm{p}}}, -\frac{C_R P_{\mathrm{p}}}{\alpha_{\mathrm{p}}}\, e^{\alpha_{\mathrm{p}} L}\right) \\ & - \Gamma\left(-\frac{\alpha - j\,\Delta\beta\left(f, f_1, f_2\right)}{\alpha_{\mathrm{p}}}, -\frac{C_R P_{\mathrm{p}}}{\alpha_{\mathrm{p}}}\right).\end{aligned} \tag{2.65}$$

where $\Gamma(a, \cdot)$ is a upper incomplete Gamma function with the complex parameter a. The Raman gain C_R is assumed to be polarisation independent. The integral in Eq. (2.59) was evaluated numerically by means of the multivariable quasi-Monte-Carlo integration [124].

2.5.2 Closed-Form Approximations of the GN Model

The calculation of the integral of Eq. (2.59) takes a large amount of time, which poses a limitation on the real-time application of the GN model. The closed-form approximation of the GN model has been proposed for low computation complexity [27].

Considering the accumulation of NLI over multiple identical fibre spans, Eq. (2.58) can be simply rewritten as

$$P_{\text{s-s}} = N^{1+\varepsilon}\eta\left(1,B\right)\cdot P^{3}\,, \tag{2.66}$$

where $\eta\left(1,B\right)$ is the NLI distortion coefficient of single span, ε is the coherence factor [28], and can be evaluated by

$$\varepsilon = \frac{1}{\ln 100}\ln(\frac{\eta(100,B)}{\eta(1,B)}) - 1. \tag{2.67}$$

For EDFA-employed Nyquist-spaced WDM systems, the closed-form approximation of the coherence factor ε is [22]

$$\varepsilon \approx \frac{3}{10}\log[1+\frac{6}{\alpha L\,\text{asinh}(\frac{\pi^2|\beta_2|}{2\alpha}B^2)}], \tag{2.68}$$

where $\text{asinh}\left(\cdot\right)$ denotes the inverse hyperbolic sine.

For dual-polarisation lumped-EDFA applied Nyquist-spaced WDM transmission systems, the NLI distortion coefficient over single fibre span $\eta\left(1,B\right)$ in Eq. (2.66) has the following closed-form approximation [27]

$$\eta\left(1,B\right) \approx \frac{8}{27}\frac{\gamma^2 L_{\text{eff}}}{\pi\left|\beta_2\right|R^2}\,\text{asinh}\left(\frac{\pi^2}{2}\left|\beta_2\right|L_{\text{eff}}\cdot \text{B}^2\right). \tag{2.69}$$

2.5.3 Enhanced GN Model for Modulation-Format Dependence Correction

GN model is based on the assumption that the transmitted signals are Gaussian. This assumption leads to an overestimation of NLI power for quadrature amplitude modulation (QAM) signals. An enhanced GN model has been developed for the accurate estimate of system performance with consideration of the modulation format [26, 70, 71]. If it is assumed that all WDM channels have the same dual-polarization multiplexed modulation format, the nonlinear interference coefficient $\eta\left(N,B\right)$ assessed at the center channel can be decomposed as

$$\eta\left(N,B\right)=\eta^{(0)}\left(N,B\right)+\eta^{(\mathrm{QAM})}\left(N,B\right). \tag{2.70}$$

The first term $\eta^{(0)}\left(N,B\right)$ in Eq. (2.70) is the signal modulation format independent term, which evaluates the NLI noise contribution assuming a Gaussian input. The second term $\eta^{(\mathrm{QAM})}\left(N,B\right)$ accounts for the corrections required for QAM formats. The conventional closed-form approximation is given by [26]

$$\eta^{(\mathrm{QAM})}\left(N,B\right)\approx-\frac{80}{81}\,\chi\,\frac{N\gamma^{2}L_{\mathrm{eff}}^{2}}{\pi\left|\beta_{2}\right|L\,R^{2}}\left[\mathrm{HN}\left(\frac{B/R-1}{2}\right)+1\right], \tag{2.71}$$

where L_{eff} is the effective length of fibre span, χ stands for the constant prefactor. The values of χ for the quadrature phase shift keying (QPSK), 16QAM, 32QAM, 64QAM, and Gaussian input are equal to $\{1, 17/25, 69/100, 13/21, 0\}$, respectively. The function $\mathrm{HN}\left(x\right)$ denotes harmonic numbers, and can be expressed by $\sum_{n=1}^{x}1/n$.

2.5.4 Nonlinear Signal-ASE Interactions

When the NLI has been greatly mitigated by digital NLC (such as DBP), nonlinear interactions between signal and ASE noises limit the system performance and must be taken into consideration [125]. Therefore, the SNR of systems applied with NLC is given by

$$\mathrm{SNR}_{\mathrm{NLC}} = \frac{P}{P_{\mathrm{ASE}} + P_{\text{s-s}}^{\mathrm{NLC}} + P_{\text{s-ASE}}}\,, \tag{2.72}$$

where the $P_{\text{s-s}}^{\mathrm{NLC}}$ is the residual signal-signal interaction after an NLC and is given by

$$P_{s-s}^{\mathrm{NLC}} \approx N^{\varepsilon+1}[\eta(1,B) - \eta(1,B_{\mathrm{NLC}})]P^3, \tag{2.73}$$

where B_{NLC} is the NLC bandwidth. When full-field (FF) NLC (where $B_{\mathrm{NLC}} = B$) is applied, the signal-signal nonlinear interaction P_{s-s}^{NLC} can be negligible.

The $P_{\text{s-ASE}}$ is the signal-ASE interaction due to the FWM process. The $P_{\text{s-ASE}}$ considering $1^{st}-$ and $2^{nd}-$ order impacts of nonlinear interference between ASE noise and signals is given by

$$P_{\text{s-ASE}} \approx 3\,\xi_1\,\eta\,(1,B)\,\frac{P_{\mathrm{ASE}}}{N}\cdot P^2 + 9\,\xi_2\,\eta\,(1,B)^2\,\frac{P_{\mathrm{ASE}}}{N}\cdot P^4\,, \tag{2.74}$$

where ξ_1 and ξ_2 are the $1^{st}-$ and $2^{nd}-$ order distance-dependent coefficients accounting for the accumulation of nonlinear signal-ASE interactions along the multi-fibre-span link, and they are given by the following expressions respectively [22, 23, 42, 67].

$$\xi_1 \triangleq \sum_{n=1}^{N} n^{\varepsilon+1}, \tag{2.75}$$

$$\xi_2 \triangleq \sum_{n=2}^{N} \sum_{m=1}^{n-1} m^{\varepsilon+1}. \tag{2.76}$$

The closed-form approximations for $1^{st}-$ and $2^{nd}-$ are expressed by [67, 126, 127]

$$\xi_1 \approx \frac{N^{\varepsilon+2}}{\varepsilon+2} + \frac{N^{\varepsilon+1}}{2}, \tag{2.77}$$

$$\xi_2 \approx \frac{\zeta(-\varepsilon-1) - \zeta(-\varepsilon-1, N)}{2} + \frac{\zeta(-\varepsilon-2) - \zeta(-\varepsilon-2, N)}{\varepsilon+2}, \tag{2.78}$$

where $\zeta(z)$ and $\zeta(z, r)$ are the Euler-Riemann zeta function and Hurwitz's generalised zeta function [128].

2.5.5 Transceiver Noise Modelling

The aforementioned analyses did not account for the impact of TRx noise. The transceiver noise includes all noise contributions from both the Tx and Rx, such as the finite resolution of digital-to-analogue converters (DACs) and ADCs, the noise from the linear electrical amplifiers, and the noise from some optical components [34]. It is related to the back-to-back (BTB) systems and defines the maximum achievable SNR in a transmission system. Based on Eq. (2.57) and Eq. (2.72), the analytical model considering the TRx noise can be expressed as

$$\mathrm{SNR} = \frac{P}{P_{\mathrm{ASE}} + P_{\text{s-s}} + P_{\text{s-ASE}} + P_{\mathrm{TRx}} + P_{\text{s-TRx}}}, \tag{2.79}$$

where P_{TRx} represents the noise power owing to the TRx noise, $P_{\text{s-TRx}}$ is the nonlinear interaction between the TRx noise and the signal. The TRx noise power P_{TRx} is given by

$$P_{\mathrm{TRx}} = \kappa P, \tag{2.80}$$

$$\kappa \triangleq \mathrm{SNR}_{\mathrm{TRx}}^{-1}, \tag{2.81}$$

where $\mathrm{SNR}_{\mathrm{TRx}}$ is the TRx SNR limit (the maximum achievable SNR in BTB systems).

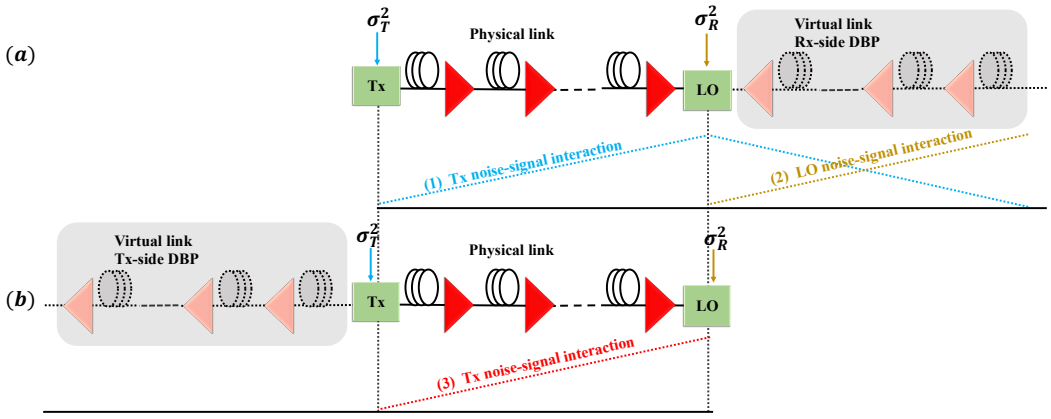

Figure 2.17: Nonlinear signal-TRx noise interference accumulation along fibre spans applied with (a) Rx-side NLC and (b) Tx-side NLC. Line (1) shows the nonlinear interaction between Tx noises and signals, which is removed after the virtual link of DBP, line (2) shows nonlinear signal-Rx noise interactions, produced after DBP, and line (3) shows nonlinear transmitter noise-signal beating, generated in transmission.

The signal-TRx noise nonlinear interference $P_{\text{s-TRx}}$ can be calculated as [33, 129]

$$P_{\text{s-TRx}} \approx 3\,\eta\,(1, B)\,\kappa\xi_{\mathrm{TRx}}P^3, \tag{2.82}$$

where ξ_{TRx} is the accumulation factor of signal-TRx noise nonlinear interference, and it depends on the virtual link placement of NLC schemes and where the TRx noise is introduced. Fig. 2.17 shows the nonlinear signal-TRx noise interference accumulation along fibre spans applied with Rx-side DBP (a) and Tx-side DBP (b). Line (1) shows the nonlinear interaction between Tx noises and signals, which were removed after the virtual link of DBP. Line (2) shows

nonlinear signal-Rx noise interactions produced after DBP, where the number of Tx-side virtual spans $X = 0$. Line (3) shows nonlinear transmitter noise-signal beating, generated in transmission, where the number of Tx-side virtual spans X is equal to the number of the physical fibre spans N. The expression of factor ξ_{TRx} is given by

$$\xi_{\mathrm{TRx}} = (1 - \kappa_{\mathrm{R}})X^{1+\varepsilon} + \kappa_{\mathrm{R}}(N - X)^{1+\varepsilon}, \tag{2.83}$$

where $\kappa_R \in [0, 1]$ is the relative quantity of Rx noise to the total TRx noise. The TRx noise can be split into two contributions-the Tx noise σ^2_{T} and the Rx noise σ^2_{T}. They are given by

$$\sigma^2_{\mathrm{T}} = (1 - \kappa_{\mathrm{R}})\kappa P, \tag{2.84}$$

$$\sigma^2_{\mathrm{R}} = \kappa_{\mathrm{R}}\kappa P. \tag{2.85}$$

The SNR of systems considering only the Tx noise or the Rx noise is expressed by

$$\mathrm{SNR}_{\mathrm{Tx}} = \frac{\mathrm{SNR}_{\mathrm{TRx}}}{1 - \kappa_{\mathrm{R}}}, \tag{2.86}$$

$$\mathrm{SNR}_{\mathrm{Rx}} = \frac{\mathrm{SNR}_{\mathrm{TRx}}}{\kappa_{\mathrm{R}}}. \tag{2.87}$$

2.6 Summary

To fully understand the complexity and intricate issues of coherent fibre optic communication systems, it is necessary to have a comprehensive understanding

of their fundamental theoretical principles. This chapter serves as an introduction to the theoretical background of coherent optical communication systems, providing detailed explanations of the various components that make up these systems.

The chapter discusses coherent optical communication structures, which are an important element of modern fibre optic communication systems. Coherent structures achieve long-distance transmission of high-speed data through advanced modulation techniques and coherent detection schemes. By understanding the principles behind these structures, readers will gain a better understanding of the internal workings of these communication systems.

The chapter also introduces the noises that affect fibre transmission, including linear and nonlinear noises. It elaborates on the sources of these noises and various methods used to mitigate their impact on signal transmission. The amplification schemes of lumped-amplified EDFAs and distributed Raman amplifiers are introduced. By utilizing DSP techniques, such as EDC for dispersion removal and DBP for nonlinear compensation, signal distortions caused by these noises can be compensated for, thereby improving system performance.

In addition, the chapter extensively discusses the family of GN models used to predict transmission system performance. These models help researchers and engineers simulate the behaviour of coherent fibre optic communication systems, enabling them to optimize system designs and identify potential issues before they occur.

Overall, this chapter provides a solid foundation for readers to understand the theoretical background of coherent fibre optic communication systems. By mastering these concepts, readers will gain a better understanding of

the subsequent chapters in this thesis, which delve deeper into specific aspects of these communication systems.

Chapter 3

Modelling and Information Rates in Nonlinear Coherent Optical Systems

To study the performance of NLC in Raman- and EDFA-amplified systems, a theoretical model is developed to take into account the modulation format-dependent distortions and transceiver noise limitations. This enables a realistic evaluation of the efficacy of NLC to enhance AIRs for different modulation formats. The results can provide important insight into the transmission regimes where NLC can have a significant impact on AIRs in Raman-amplified $C-$band systems, as well as highlighting the required compensation bandwidth for these systems. The results in this Chapter was from [15] by T. Xu *et al.*

This chapter is structured as follows: in Section 3.1, the analytical models for estimating the performance of Raman- and EDFA-amplified systems are presented along with the AIR calculation method; in Section 3.2, the performance of digital NLC in Raman- and EDFA-amplified systems with

and without the distortion from transceiver noises is investigated; in Section 3.3, the performance of OPC-employed Raman-amplified systems with and without the impact of transceiver noises is examined.

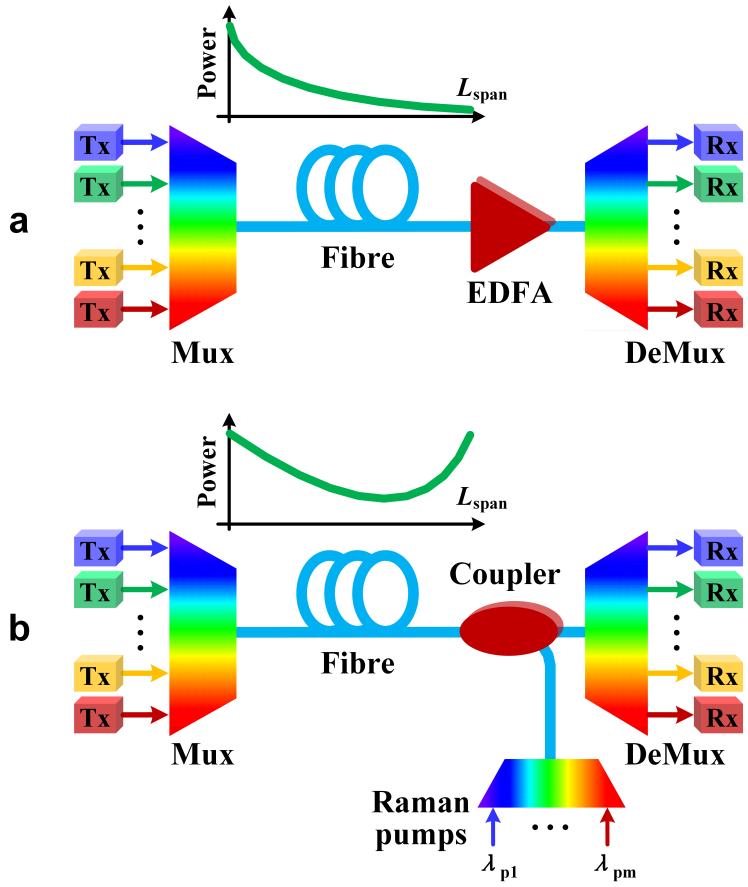

Figure 3.1: Schematic of WDM transmission systems applied with NLC. **a**. EDFA-amplified system and the power profile in each fibre span, **b**. Raman-amplified system and the power profile in each fibre span. Mux: multiplexer, DeMux: de-multiplexer.

3.1 Theoretical Model

Considering an EDFA- and a Raman-amplified Nyquist-spaced WDM dispersion-unmanaged coherent fibre communication system as shown in Fig. 3.1, the

system performance can be estimated in terms of SNR based on GN models [28, 43, 68, 130] with the consideration of ASE noise, fibre nonlinearities and TRx noise, whose expression based on Eq. (2.79) is given by

$$\mathrm{SNR} \triangleq \frac{P}{\sigma^2_{\mathrm{eff}}} \approx \frac{P}{P_{\mathrm{TRx}} + P_{\mathrm{ASE}} + P_{\mathrm{s-TRx}} + P_{\mathrm{s-ASE}} + P_{\mathrm{s-s}}}. \tag{3.1}$$

Assuming the contribution of TRx noise from the Tx is equal to that from the Rx and the NLC is only applied at the Rx side, based on Eq. (2.80) and Eq. (2.82), the TRx noise and the nonlinear beating between signals and TRx noise components can be respectively given by [33]

$$P_{\mathrm{TRx}} = \mathrm{SNR}^{-1}_{\mathrm{TRx}} \cdot P\,, \tag{3.2}$$

$$P_{\mathrm{s-TRx}} = \frac{3}{2}\,\mathrm{SNR}^{-1}_{\mathrm{TRx}} \cdot P_{\mathrm{s-s}}\,, \tag{3.3}$$

where $P_{\mathrm{s-s}}$ is given by Eq. (2.58).

Soft-decision mutual information (MI) can be calculated based on an AWGN model for AIRs [38, 39], and this is suitable for the optimum emitted power regimes in dispersion-unmanaged optical transmission using EDC or NLC [39,43]. In a discrete-time memoryless AWGN channel, assuming random complex input symbols X and output symbols Y, the relationship $X = Y + Z$ is given in each polarisation. The Z stands for the complex input-independent, zero-mean, identically distributed, symmetric circularly Gaussian random variable. The variance of Z is approximately equal to the effective variance σ^2_{eff} in

Eq. (3.1). Symbol-wised soft-decision MI can be given by [36, 39]

$$\mathrm{MI} = \frac{1}{M} \sum_{x \in \mathcal{X}} \int_{\mathbb{C}} dy \, p_{Y \mid X}(y \mid x) \log_2 \frac{p_{Y \mid X}(y \mid x)}{\frac{1}{M} \sum_{x' \in \mathcal{X}} p_{Y \mid X}(y \mid x')}, \tag{3.4}$$

where $M \triangleq |\mathcal{X}|$ is the cardinality of a square QAM-constellation, $\mathcal{X}$ is the set of transmitted random symbols, and $\mathbb{C}$ is the set of complex numbers. The Gaussian conditional probability density function in Eq. (3.4) is given by

$$p_{Y \mid X}(y \mid x) = \frac{1}{\pi \sigma_{\mathrm{eff}}^2} \exp\left(-\frac{|y - x|^2}{\sigma_{\mathrm{eff}}^2} \right), \tag{3.5}$$

where x and y are the realisations of X and Y, respectively.

The overall system AIR is computed as [37–39, 42, 127]

$$\mathrm{AIR} = 2 N_{\mathrm{ch}} R \cdot \mathrm{MI}. \tag{3.6}$$

Because nonlinear distortion is more severe in the central channel than in the outer channel, Eq. (3.4) based on Eq. (2.59) is basically a lower bound estimate of the AIR.

3.2 Results and Discussion

3.2.1 Digital Nonlinearity Compensation

According to the mentioned theoretical model, AIRs of $C-$band communication systems amplified by EDFA employed with EDC, partial bandwidth and full-field digital NLC, are investigated. An ideal scheme (no TRx noise limitation) and a more practical scheme (TRx SNR of 25 dB) are employed

to explore the performance of the NLC in $C-$band optical transmissions. Detailed system parameters are shown in Table 3.1. PMD is neglected in this chapter since TRx noise greatly exceeds its effect [33]. Phase noise from the Tx and LO lasers and the frequency offset are also neglected.

Table 3.1: Transmission Systems Parameters

Parameters	**Values**
Central wavelength (λ_0)	1550 nm
Channel spacing	32 GHz
Symbol rate (R)	32 GBd
Span length (L)	80 km
Attenuation coefficient (α)	0.2 dB/km
Number of channels (N_{ch})	151
Nonlinear coefficient (γ)	1.2 /W/km
CD coefficient (D)	17 ps/nm/km
CD slope coefficient (S)	0.067 ps/nm^2/km
EDFA noise figure (NF)	4.5 dB
Raman pump power (P_{p})	5 $\times$ 680 mW
Raman pump loss (α_{p})	0.25 dB/km

In the scenario of the NLC scheme, the bandwidth of single-channel NLC is 32 GHz, and the currently practical possible digital NLC bandwidth is 250 GHz [131].

Fig. 3.2 shows the AIR as a function of transmission distance with various modulation formats in a TRx-noise-free $C-$band communication system using NLC and EDC. It can be observed that for DP-QPSK, the systems using EDC, partial bandwidth NLC and FF-NLC display identical (saturated) AIR over the transmission distance of 10,000 km. This indicates that in a TRx-noise-free $C-$band communication system, applying DP-QPSK, no NLC is required to improve the AIR of the system up to 10,000 km. For DP-16QAM, NLC effectively improves AIRs at distances over 2,000 km. For DP-64QAM, NLC improves AIRs at transmission distances over 600 km. For DP-256QAM,

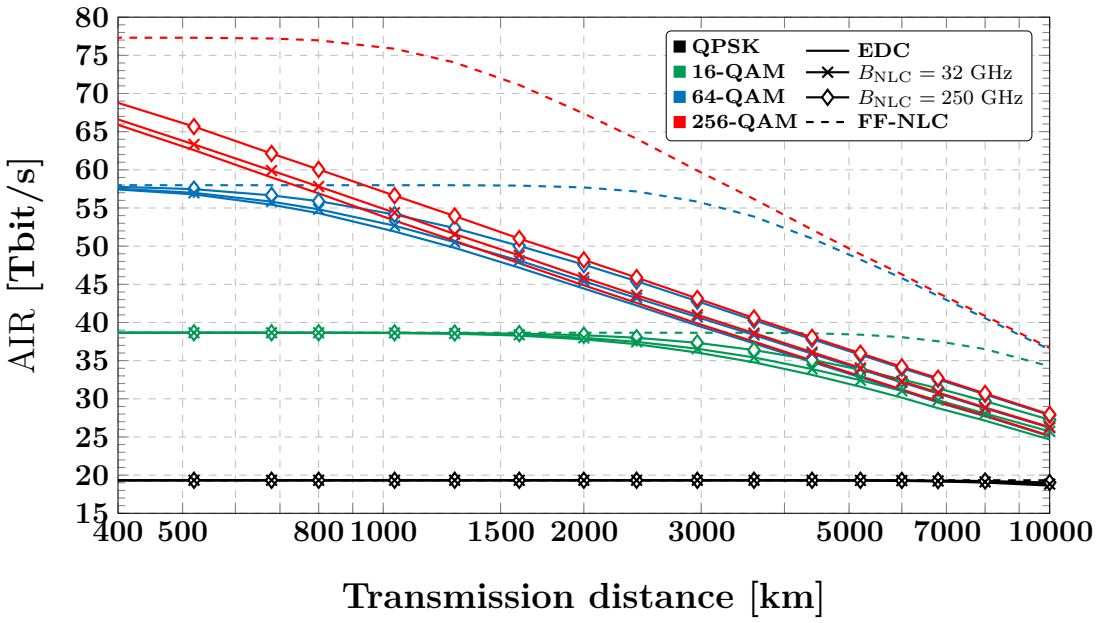

Figure 3.2: AIRs as a function of transmission distances for various modulation formats in ideal $C-$band (∼4.8 THz) EDFA-amplified transmission systems (without TRx noise).

NLC is efficient for all distances considered that begin from 400 km. It is noteworthy that for 250-GHz NLC cases, the DP-64QAM system shows similar AIRs to the DP-256QAM system when the distance exceeds 3000 km. The maximum constellation size considered here is 256QAM, a choice made through deliberation to align with the requirements of long-haul optical communication systems [11, 21, 132, 133].

Further investigation of the impact of TRx noise on AIRs has been conducted to include a case that is closer to practical scenarios. Fig. 3.3 shows the AIRs as a function of the transmission distances for various modulation formats in a $C-$band transmission system with 25 dB TRx SNR. It is demonstrated that for DP-QPSK systems NLC is not necessary for increasing AIR when the transmission distance is up to 10,000 km. For DP-16QAM, similar to the scenario of no TRx noise, the NLC enhances AIRs when the transmis-

sion distance is longer than 2000 km. For the DP-64QAM and DP-256QAM cases, employing the NLC raises AIRs overall considered distances, including from 400 to 10,000 km. It can also be observed that for EDC and NLC with bandwidths of 32 GHz and 250 GHz, when the transmission distance exceeds 2000 km, AIRs of DP-64QAM systems are similar to that of DP-256QAM systems. By comparing the results of considered $C-$band systems without and with TRx noises, it may be found that the TRx noise limitation has a minor influence on AIRs of DP-QPSK and DP-16QAM systems, while the performance degradation of DP-64QAM and DP-256QAM modulation formats is more significant. The MI-based AIR is for coded modulation based on nonbinary codes or multilevel codes multi-stage decoding [39, 134]. However, the generalized mutual information (GMI)-based AIR is the quantity for the performance estimation of the system with binary FEC (with bit-interleaved coded modulation or with parallel, independent decoding of the individual levels) [36, 135, 136]. Adopting the approach in [136], GMI-based AIRs for $C-$band EDFA-amplified systems with a 25 dB TRx SNR limitation were calculated as well and the results are shown in Fig. 3.4. A corresponding trend to that in Fig. 3.3 is evident in Fig. 3.4, where the efficiency of NLI on enhancing AIRs depends on the modulation formats and transmission distances.

The Raman-amplified systems applied with digital NLC have also been investigated. Fig. 3.5 illustrates the AIRs as a function of transmission distance for various modulation formats in a $C-$band transmission without the TRx noise limitation. Similar to the systems amplified by EDFA, it has been found that for DP-QPSK systems (transmission distances up to 10,000 km), NLC is not essential for the increase of AIRs because the AIRs are always at the highest value of saturation. For DP-16QAM, NLC becomes efficient in raising

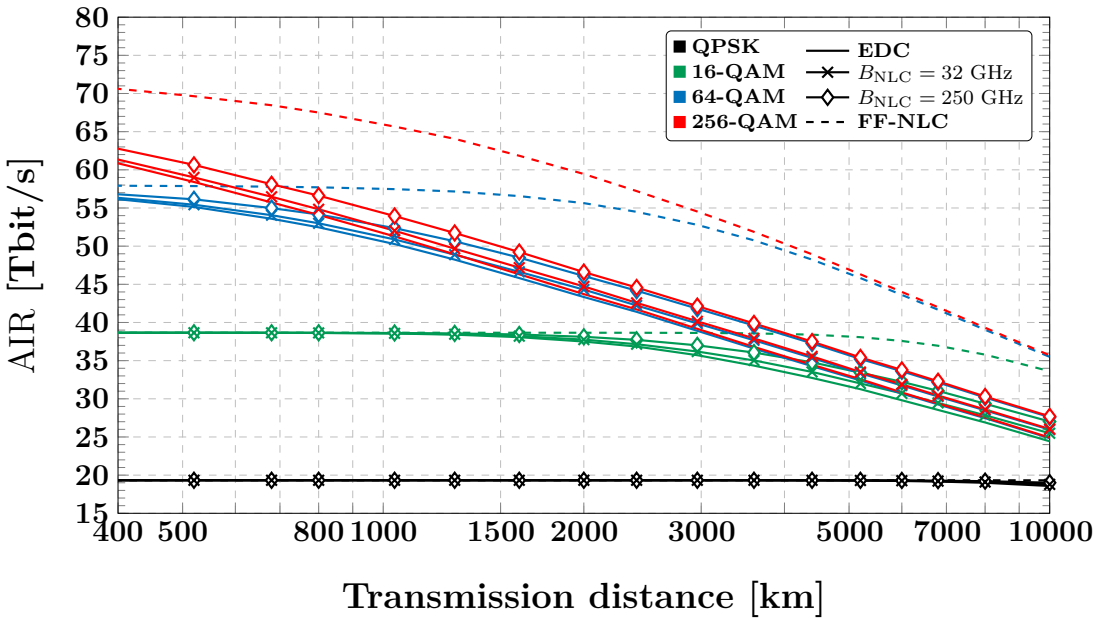

Figure 3.3: AIRs as a function of transmission distances for various modulation formats in $C-$band (∼4.8-THz) EDFA-amplified transmission systems (with a 25 dB TRx SNR limitation).

AIRs when transmission distances are longer than 3000 km. For DP-64QAM systems, the NLC is essential when transmission distances are beyond 1000 km, while for DP-256QAM, the NLC is effective for all considered transmission distances ranging from 400 km to 10,000 km.

A practical investigation of Raman-amplified $C-$band communication systems with the consideration of the TRx SNR limitation of 25 dB has also been conducted. The AIR as a function of the transmission distance for various modulation formats is shown in Fig. 3.6. Similar to the analysis above, the NLC is not essential for the DP-QPSK scheme for raising AIRs with transmission distances less than 10,000 km. For the scenario of the DP-16QAM system, NLC significantly enhances AIRs when the distances exceed 3000 km. For the DP-64QAM scheme, NLC is efficient when the distance is longer than 600 km. For all considered DP-256QAM systems, the NLC enhances the

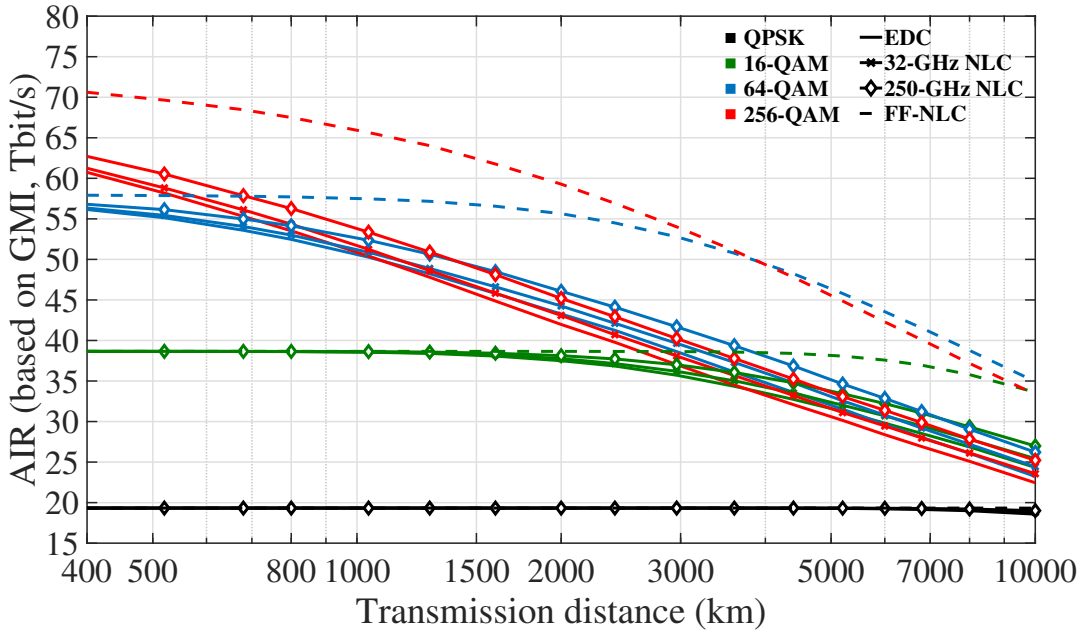

Figure 3.4: GMI-based AIRs as a function of transmission distances for various modulation formats in $C-$band EDFA-amplified systems (with a 25 dB TRx SNR limitation).

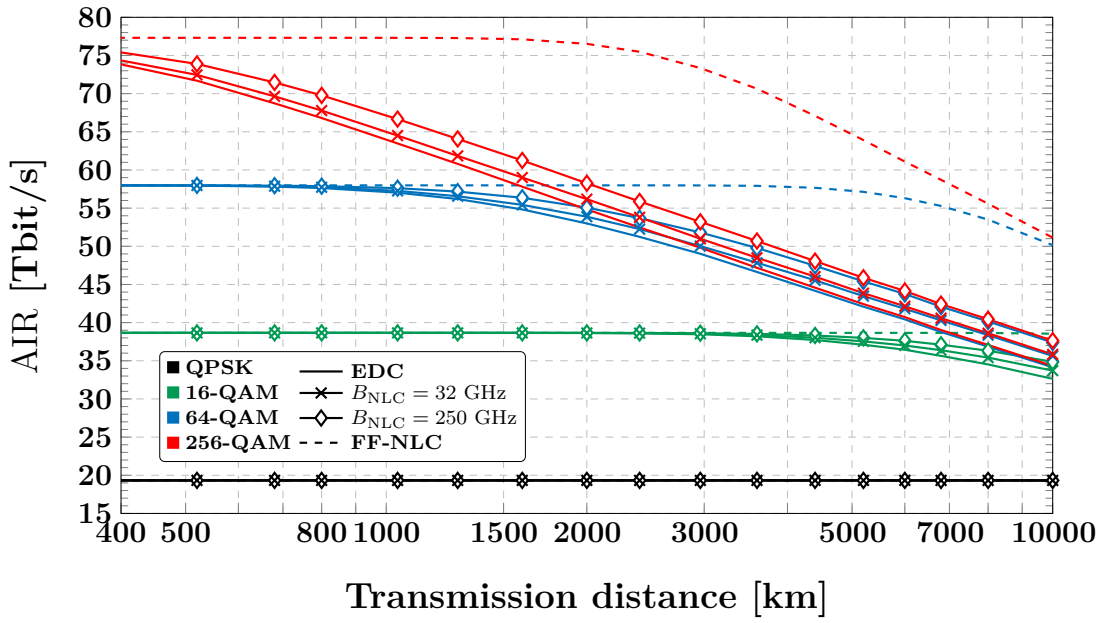

Figure 3.5: AIRs as a function of transmission distances for various modulation formats in ideal $C-$band Raman-amplified systems (without TRx noise).

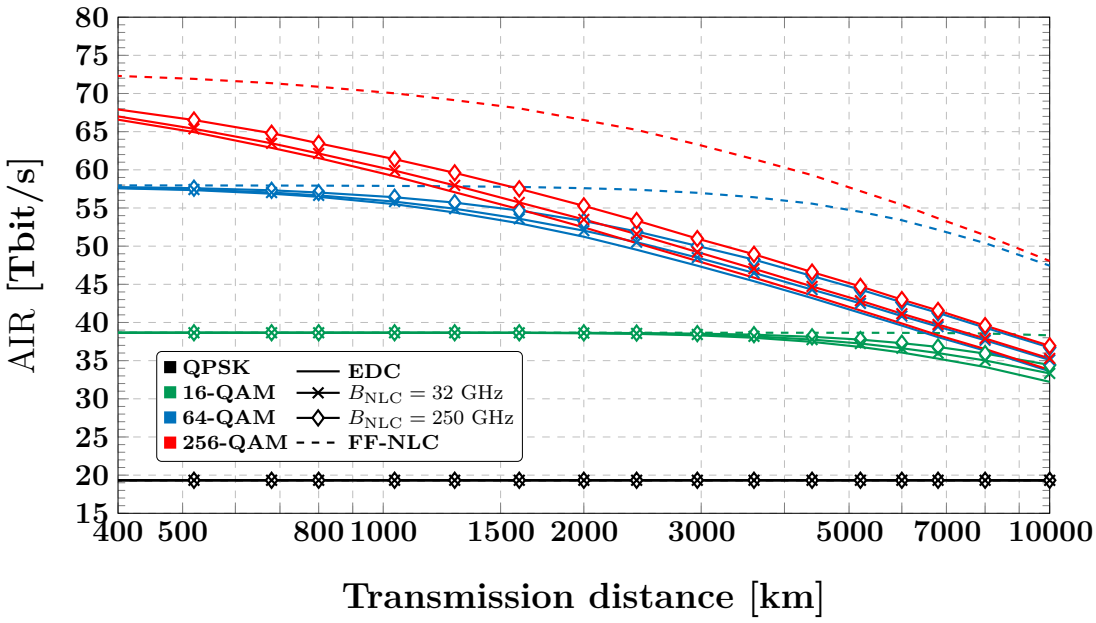

Figure 3.6: AIRs as a function of transmission distances for various modulation formats in Raman-amplified $C-$band systems (with a 25 dB TRx SNR limitation).

AIRs. Additionally, comparing Fig. 3.2 and Fig. 3.6, the smaller gain from NLC over EDC with Raman amplifiers rather than lumped amplifiers can be observed for shorter transmission distances. This is due to the fact that in this scenario, for Raman amplification systems, the launched optimal power is lower compared to EDFA systems. As a result, the generated nonlinear effects are also reduced, leading to a more limited enhancement of the AIR through NLC.Similar phenomena could also be observed in Fig. 3.7 in terms of GMI-based AIRs.

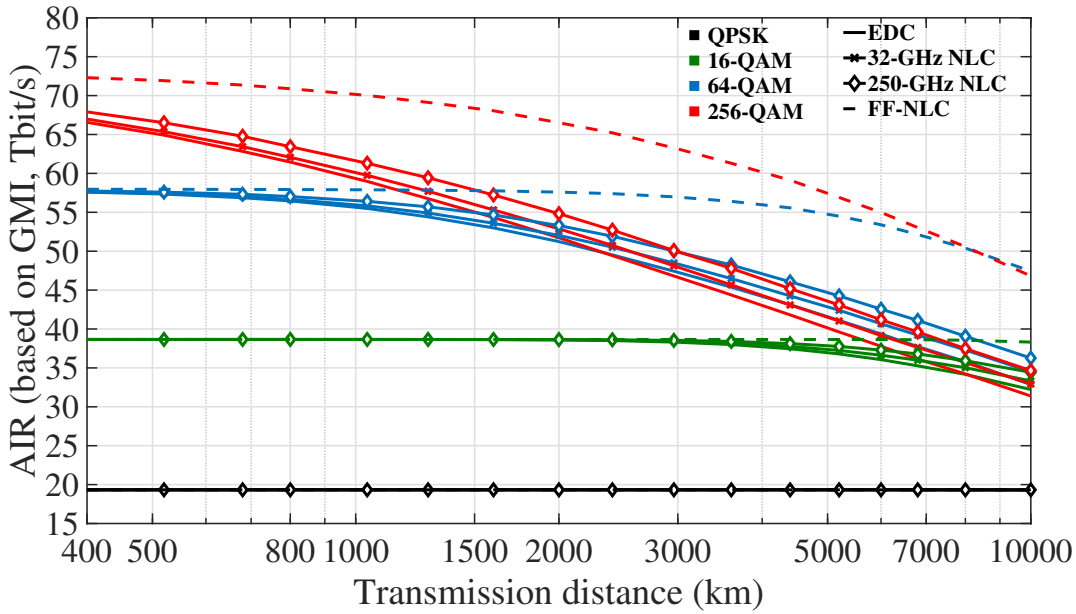

Figure 3.7: GMI-based AIRs as a function of transmission distances for various modulation formats in $C-$band DRA-amplified systems (with a 25 dB TRx SNR limitation).

3.2.2 Optical Nonlinearity Compensation (Optical Phase Conjugation)

As has been previously analysed, the application of OPC is an alternative promising method for mitigating nonlinear degradation. Generally, the technique benefits from distributed amplification. Therefore the fully loaded $C-$band transmissions with Raman amplification with and without the TRx noises limitation were investigated. The mid-link OPC technique was employed.

The AIRs as a function of the transmission distance for various modulation formats in the $C-$band OPC-applied transmission systems without the consideration of TRx noise are shown in Fig. 3.8. It can be observed that the NLC is not necessary for DP-QPSK cases when the distance is in the range of 400 km to 10,000 km, as the AIRs are at the maximum saturated values. For

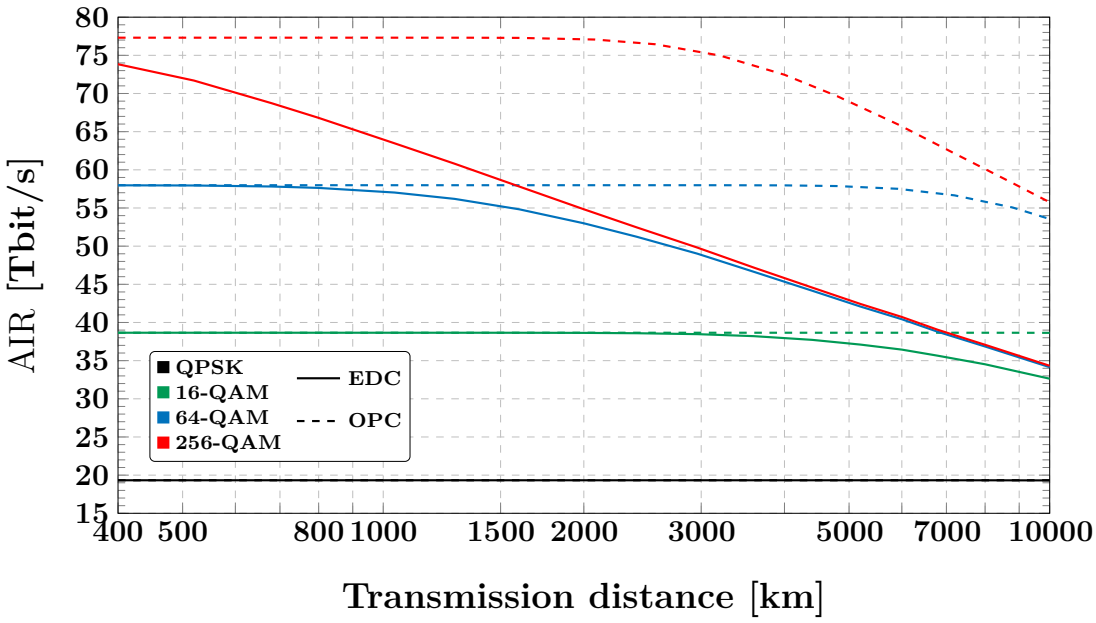

Figure 3.8: AIRs as a function of transmission distances in ideal $C-$band Raman-amplified systems using OPC (without TRx noise and OPC loss).

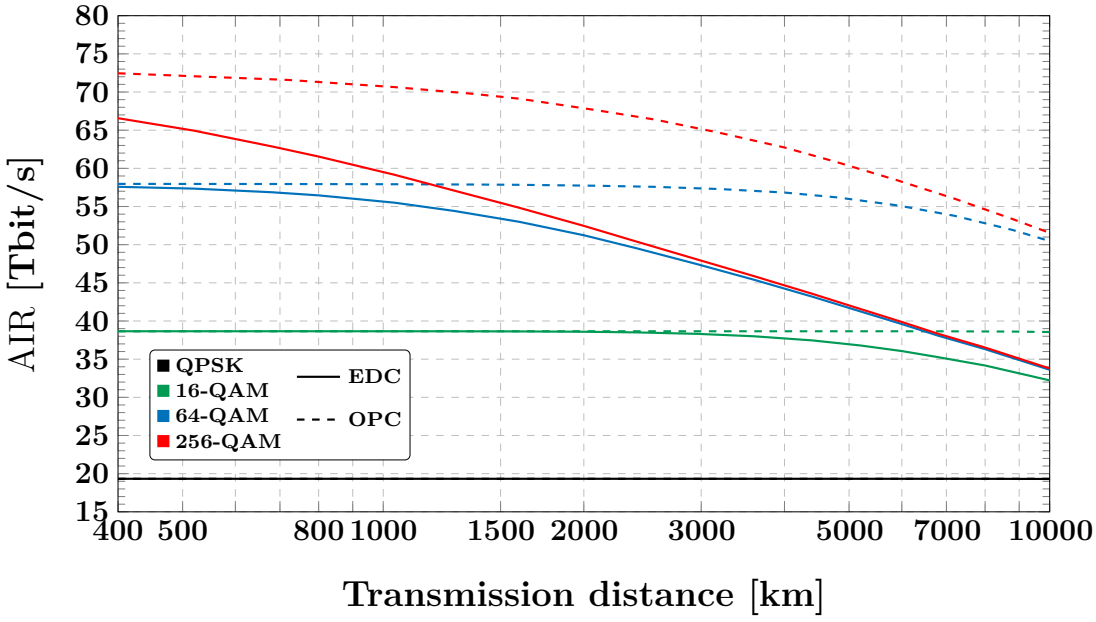

Figure 3.9: AIRs as a function of transmission distances in practical $C-$band Raman-amplified systems using OPC (with a 25 dB TRx SNR limitation and an OPC loss of 10 dB).

the DP-16QAM systems, the application of the OPC is effective in raising the system AIRs when the transmission distance is beyond 3000 km. For the DP-64QAM systems, this effective distance decreases to 800 km, whereas for the DP-256QAM systems, OPC effectively enhances the AIRs for all considered distances ranging from 400 to 10,000 km.

The influence of TRx noise on the performance of the system using OPC in terms of AIRs has also been further studied. The TRx SNR limitation is assumed as 25 dB for a fully-loaded $C-$band optical communication system. The loss of the applied OPC device is set to 10 dB [21, 137, 138], and it can be compensated by an EDFA. Fig. 3.9 illustrates the AIR as a function of transmission distance for various modulation formats. The results indicate that for DP-QPSK, the reduction of AIRs caused by the TRx noise is marginal and as the rates are maximum, the NLC is not beneficial for all explored distances (400 to 10,000 km). For DP-16QAM systems, the impact of TRx noise is also negligible, and OPC at distances beyond 3,000 km becomes beneficial, which is similar to the scenario for the ideal $C-$band communication systems. For higher-order modulation formats, the degradation caused by TRx noise is more severe. For DP-64QAM, AIR gain is observed over distances of about 500 km, and for DP-256QAM, OPC is effective over all distances examined from 400 to 10,000 km. Similar phenomena could also be observed in Fig. 3.10 in terms of GMI-based AIRs.

Notably, in this work, a fixed span length of 80 km has been considered for both the EDFA and Raman amplified transmissions for analyzing the DBP and OPC performance. Several reports indicate that the performance of DBP and OPC can be further enhanced with the optimized fibre span length [139–142]. Under such circumstances, the performance of AIRs with

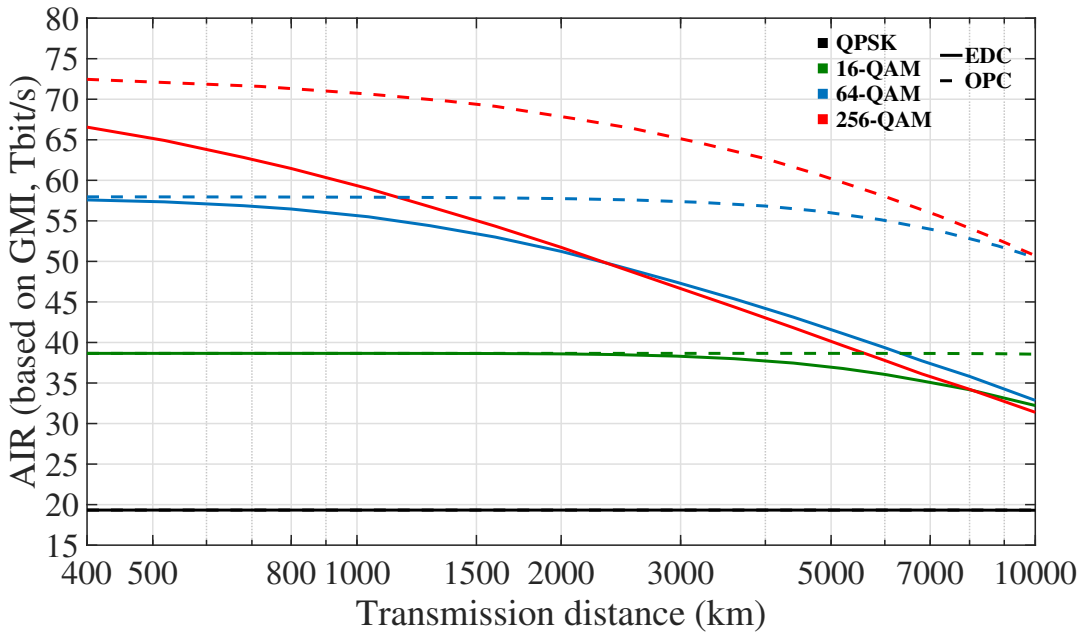

Figure 3.10: GMI-based AIRs as a function of transmission distances in practical $C-$band Raman-amplified systems using OPC (with a 25 dB TRx SNR limitation and an OPC loss of 10.

respect to transmission distance can also be improved accordingly in such optimized systems. Moreover, it is noteworthy that in a practical communication system, OPC cannot fully compensate for the fibre nonlinearity because of the asymmetric power profile and dispersion slope. Furthermore, optical communication systems amplified by EDFAs are the most common deployment in current optical network infrastructures. The OPC in the middle of the link cannot, in principle, fully compensate for the nonlinear distortion, because the propagated power profile in the link before and after the OPC is asymmetric. The combined operation of OPC and DBP could be necessary to optimize the performance of the NLC in such a system.

3.3 Summary

The AIRs benefits obtained by using digital and optical NLC are comprehensively studied in fully-loaded $C-$band (~ 4.8 THz) Nyquist-spaced WDM optical fibre transmission systems with the consideration of various modulation formats. The schemes of both EDFA and Raman amplification have been employed, and the TRx noise has also been considered for the modelling of the practical $C-$band communication system. It showed that in the wideband transmission scenario, the effectiveness of both DBP and OPC in improving AIR depends on the specific transmission distance and modulation format. For higher-order modulation formats, NLC becomes effective from a shorter system distance. In particular, NLC is not essential for DP-QPSK systems for the considered transmission distances of up to 10,000 km. Additionally, TRx noise considered in the practical system has a negligible influence on the AIRs for the cases of DP-QPSK and DP-16QAM, whereas it limits the AIRs more essentially for the DP-64QAM and DP-256QAM transmissions.

This work provides perspectives on the application and enhancement of digital and optical NLC techniques in both EDFA- and Raman-amplified fully-loaded $C-$band transmission systems while taking into account the limitations of practical transceivers.

Chapter 4

Performance of Nonlinear Coherent Optical Systems Influenced by EEPN

In this chapter, the impact of EEPN on nonlinear optical fibre transmission systems through split-step Fourier simulations and obtain accurate predictions of the system's performance is investigated. Therefore, the GN model accounting for the impact of EEPN is described to predict the performance of long-haul Nyquist-spaced WDM coherent communication systems with both EDC and digital NLC. Both the accuracy and effectiveness of the analytical approach were verified via split-step Fourier numerical simulations. The performance of single- and multi-channel systems with and without the EEPN was evaluated and compared. The results indicate that EEPN can greatly degrade the system's performance. The introduction of EEPN into the GN model is essential for an accurate performance evaluation of dispersion-unmanaged optical communication systems accounting for LPN from Tx and LO. Moreover, the

maximum system reaches for different laser linewidths and signal modulation formats are predicted and analysed.

The rest of this chapter is organized as follows: Section 4.1 describes the analytical model for evaluating the impacts of amplifier noise, NLI and EEPN. Section 4.2 presents the transmission setup. Section 4.3 presents and discusses the simulation and analytical model results. Section 4.4 analyses the system maximum reach and the laser linewidth tolerance. Section 4.5 and 4.6 present the results of the simulations considering TRx noise and PMD, respectively. Section 4.7 is the further analysis of the model application in high-speed wideband systems with considering various transmission rates, modulation formats and distances. Section 4.8 investigates the impact of EEPN effects on backwards-pumped distributed-Raman-amplified nonlinear coherent optical fibre system through both numerical simulations and the analytical model. Section 4.9 is the summary.

4.1 GN-EEPN Model

In this section, the analytical model is presented to predict the SNR in dispersion-unmanaged Nyquist-spaced coherent optical transmission systems in presence of EEPN, where the EDC and the NLC are applied respectively.

Considering such a transmission system, nonlinear distortions can be modelled as additive Gaussian noise, which is appropriate for signals distorted by moderate fibre nonlinearities and significant dispersion in long-haul transmission systems. The conventional GN model considers the distortion caused by NLI and ASE noise as shown in Eq. (2.57). With the consideration of the nonlinear interference between ASE and signals as presented in Section 2.5.4,

the system SNR is generally expressed as [25, 28]

$$\mathrm{SNR} = \frac{P}{P_{\mathrm{ASE}} + P_{\text{s-s}} + P_{\text{s-ASE}}}\,, \tag{4.1}$$

Considering an EDFA-amplified Nyquist-spaced system with multiple identical fibre spans, and accounting for the impact of input signal modulation format [26], based on Eq. (2.58), Eq. (2.70), Eq. (2.69) and Eq. (2.71), the signal-signal NLI noise power at the central channel has the following closed-form approximation [27]

$$\begin{aligned} P_{\text{s-s}} &\triangleq \eta\left(N, B\right) \cdot P^3 \\ &\approx \frac{8}{27}\frac{\gamma^2 N L_{\mathrm{eff}}}{\pi\left|\beta_2\right| R^2}\left\{N^{\varepsilon}\,\mathrm{asinh}\left(\frac{\pi^2}{2}\left|\beta_2\right| L_{\mathrm{eff}} \cdot N_{\mathrm{ch}}^2\, R^2\right)\right. \\ &\quad \left. - \chi\,\frac{10}{3}\frac{L_{\mathrm{eff}}}{L}\left[\mathrm{HN}\left(\frac{N_{\mathrm{ch}}-1}{2}\right)+1\right]\right\} \cdot P^3\,. \end{aligned} \tag{4.2}$$

The conventional GN model would significantly overestimate the system performance if the EEPN noise was not negligible. For more practical cases with considerable LPNs from Tx and Rx lasers, the EEPN contribution should be added to the estimation of SNR. Accounting for the EEPN effect, the updated expression of Eq. (4.1) is now given by

$$\mathrm{SNR} = \frac{P}{P_{\mathrm{ASE}} + P_{\text{s-s}} + P_{\text{s-ASE}} + \sigma_{\mathrm{EEPN}}^2 \cdot P}\,, \tag{4.3}$$

where σ_{EEPN}^2 is the variance of EEPN given by Eq. (2.47).

In the case of EDC, $P_{\text{s-ASE}}$ can be neglected as its contribution is much smaller than the P_{NLI}. When NLC is applied in the system, the signal-signal NLI P_{NLI} is greatly reduced. The signal-ASE interaction $P_{\text{s-ASE}}$, which is

neglected in the EDC case, becomes relatively significant and needs to be considered. The NLC considered in this section refers to the full-field compensation (i.e., applied to all signal bandwidths). Thus, the signal-signal NLI can be completely removed. The nonlinear interaction between the signals and EEPN effects should also be taken into account, as it happens when the signals pass through the NLC module. Fig. 4.1 shows the schematic of EEPNs and EEPN-signal interactions accumulation process in an optical communication system using NLC. In presence of EEPN, the model expressions for the case of EDC and NLC are given respectively by

$$\mathrm{SNR}_{\mathrm{EDC}} = \frac{P}{P_{\mathrm{ASE}} + P_{\text{s-s}} + \sigma^2_{\mathrm{EEPN}} \cdot P}\,, \tag{4.4}$$

$$\mathrm{SNR}_{\mathrm{NLC}} = \frac{P}{P_{\mathrm{ASE}} + P_{\text{s-ASE}} + \sigma^2_{\mathrm{EEPN}} \cdot P + P_{\text{s-EEPN}}}\,, \tag{4.5}$$

where $P_{\text{s-EEPN}}$ is the interaction between the signal and the EEPN effect due to the FWM process, and it is approximately estimated as $3\,\xi\,\eta\,(1, B)\ (\sigma^2_{\mathrm{EEPN}}/N) \cdot P^3$. This expression gives rise to an overestimation of the noise variance due to the signal-EEPN interaction. A more accurate evaluation of the signal-EEPN interaction can be found in Section 4.1.1. It is worth noting that in the presence of NLC, the amount of EEPN contribution is larger than that in the case of EDC. This happens due to the appearance of extra signal-EEPN interaction.

The optimum launch power for the EDC case can be obtained by setting the derivative of Eq. (4.4) to zero and solving the arising equation. Then the maximum SNR can be obtained by substituting the optimum launch power in Eq. (4.4). The optimum launch power and the corresponding maximum SNR

in the case of EDC are expressed as

$$P_{\mathrm{EDC,opt}} = \sqrt[3]{\frac{P_{\mathrm{ASE}}}{2N^{\varepsilon}\,\eta\,(1,N_{\mathrm{ch}})}}\,, \tag{4.6}$$

$$\max_{P}\left[\,\mathrm{SNR}_{\mathrm{EDC}}\,\right] = \frac{1}{\sigma^2_{\mathrm{EEPN}} + \sqrt[3]{\frac{27}{4}N^{\varepsilon+3}\,\eta\,(1,N_{\mathrm{ch}})\;P^2_{\mathrm{ASE}}}}\,. \tag{4.7}$$

Similarly, the optimum launch power and the corresponding maximum SNR for the use of NLC are described as

$$P_{\mathrm{NLC,opt}} \approx \sqrt{\frac{N}{3\xi\,\eta(1,N_{\mathrm{ch}})}}\,, \tag{4.8}$$

$$\max_{P}\left[\,\mathrm{SNR}_{\mathrm{NLC}}\,\right] \approx \frac{1}{\sigma^2_{\mathrm{EEPN}} + \sqrt{12\xi N\eta(1,N_{\mathrm{ch}})P^2_{\mathrm{ASE}}}}\,. \tag{4.9}$$

Here simple and accurate predictions of the optimum launch power and the achievable maximum SNR are provided for both the EDC and the NLC schemes when there exists considerable Tx and LO LPN in long-haul optical fibre communication systems.

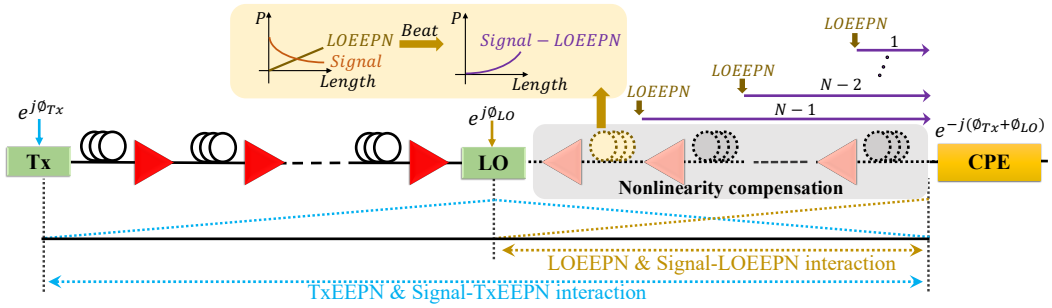

Figure 4.1: Schematic of EEPN and Signal-EEPN interactions accumulation process in an optical communication system using NLC.

4.1.1 Estimation of the Signal-EEPN Interaction

The corresponding PSDs for signal and noise contributions at the Nyquist rate can be respectively defined as follows

$$S(f) \triangleq \frac{P}{R}\,\mathrm{rect}\left(\frac{f}{\mathrm{B}}\right), \tag{4.10}$$

$$\begin{aligned} N_{\mathrm{EEPN}}(f \mid z) &\triangleq \frac{\sigma^2_{\mathrm{s-EEPN}}(z)\,P}{R}\,\mathrm{rect}\left(\frac{f}{\mathrm{B}}\right) \\ &\equiv \sigma^2_{\mathrm{s-EEPN}}(z) \cdot S(f), \end{aligned} \tag{4.11}$$

where B denotes the total WDM bandwidth, z is the transmission distance, $\sigma^2_{\mathrm{s-EEPN}}(z)$ is the variance of the signal-EEPN interaction.

Taking the transmission distance dependency of the EEPN variance in Eq. (4.11) into account gives rise to the following modifications in the GN-model-based expressions

$$P_{\mathrm{s-EEPN}} \approx 3\,\xi\,\kappa\,\eta_{\mathrm{s-EEPN}} \cdot P^3, \tag{4.12}$$

where the nonlinear interference coefficient after one fibre span propagation is evaluated at the centre channel, yields

$$\begin{aligned} \eta_{\mathrm{s-EEPN}} =& \frac{16\,\gamma^2}{27R^2} \int_{-\mathrm{B}/2}^{\mathrm{B}/2} \int_{-\mathrm{B}/2}^{\mathrm{B}/2} df_1\,df_2 \\ & \cdot \rho_{\mathrm{EEPN}}(f_1, f_2, 0 \mid L)\ \mathrm{rect}\left(\frac{f_1+f_2}{\mathrm{B}}\right), \end{aligned} \tag{4.13}$$

where the FWM efficiency is now being defined as follows

$$\rho_{\mathrm{s-EEPN}}\left(f_1, f_2, 0 \,|\, L\right) = \int_0^L dz\, z\, e^{-\alpha z}\, e^{j\,\Delta\beta(0,f_1,f_2)\,z} = \frac{1 - \left[1 + \left(\alpha - j\,\Delta\beta\left(0, f_1, f_2\right)\right) L\right] \cdot e^{-\left(\alpha - j\,\Delta\beta(0,f_1,f_2)\right) L}}{\left(\alpha - j\,\Delta\beta\left(0, f_1, f_2\right)\right)^2}\,, \tag{4.14}$$

where the FWM mismatch factor $\Delta\beta\left(f, f_1, f_2\right) \approx 4\pi^2[\,\beta_2 + \pi\left(f_1 + f_2\right)\beta_3\,] \cdot \left(f_1 - f\right)\left(f_2 - f\right)$, with β_2 and β_3 being the 2^{nd} and 3^{rd}-order dispersion coefficients. In Eq. (4.12), the following notation has also been introduced

$$\kappa \triangleq \frac{\sigma^2_{\mathrm{EEPN}}\left(L\right)}{N \cdot L} = \frac{\pi c\, D\, f_{3\mathrm{dB}}\, R}{2 f_0^2}\,.$$

It is rather evident that a more accurate analysis of signal-EEPN interaction becomes more complicated, whilst it has been observed that the amount of signal-EEPN interaction itself remains marginal compared to other contributions in the reference SNR equation Eq. (4.5). Therefore, a simpler approach has been used in the model, which essentially overestimates the impact of signal-EEPN interaction as previously described.

4.2 Transmission System

Numerical simulations were performed to assess the impact of the EEPN on the system performance. The simulation setup of a Nyquist-spaced 32-GBd DP-16QAM WDM optical transmission system is described in Fig. 4.2. At the Tx, a 32-GHz spaced laser comb was used as the source of the optical carrier. The symbol sequence of the transmitted signal in each channel was

fully random and independent. A root-raised cosine (RRC) filter with 0.1% roll-off was employed for Nyquist pulse shaping (NPS). A recirculating fibre loop was used in the transmission link. SSMF was employed with a span length of 80 km. The signal propagation over the optical fibre was simulated based on the split-step Fourier solution of the Manakov equation [102, 143]. After each span of fibre, an EDFA with a 4.5 dB noise figure was applied to exactly compensate for the loop loss. At the Rx, the signal was mixed with a LO laser for coherent detection. Two scenarios were considered: 1) LO linewidth of 100 kHz to analyse the impact of EEPN; 2) LO linewidth of 0 Hz as a benchmark for no EEPN applied in the system. The signals were detected by photodetectors and sampled by ADCs.

In DSP modules, an RRC filter was applied before the NLC (or EDC) module to select the NLC bandwidth. A frequency domain equalizer (FDE) was used as the EDC module [21]. The Rx-side NLC was applied based on the reverse split-step Fourier solution of the Manakov equation [144]. An ideal CPE was used for the compensation of phase noise, achieved by using the conjugate multiplication between the received signal and the extracted intrinsic LPN. This is to focus on the impact from EEPN, where no amplitude noise mitigation effect is employed in the CPE module [108]. The matched filter was used to select the observed (centre) channel and remove the out-of-band noise, and it was again achieved by an RRC filter with a roll-off factor of 0.1%. Finally, the performance of the central channel was estimated in terms of the SNR. The laser frequency offset and PMD were neglected in the simulation. Detailed parameters of the transmission system were given in Table 4.2.

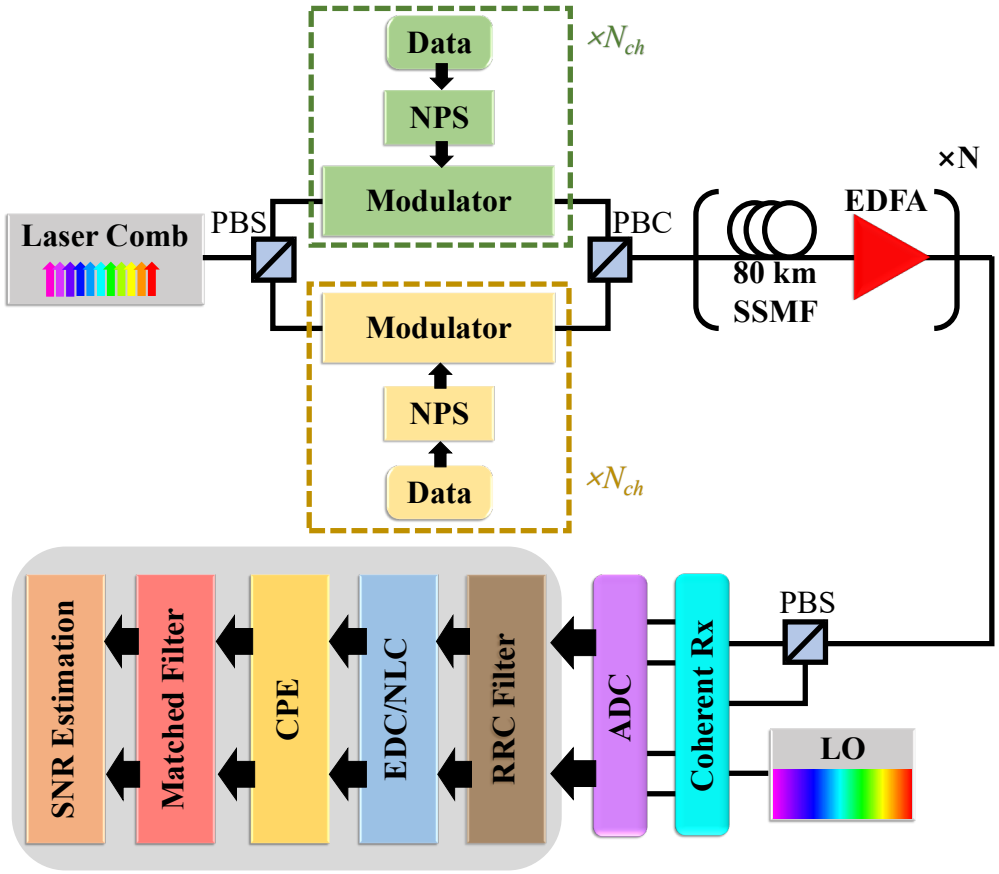

Figure 4.2: Simulation setup of DP-16QAM Nyquist-spaced WDM transmission system using EDC or NLC. PBS: polarisation beam splitter; PBC: polarisation beam combiner.

4.3 Results and Analyses of Numerical Simulations

Numerical simulations and analytical model predictions have been carried out for the DP-16QAM system over a transmission distance of 2000 km (25 fibre spans). Fig. 4.3, Fig. 4.4 (a) and Fig. 4.4 (b) show the results for the cases of single-channel, 5-channel and 9-channel transmission, respectively. Lines represent predictions from the proposed model expression, and markers represent simulation results. It is observed that the simulation results are highly consis-

Table 4.1: Transmission System Parameters

Parameters	Values
Center wavelength	1550 nm
Attenuation coefficient	0.2 dB/km
CD coefficient (D)	17 ps/nm/km
Nonlinear coefficient (γ)	1.2 /W/km
EDFA noise figure (NF)	4.5 dB
Total fibre length ($N \times L$)	25×80 km
Symbol rate (R)	32 GBd
Channel spacing	32 GHz
Number of channels (N_{ch})	$\{1, 5, 9\}$
Modulation format	16QAM
Roll-off factor	0.1%
Number of symbols	2^{20}
LO laser linewidth	$\{0, 100\}$ kHz

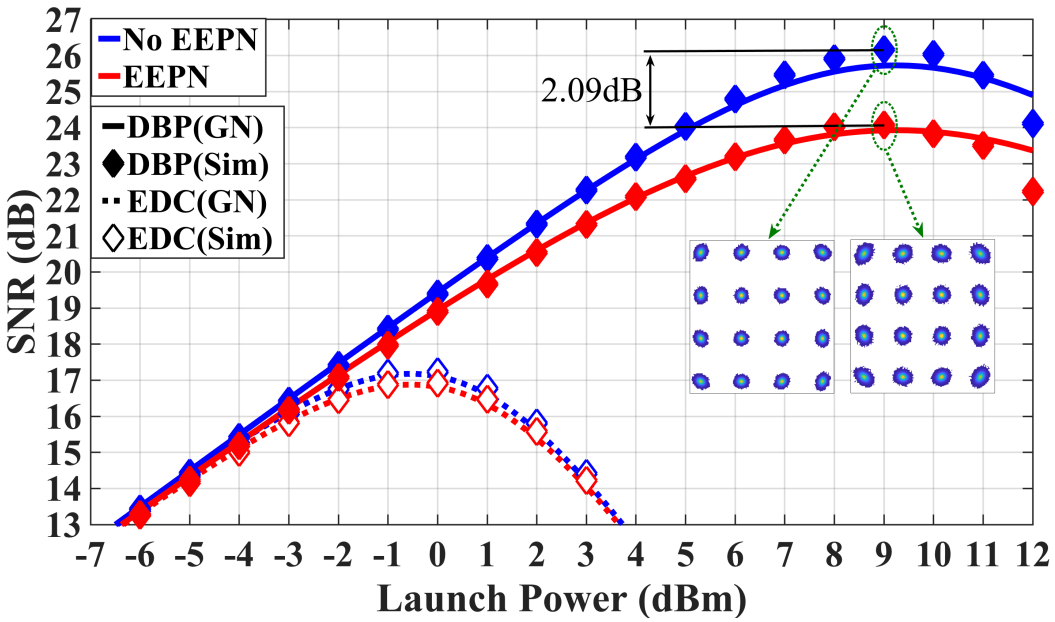

Figure 4.3: The SNR of the central channel as a function of launch power per channel in the DP-16QAM Nyquist-spaced system with the single-channel transmission. The constellations at the optimal simulation performance in the NLC systems are shown in the insets.

tent with the model in both cases of EDC and NLC. From Fig. 4.3, 4.4 (a), and 4.4 (b), it can also be found that the EEPN has an important impact on

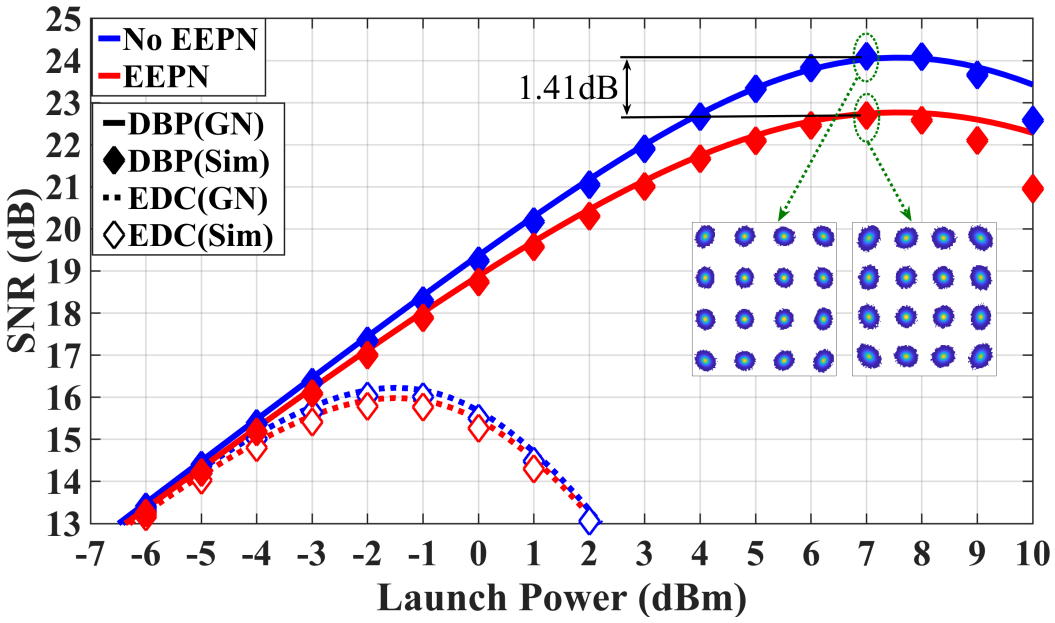

(a)

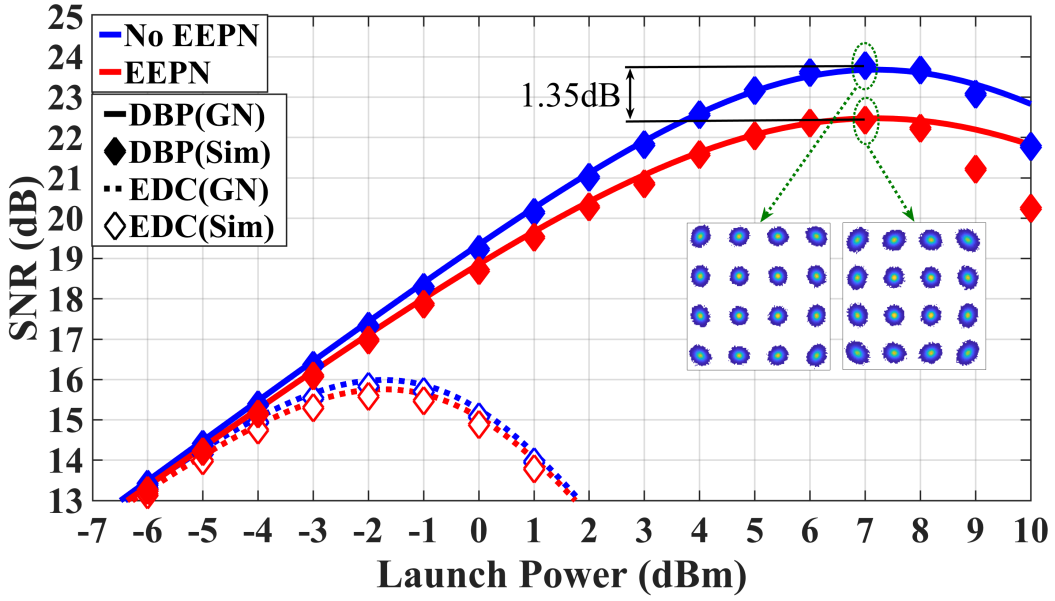

(b)

Figure 4.4: The SNR of the central channel as a function of launch power per channel in the DP-16QAM Nyquist-spaced system with the 5-channel (a) and 9-channel (b) transmission. The constellations at the optimal simulation performance in the NLC systems are shown in the insets.

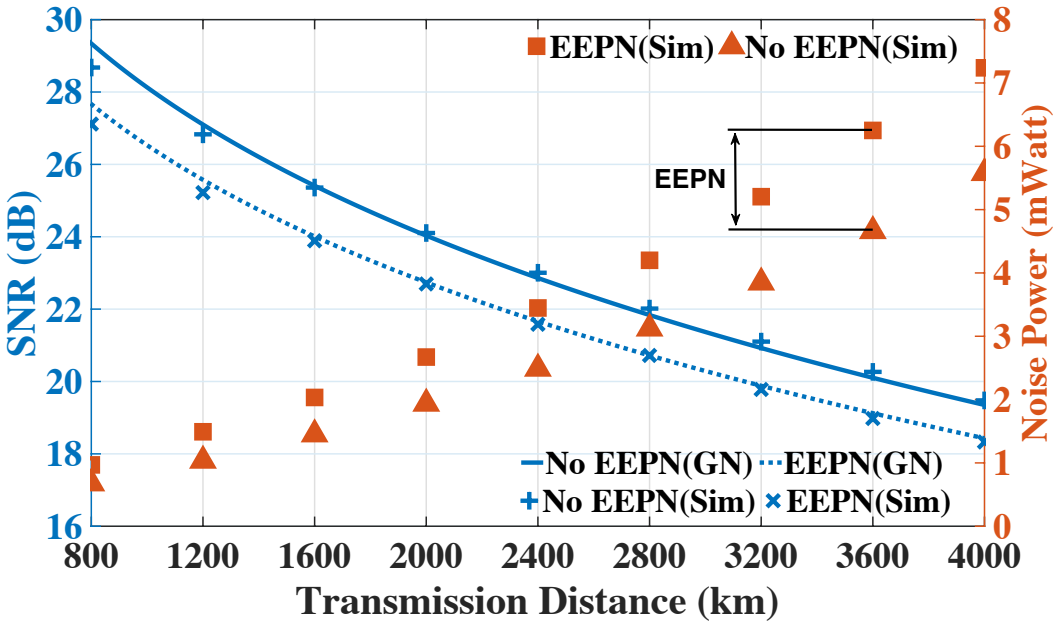

Figure 4.5: The SNR (left side) and noise power (right side) of the central channel as a function of transmission distance in the DP-16QAM 5-channel Nyquist-spaced system at 7 dBm per channel launched power using NLC, with and without EEPN. Lines represent the model in Eq. (4.5), and markers represent results obtained by simulations.

the performance of NLC. This shows that the EEPN variance is significantly smaller than the signal-signal interaction in Eq. (4.4) but is considerably large compared to the signal-ASE interaction in Eq. (4.5). For the NLC case, it is found that the SNR with EEPN is 2.09 dB lower than that without EEPN at the optimal power of 9 dBm for the single-channel system. Similarly, the gaps are 1.41 dB and 1.35 dB at 7 dBm for the 5-channel and the 9-channel transmission systems, respectively. Their constellations at the optimum powers (without and with EEPN) are also shown in the insets. It can be seen that the EEPN causes significant distortion to the signal constellations.

Fig. 4.5 shows the SNR (left side) and the noise power (right side) of the central channel as a function of transmission distance in the DP-16QAM

5-channel Nyquist-spaced system using NLC at a fixed launch power of 7 dBm, with and without the application of EEPN. It can be observed that the additional degradation of SNR caused by EEPN exceeds 1 dB for all considered transmission distances from 800 to 4000 km. The deviation in the conventional GN model caused by neglecting the EEPN is significant. The noise power in the system is also presented in Fig. 4.5. Square markers indicate the total power of EEPN, NLI, and ASE noise generated in the transmission system with a LO laser linewidth of 100 kHz, while triangle markers represent the power of NLI and ASE noise for the ideal LO laser system (neglecting the LO linewidth). Therefore, the "gap" between these two markers indicates the power of EEPN, as shown in Fig. 4.5 (right side). The continuous growth of EEPN power can be observed with the increase of the transmission distance (from 0.14 mW at 800 km to 1.66 mW at 4000 km, a total increase of $\sim$ 12 times).

4.4 Maximum Reach Analyses

The maximum reach and the LPN tolerance in optical communication systems are discussed based on the analytical model. Calculated SNRs from Section 4.1 are converted to BERs for a clear analysis [21]. Modulation formats of DP-QPSK, DP-16QAM, and DP-64QAM are considered. Detailed parameters used for estimations, such as centre wavelength, fibre parameters, symbol rate and EDFA noise figure etc. are the same as those listed in Table 4.2.

Fig. 4.6 shows the achievable BER as a function of transmission distance in the single-channel Nyquist-spaced system, with and without EEPN (LO laser linewidth of 100 kHz and 0 Hz, respectively) for the modulation

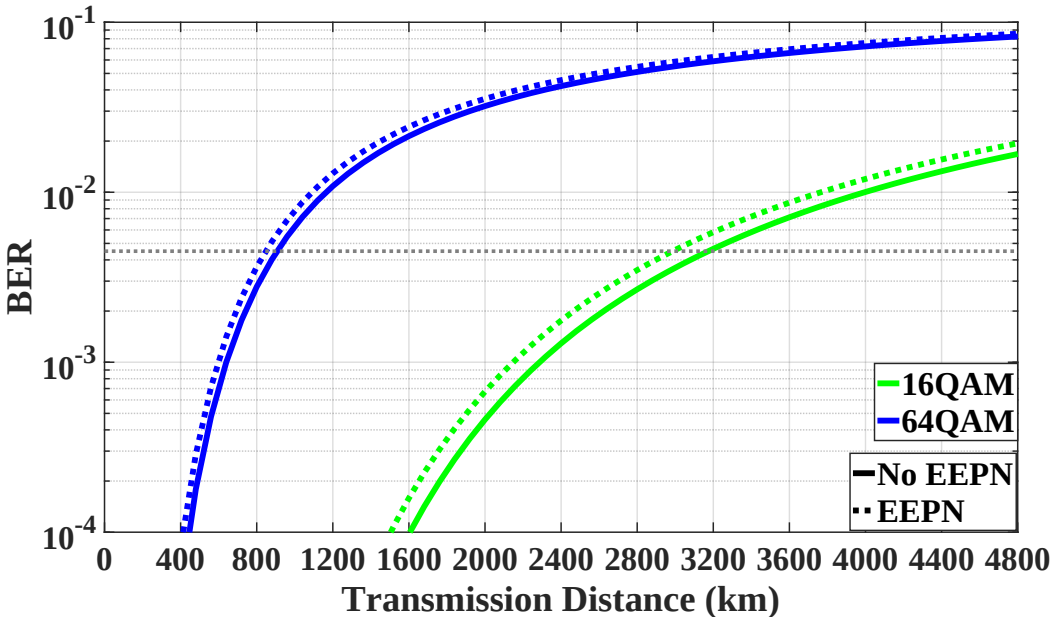

(a)

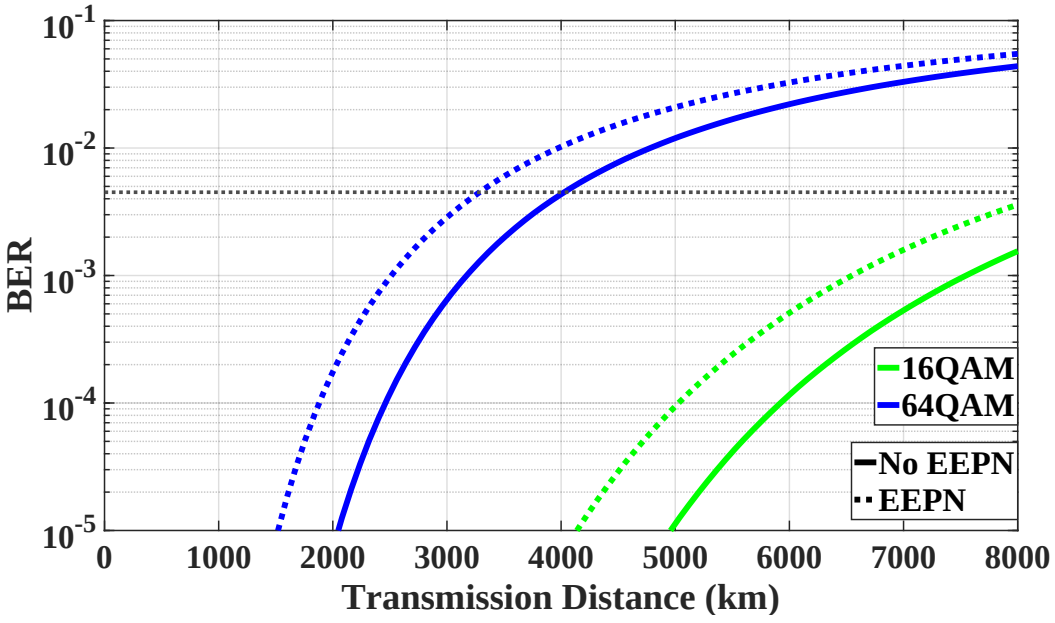

(b)

Figure 4.6: The theoretical BER as a function of transmission distance in the single-channel system using EDC only (a) and NLC (b), with and without EEPN for the modulation format of 16QAM and 64QAM. The black dotted line indicates the FEC threshold (BER of 4.5×10^{-3}).

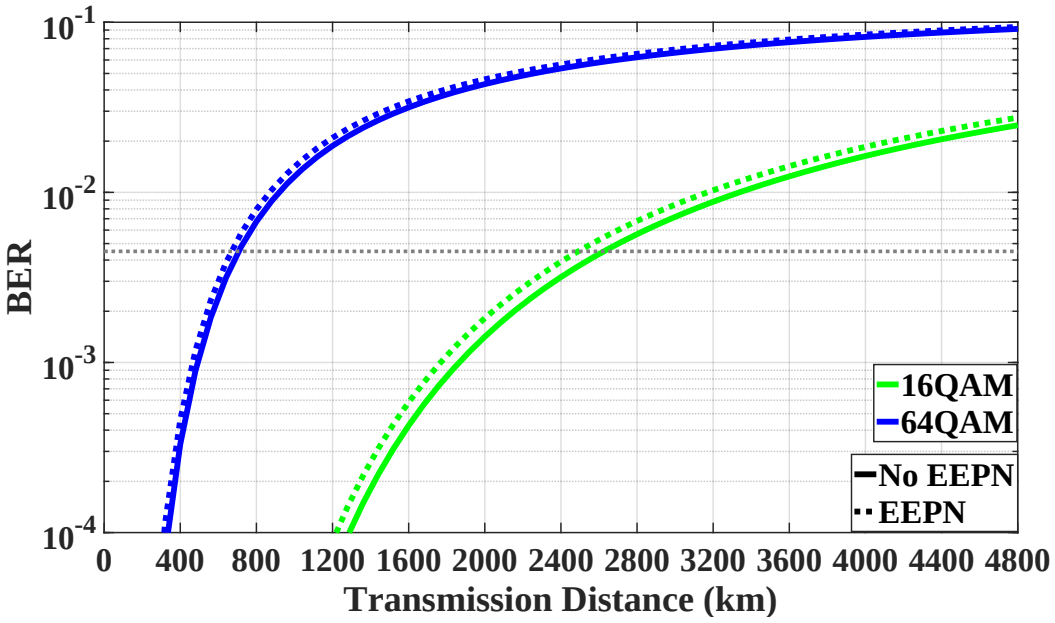

(a)

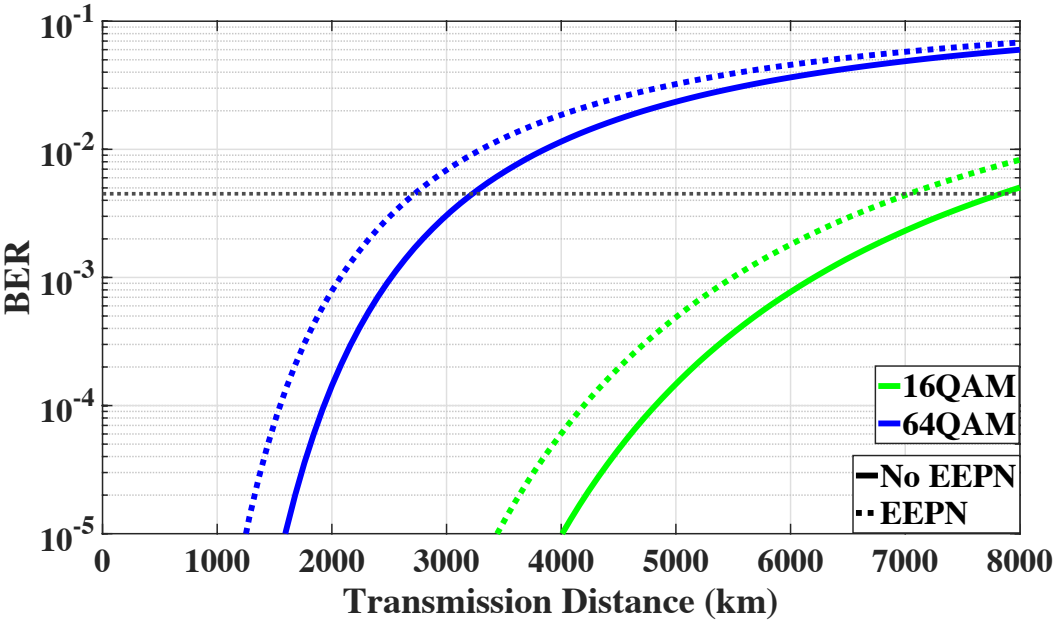

(b)

Figure 4.7: The theoretical BER as a function of transmission distance in the 5-channel Nyquist-spaced system using EDC only (a) and NLC (b), with and without EEPN for the modulation format of 16QAM and 64QAM. The black dotted line indicates the FEC threshold (BER of 4.5×10^{-3}).

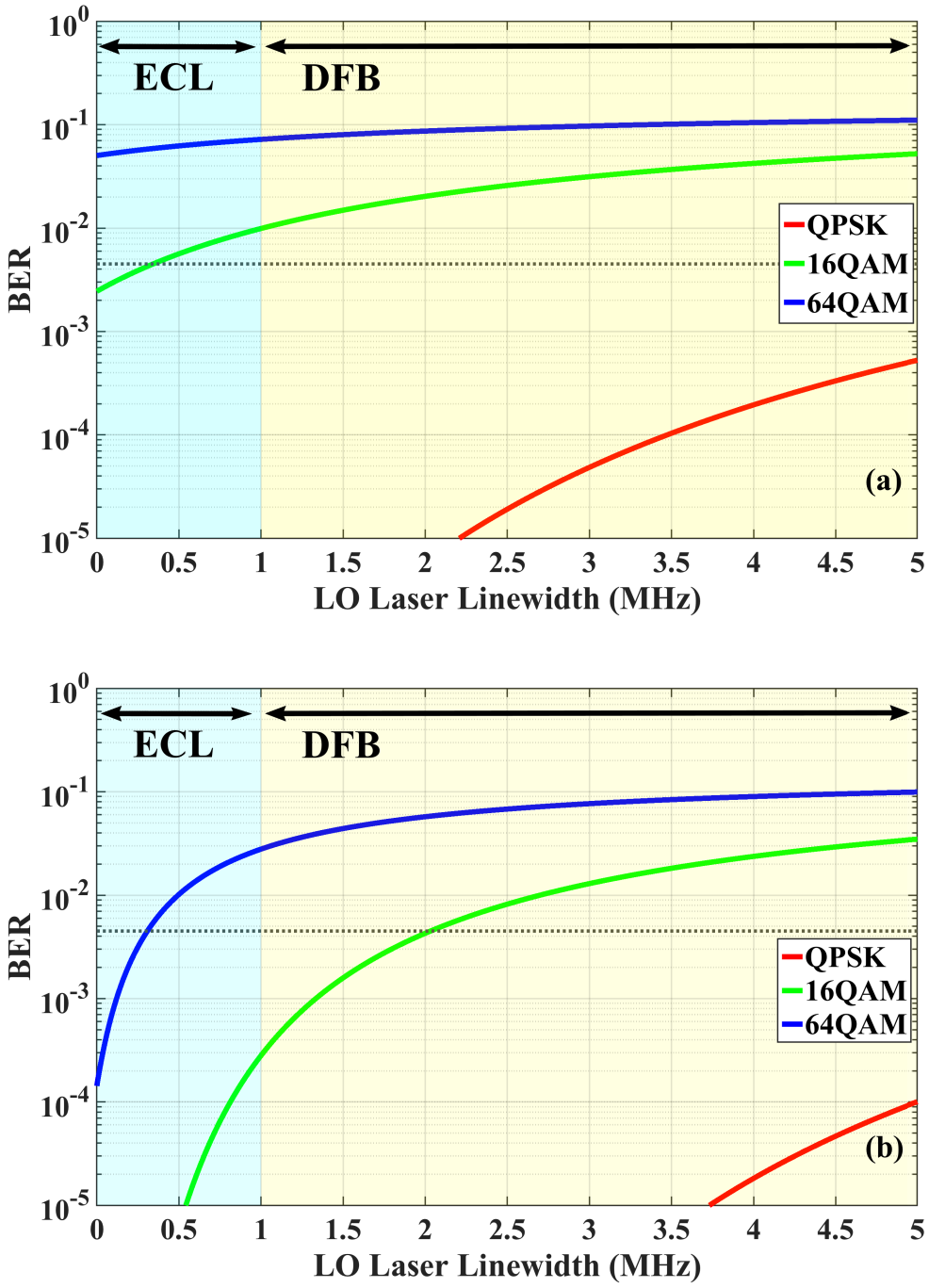

Figure 4.8: The analytical BER as a function of LO laser linewidth in the 2000 km 5-channel Nyquist-spaced system for the modulation format of QPSK, 16QAM, and 64QAM using EDC (a) and NLC (b). The black dotted line indicates the FEC threshold (BER of 4.5×10^{-3}).

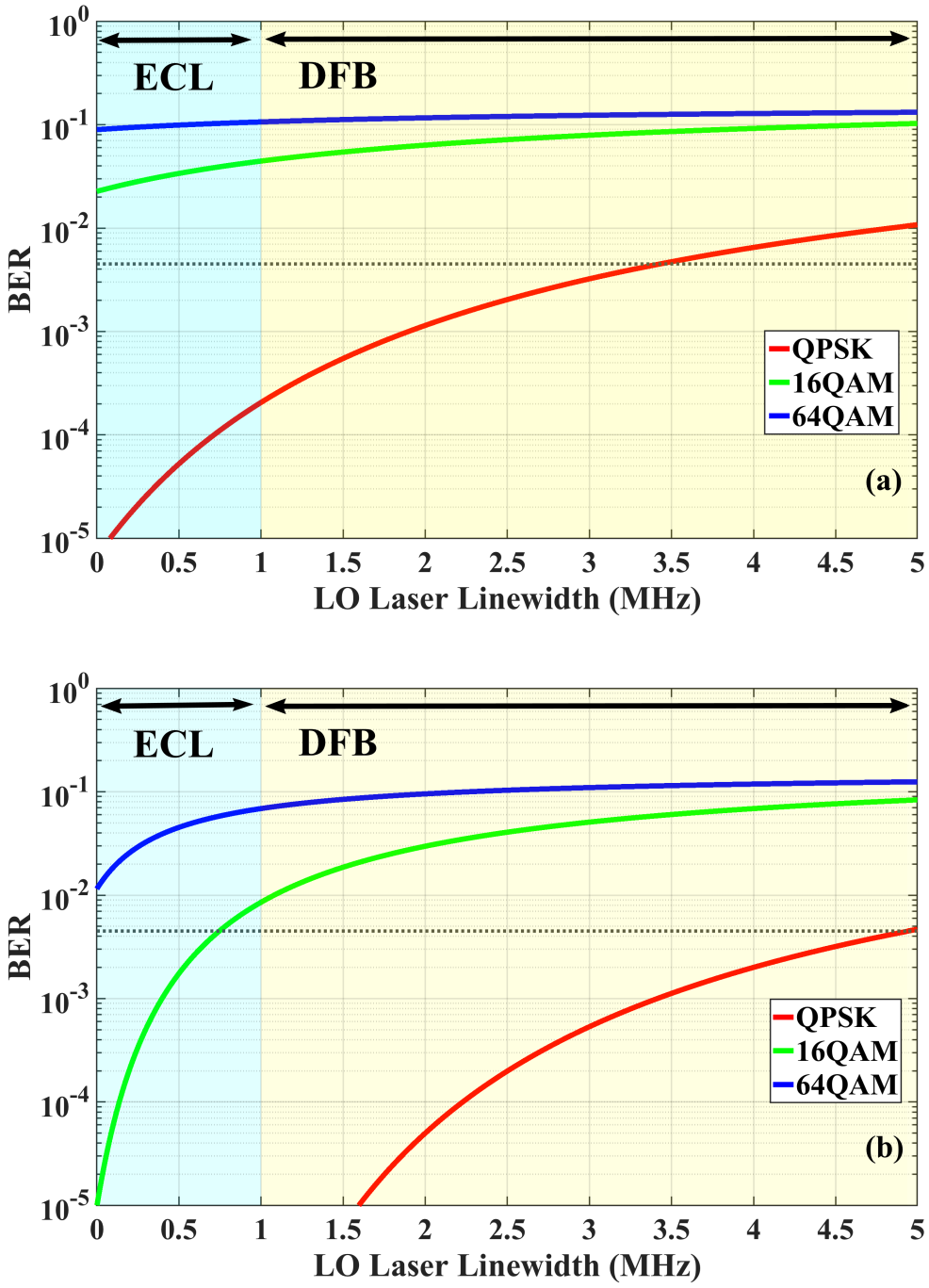

Figure 4.9: The analytical BER as a function of LO laser linewidth in the 4000 km 5-channel Nyquist-spaced system for the modulation format of QPSK, 16QAM, and 64QAM using EDC (a) and NLC (b). The black dotted line indicates the FEC threshold (BER of 4.5×10^{-3}).

formats of 16QAM and 64QAM. Fig. 4.6 (a) and (b) shows the cases of EDC and NLC, respectively. The black dotted line indicates the BER threshold of 4.5×10^{-3}, corresponding to a 7% overhead hard-decision forward-error-correction (FEC) error-free threshold [145], which is applied to evaluate the system performance with a robust transmission margin. The length of each SSMF span is again 80 km. From the results presented in Figure 4.6 (a), it can be inferred that the EEPN effect has a negligible impact on the performance of the EDC system. However, in the case of the NLC system, the effect of EEPN is more pronounced. Specifically, for the 64QAM system, the maximum reach is reduced by 720km (from 4000km to 3280km) due to EEPN. On the other hand, the BER of the 16QAM system remains below the FEC threshold, with or without the EEPN effect, within the considered transmission distance of 0 to 8000km. Regarding the QPSK system, its results are not shown for both EDC and NLC cases since it can support transmission over 8000 km even with the distortion caused by EEPN.

Fig. 4.7 shows the achievable BER as a function of transmission distance in the 5-channel Nyquist-spaced system, with and without EEPN (LO laser linewidth of 100 kHz and 0 Hz, respectively) for the modulation formats of 16QAM and 64QAM. From Fig. 4.7 (a), it is observed that the EEPN effect has a limited impact on the performance of the EDC case. While for the NLC employed system, it is shown from Fig. 4.7 (b) that the maximum transmission distance for the 16QAM system considering EEPN is 6960 km, which is 800 km less than that of the system without EEPN. Similarly, the EEPN reduced the maximum reach by 480 km for the 64QAM system (from 3200 km to 2720 km). The QPSK result is not presented here for both EDC and NLC cases, since it can support transmission over 8000 km under the FEC threshold, even with

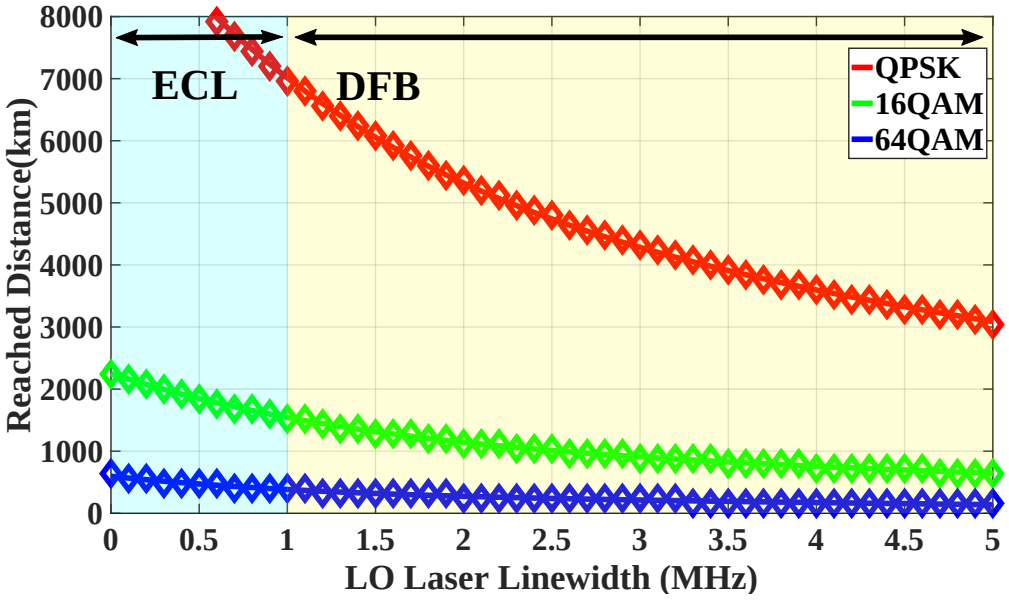

(a)

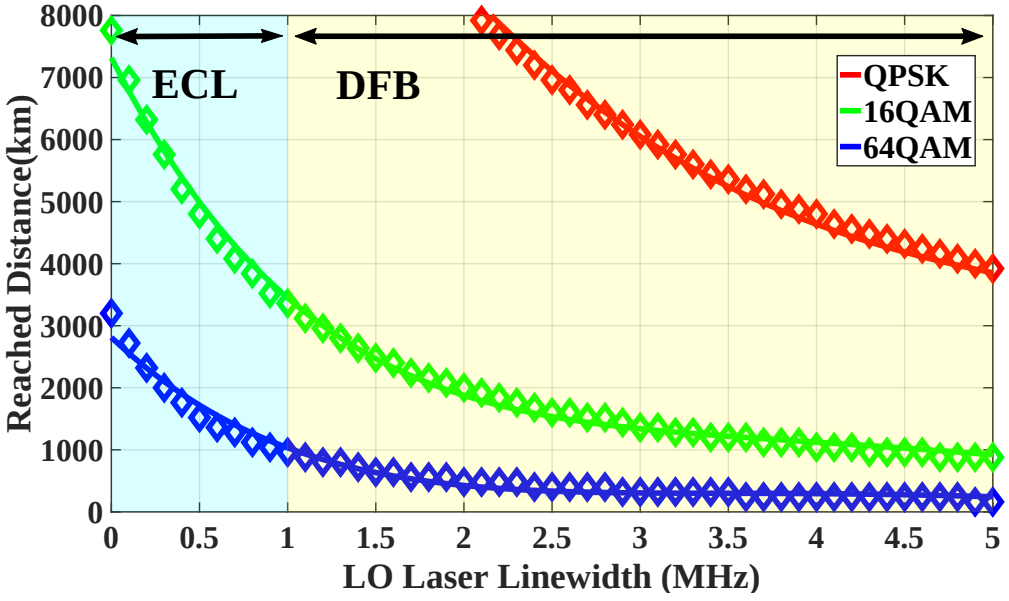

(b)

Figure 4.10: The achievable transmission distance as a function of LO laser linewidth in the 5-channel Nyquist-spaced system using EDC (a) and NLC (b) for the modulation format of QPSK, 16QAM, and 64QAM under the FEC threshold (BER of 4.5×10^{-3}). The 5th-order polynomial fit was applied.

the distortion from EEPN.

Fig. 4.8 shows the theoretical BER as a function of LO laser linewidth

in the 5-channel Nyquist-spaced system for the modulation format of QPSK, 16QAM, and 64QAM with a transmission distance of 2000 km. The black dotted line again indicates the BER threshold of 4.5×10^{-3}. Linewidths of typical lasers used in optical fibre communication systems, such as external cavity lasers (ECLs), and distributed feedback (DFB) lasers, were considered [146]. EDC was employed for Fig. 4.8(a) and NLC was employed for Fig. 4.8(b). For the case of EDC, a 2000 km transmission cannot be ensured for the modulation format of 64QAM even without LPN. When LO laser linewidth is less than 0.342 MHz, the BER value of the 16QAM case is less than the FEC threshold. For the case of NLC, it can be seen from Fig. 4.8(b) that in order to ensure the transmission over a 2000 km fibre link, the LO laser linewidths in 16QAM and 64QAM systems need to be smaller than 2.032 MHz and 0.308 MHz, respectively. The BER of QPSK is well below the FEC threshold for any LO laser linewidth of from 0 to 5 MHz for both EDC and NLC cases.

Fig. 4.9 shows the theoretical BER as a function of LO laser linewidth in the 5-channel Nyquist-spaced system for the modulation format of QPSK, 16QAM, and 64QAM with the transmission distance of 4000 km. EDC was employed for Fig. 4.9(a) and NLC was employed for Fig. 4.9(b). From Fig. 4.9(a), it can be found that DP-16QAM and DP-64QAM systems using only EDC cannot meet the requirement of FEC even without the influence of EEPN at 4000 km. For the transmission of QPSK signals, the maximum allowable LO laser linewidth is 3.429 MHz for the EDC-employed system. From Fig. 4.9(b), it can be observed that below the FEC threshold, the maximum allowable LO laser linewidth in 16QAM and QPSK systems using NLC with a transmission distance of 4000 km are 0.746 MHz and 4.944 MHz. The DP-64QAM NLC-applied system, even without the impact of EEPN, cannot meet the re-

quirement of FEC at such a long distance.

It is found that as the distance increases, the maximum LO linewidth of the system has to be decreased. This can also be observed in Fig. 4.10, which specifically shows the relationship between the maximum reach (under the 7% FEC threshold) and the LO linewidth. Fig. 4.10 (a) and (b) show the EDC and NLC cases, respectively. The results are presented by markers and these lines are fitted by a 5th-order polynomial. According to the data presented in Figure 4.10 (a), it can be observed that the reachable distance shows a gradual decrease as the EEPN effect increases for 16QAM and 64QAM signals. However, for QPSK signals, the decrease is much more significant and occurs rapidly. If the linewidth of the LO laser is less than 2.5 MHz, a 16QAM system can achieve a maximum reach of over 1000 km. Meanwhile, a QPSK system with an LO linewidth below 1 MHz can transmit over 7000km, and even with an LO linewidth of 5MHz, it can still cover a distance of approximately 3000 km. For the NLC case, it can be observed from Fig. 4.10 (b) that, when the LO linewidth is below 1 MHz, the maximum reach of 16QAM systems exceeds 3000 km, and 64QAM systems can transmit over 1000 km. When the LO linewidth is less than 2 MHz, the maximum reaches of 16QAM and 64QAM systems decrease dramatically. It tends to be stable when the LO linewidth is above 2 MHz. The QPSK systems with a LO linewidth of below 2 MHz can reach over 8000 km, and they can still transmit around 4000 km with a LO linewidth of 5 MHz.

4.5 Impact of Transceiver Noise

The aforementioned analyses did not account for the impact of TRx noise, which includes all noise contributions from both the Tx and Rx, such as the

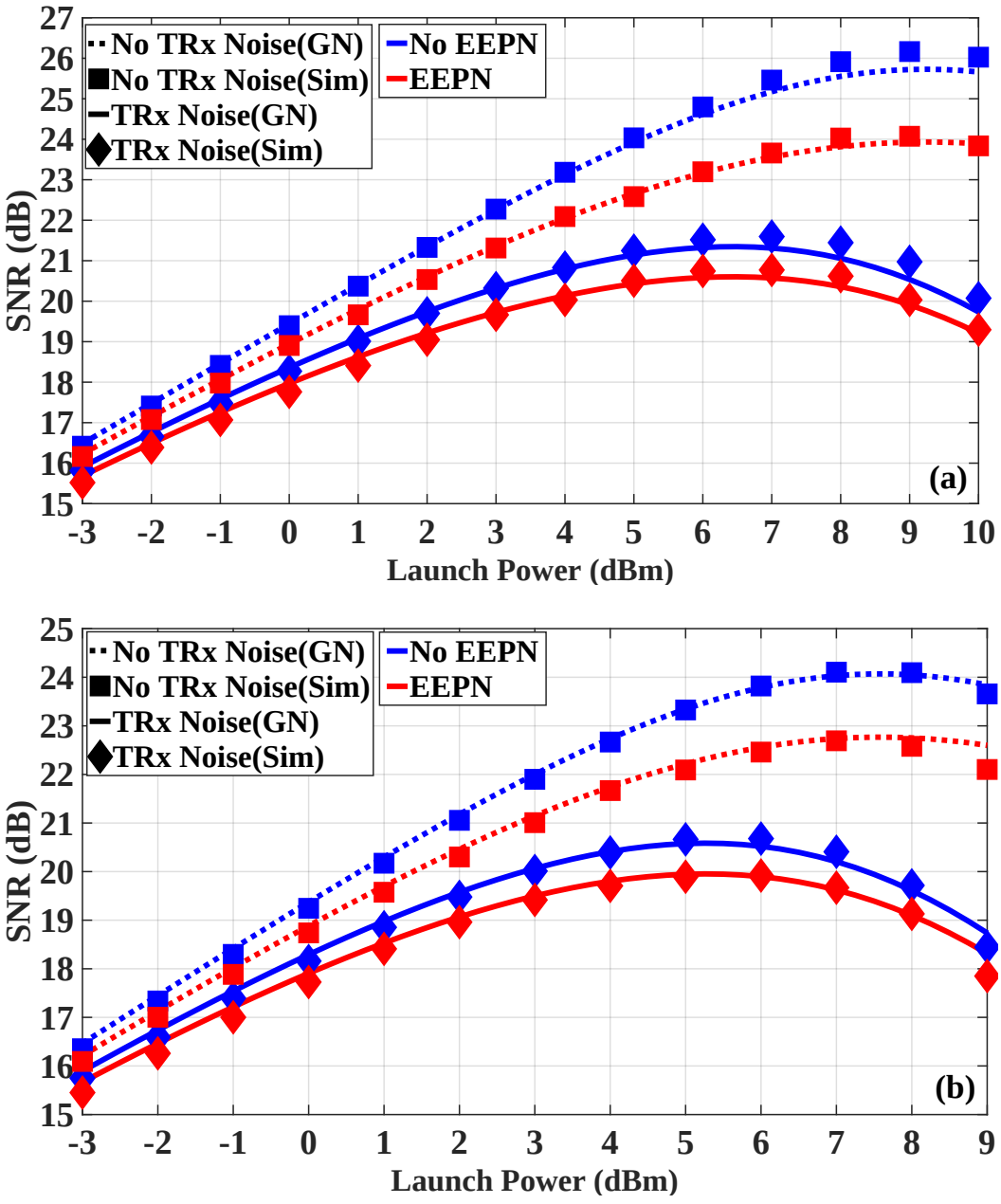

Figure 4.11: The SNR of the central channel as a function of launch power per channel in the single-channel (a) and 5-channel (b) DP-16QAM Nyquist-spaced 2000-km NLC-applied system with and without the impact of 25-dB TRx noise.

finite resolution of DACs and ADCs, the noise from the linear electrical amplifiers, and the noise from some optical components [34]. It defines the maximum achievable SNR in a transmission system. In order to further assess the impact of the EEPN in practical systems, numerical simulations considering TRx noise have been conducted in a 2000 km DP-16QAM Nyquist-spaced system with applying NLC. Similar to Eq. (4.5), and based on Eq. (2.79), the SNR estimated for the case of FF-NLC considering the TRx noise can be expressed as

$$\mathrm{SNR}_{\mathrm{NLC}}^{\mathrm{TRx}} = \frac{P}{P_{\mathrm{ASE}} + P_{\text{s-ASE}} + \sigma_{\mathrm{EEPN}}^2 \cdot P + P_{\text{s-EEPN}} + P_{\mathrm{TRx}} + P_{\text{s-TRx}}}, \tag{4.15}$$

where P_{TRx} and $P_{\text{s-TRx}}$ represent the noise power owing to the TRx noise and its interaction with the signal, respectively. The calculation expressions of P_{TRx} and $P_{\text{s-TRx}}$ can be found in Section 2.5.5. The TRx SNR limit was set to 25 dB in the simulation here with an equal split of TRx noise between the Tx and Rx, where $\kappa_{\mathrm{R}} = 1/2$. This is a typical value for practical superchannel systems [33]. The transmission system has been presented in Section 4.2. Detailed settings were the same as those in Table 4.2.

Fig. 4.11(a) and Fig. 4.11(b) show the results for the single- and 5-channel DP-16QAM NLC-applied transmission systems, both with and without the impact of 25-dB TRx noise. Significant degradation of system performance caused by TRx noise can be observed. For the systems affected by TRx noise, excellent agreement between analytical predictions and simulation results was attained. The gaps between the SNR with and without EEPN are also very significant. EEPN caused reductions in the SNRs, ~ 0.83 dB in

the single-channel system and ~ 0.76 dB in the 5-channel system. Simulation results demonstrate that the system performance degradation due to EEPN is still significant under the influence of TRx noise. Therefore, when evaluating the performance of optical communication systems with LPN, it is necessary to account for the impact of the EEPN effect.

4.6 Impact of Polarisation Mode Dispersion

The PMD effect was neglected in previous simulations. In order to further assess the impact of the EEPN in practical systems, numerical simulations considering PMD have also been conducted in a 2000 km 5-channel DP-16QAM Nyquist-spaced system with applying NLC and EDC. The signal propagation was simulated by solving the Manakov-PMD equation [102]. The PMD param-

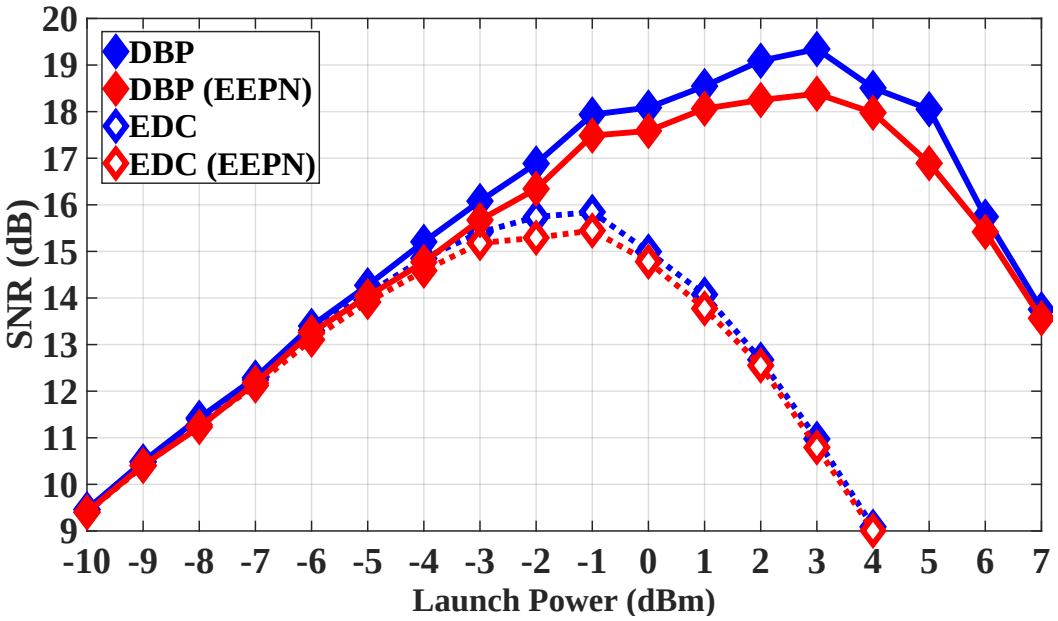

Figure 4.12: The average SNR of the central channel as a function of launch power per channel in the 5-channel DP-16QAM Nyquist-spaced system in the presence of PMD. The transmission distance is fixed at 2000 km.

eter in the system was set as 0.1 ps/$\sqrt{\text{km}}$. The simulation setup was similar to that described in Fig. 4.2. For mitigating the PMD effect, a blind multiple modulus algorithm (MMA) equalizer [147] was additionally applied after the matched filter. Other simulation details of the transmission setup were the same as those listed in Table 4.2.

Simulation results are shown in Fig. 4.12. Despite that in the presence of PMD the performance of EDC case degrades marginally [148,149], and NLC performance degrades considerably, the gaps between the SNRs with and without EEPN remain significant. EEPN caused the SNR reductions of ~ 1 dB in the case of NLC, and ~ 0.45 dB in the case of EDC. Simulation results indicate that the system performance degradation due to EEPN remains substantial even in the presence of the PMD effect.

4.7 Model Application in High-Speed Wideband Systems

This section investigates the performance of WDM Nyquist-spaced nonlinear coherent optical fibre systems via the analytical and simulated results considering various transmission rates, modulation formats and distances. The prediction for $C-$band systems based on the analytical model has also been made.

Fig. 4.13 illustrates the results obtained for a 64-GHz DP-16QAM 5-channel 2000 km Nyquist-spaced transmission system performance. Detailed transmission parameters used for prediction are shown in Table 4.2. Solid lines represent the analytical model predictions, whereas the markers are numerical

simulation outputs. Excellent agreement between the simulation results and the analytical model estimation has also been achieved. It is shown that due to the EEPN effect, the decrease of SNR at the optimal power (about 10 dBm per channel) is observed to be from 23.7 dB to 21.4 dB. This SNR decrement is larger compared to that in the 32-GHz 5-channel transmission system as shown in Fig. 4.4 (a), since the strength of EEPN effect is proportional to the transmission symbol rates. This clearly indicates the role and importance of the EEPN effect in particular for modern high-speed optical communication systems.

Additionally, the LPN tolerance for high-speed long-haul nonlinear optical coherent transmission was also examined. Analytically estimated SNR

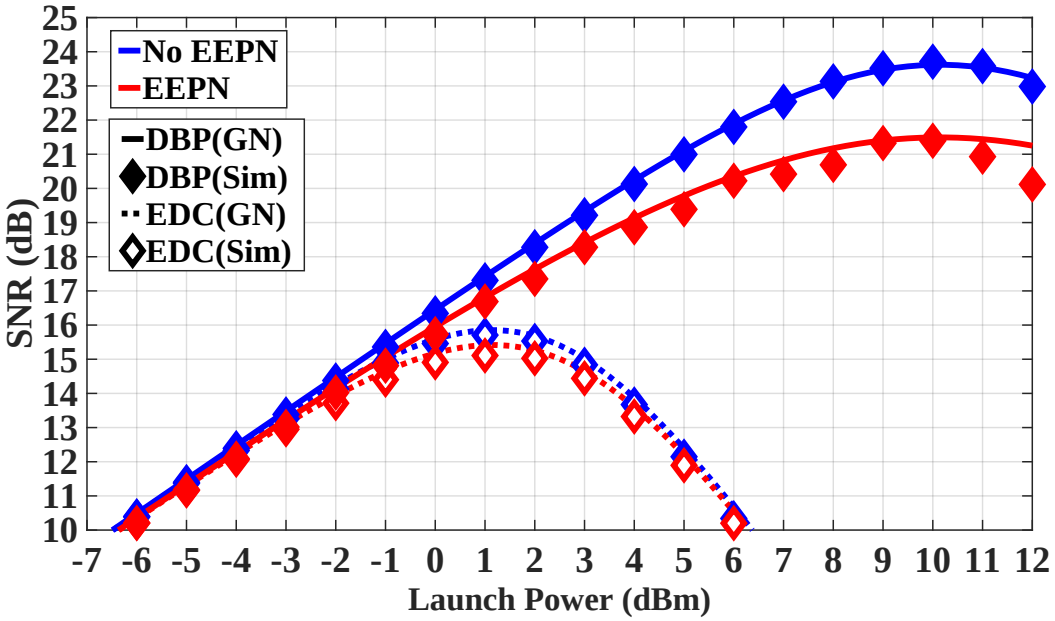

Figure 4.13: The SNR of the central channel as a function of launch power per channel in the 5-channel 64-GHz DP-16QAM Nyquist-spaced system. The transmission distance is fixed at 2000 km. Lines represent the models, and markers represent simulation results.

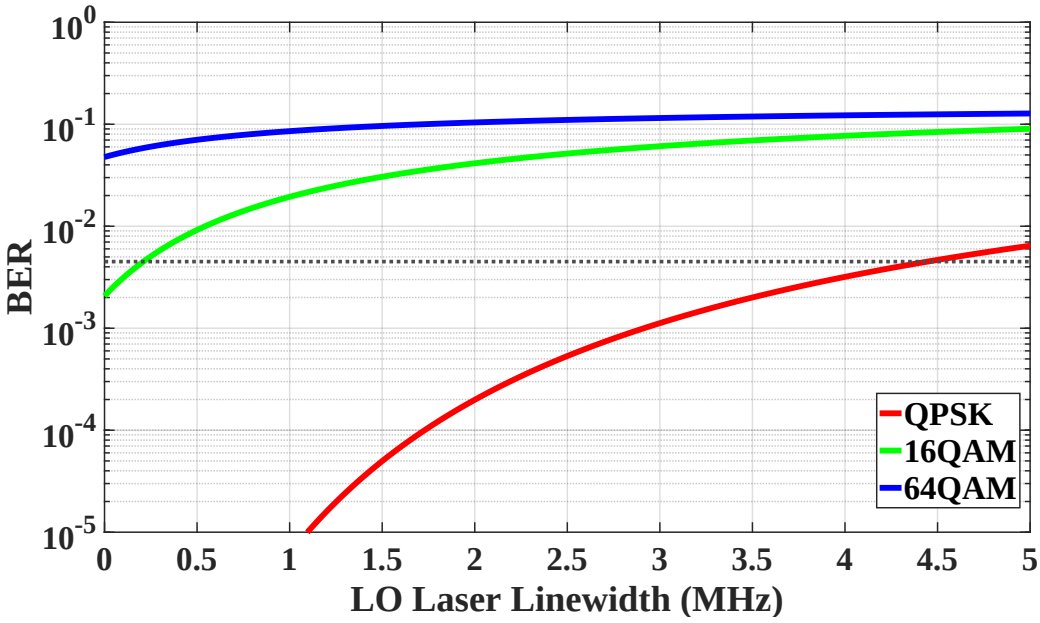

(a)

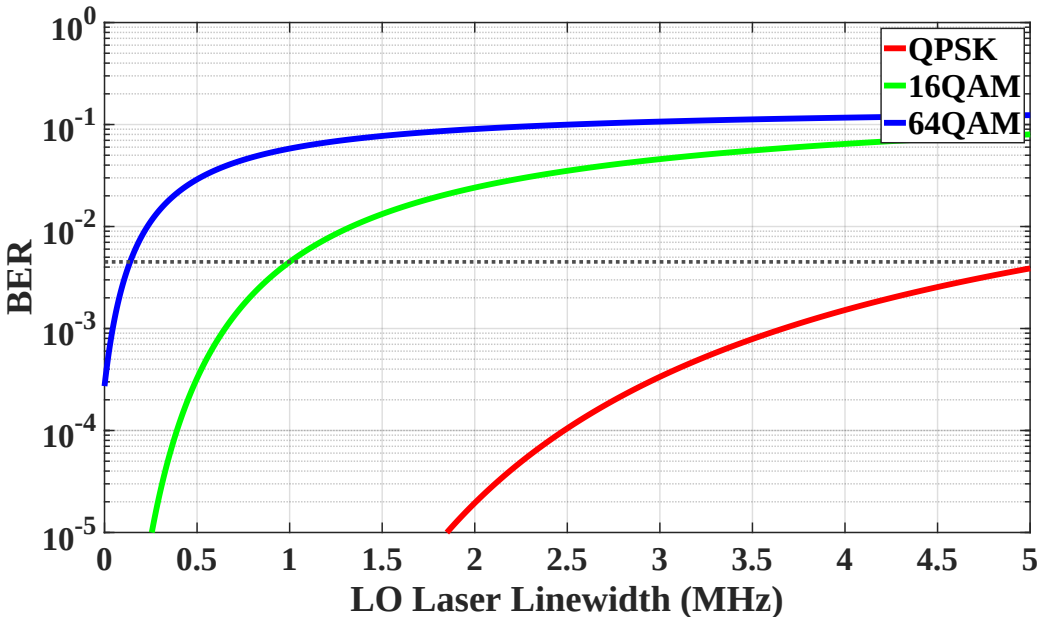

(b)

Figure 4.14: The analytical BER as a function of LO laser linewidth in the 64-GHz 5-channel 2000-km Nyquist-spaced system using EDC (a) and NLC (b) for the modulation formats of QPSK, 16QAM, and 64QAM.

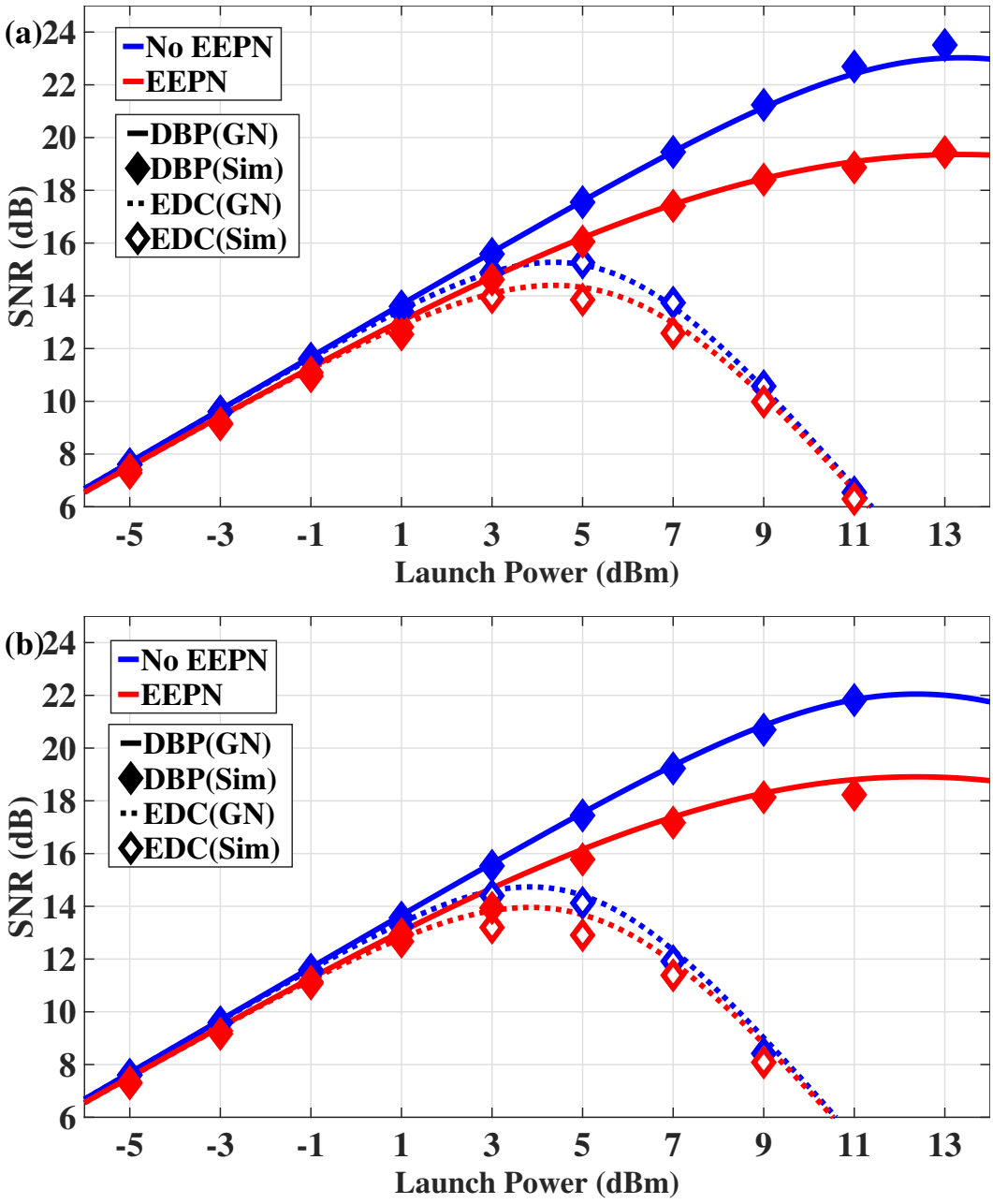

Figure 4.15: The SNR of the central channel as a function of launch power per channel in the single-channel (a) and 5-channel (b) 128-GHz DP-16QAM Nyquist-spaced system. The transmission distance is fixed at 2400 km. Lines represent the models, and markers represent simulation results.

values are converted to BERs. Fig. 4.14 (a) and (b) show the analytical BER as a function of LO laser linewidth in the 64-GHz 5-channel Nyquist-spaced 2000-

km system with the employed EDC and NLC, respectively. QPSK, 16QAM, and 64QAM modulation formats are considered. The dotted line represents the BER threshold. In order to ensure the quality of received symbols, some requirements on the LO laser linewidth were theoretically explicated. In particular, the LO laser linewidths for the DP-16QAM and DP-QPSK systems with EDC are limited to 0.21 MHz and 4.45 MHz, respectively. However, the 64QAM system with EDC is unable to meet the transmission requirement, even without the distortion caused by the EEPN effect. The LO laser linewidths are upper-bounded by 1.00 MHz and 0.14 MHz for the DP-16QAM and DP-64QAM systems using NLC, respectively. However, within the LO laser linewidths frequency range from 0 to 5 MHz, all values of BER in the QPSK systems using NLC remain below the FEC threshold.

Fig. 4.15 (a) shows the central channel performance as a function of launch power per channel in the 128-GHz DP-16QAM single-channel 2400 km (30×80 km) Nyquist-spaced nonlinear optical transmission system. High consistency can be observed between the simulated SNRs and the predictions. It is found from the results that the systems excluding EEPN effects can achieve over 4 dB higher SNRs than the transmission influenced by the EEPN in the case of NLC. The apparent discreteness reveals the vital break in transmissions originated from the EEPN, especially when the communication date rate is at a relatively high level. A similar phenomenon could also be observed in Fig. 4.15 (b), which presents the simulation and theoretical results of the 128-GHz DP-16QAM 5-channel 2400-km Nyquist-spaced nonlinear optical transmission system. The accuracy of the model and the great performance decrease induced by EEPN are demonstrated again in the multi-channel system.

Fig. 4.16 shows the central channel SNR with varying launch power in

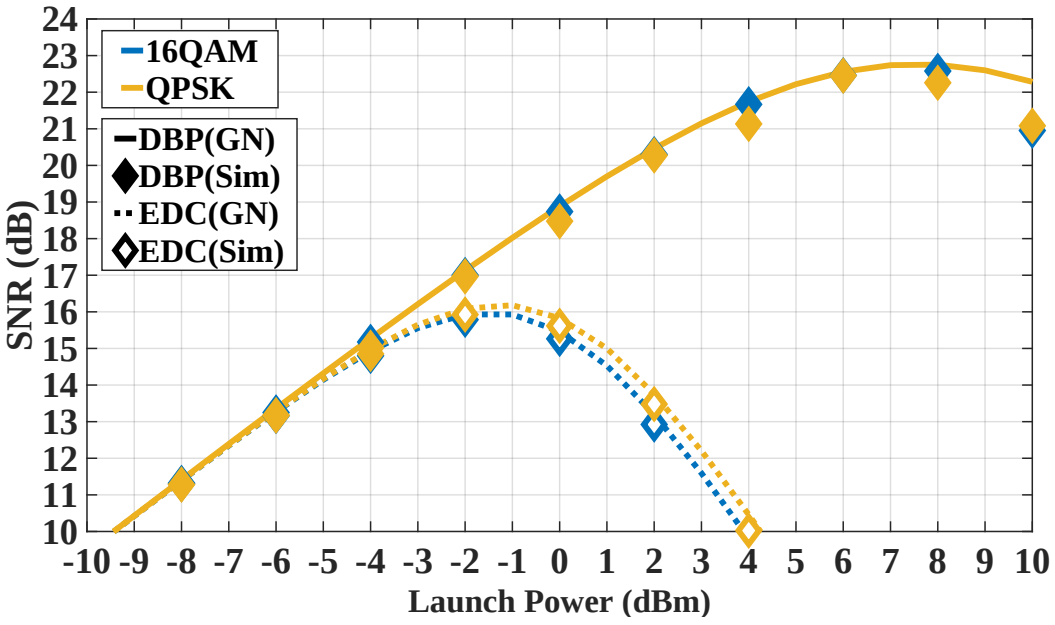

(a)

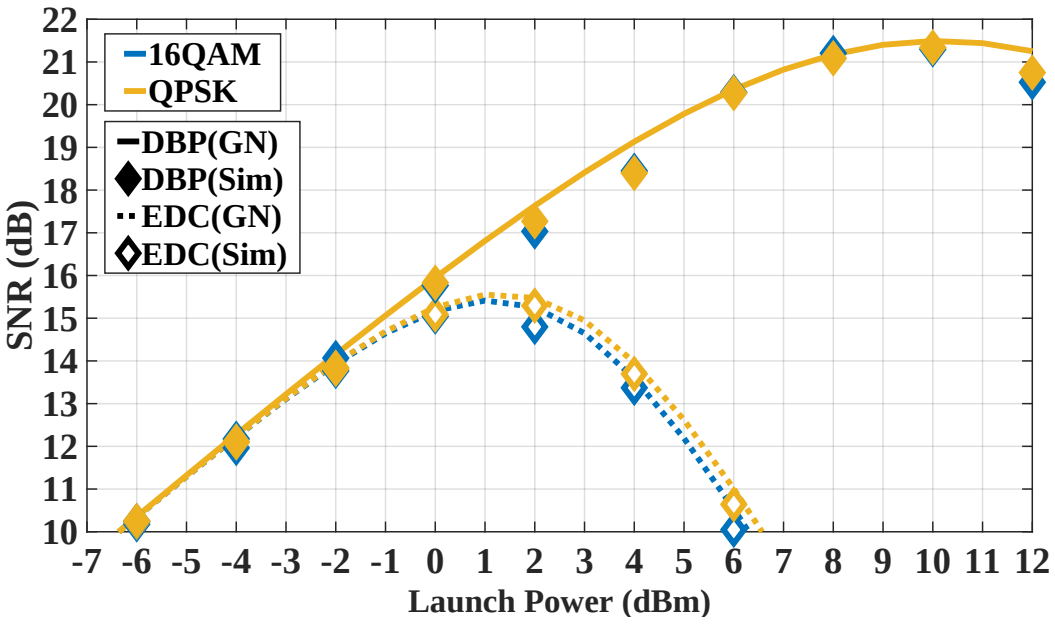

(b)

Figure 4.16: The SNR with varying launch power in Nyquist-spaced 5-channel systems with transmission symbol rates of 32-GBd in (a), and of 64-GBd in (b).

a Nyquist-spaced 25×80 km $5-$channel system with 32-GBd transmission symbol rate in (a), with 64-GBd transmission rate in (b), where significant LO LPN with 100 kHz linewidth is considered. The dotted line represents the result of EDC model Eq. (4.4), and the solid line represents the results of NLC model Eq. (4.5). Both of DP-QPSK and DP-16QAM modulation formats are considered. A great consistency between the results of the analytical model and simulation is observed in Fig. 4.16 (a) and (b), which validates the efficiency and the accuracy of the model described in Section 4.1 in 32-GBd and 64-GBd DP-QPSK and DP-16QAM multichannel Nyquist-spaced nonlinear fibre transmission in cases of NLC and EDC. It is also be observed that the QPSK systems can achieve better performance than 16QAM in the case of EDC. This is because the value of Eq. (2.70) for 16QAM is larger, which indicates a worse NLI distortion, since the value of χ in Eq. (2.71) for 16QAM is smaller compared with that for QPSK. Accordingly, based on the analytical model, the 16QAM system will outperform the 32QAM system, and the 32QAM system will outperform the 64QAM scheme. For DBP scenarios, the performance discrepancy of systems with different modulation formats is negligible due to the strong efficiency of DBP in the NLI mitigation. Comparing the NLC results in Fig. 4.16 (a) and (b), it can also be found that the 32-GBd system performs better than the 64-GBd system, which indicates that the distortion from EEPN and ASE noise scales with the transmission symbol rate as in Eq. (2.47) and Eq. (2.24).

Next, the modulated bandwidth has been extended to 4.5 THz to discuss the performance of an entire $C-$band system with different values of transmission symbol rates. The performance of 16-GBd 281-channel, 32-GBd 141-channel, 64-GBd 71-channel, and 128-GBd 35-channel DP-16QAM

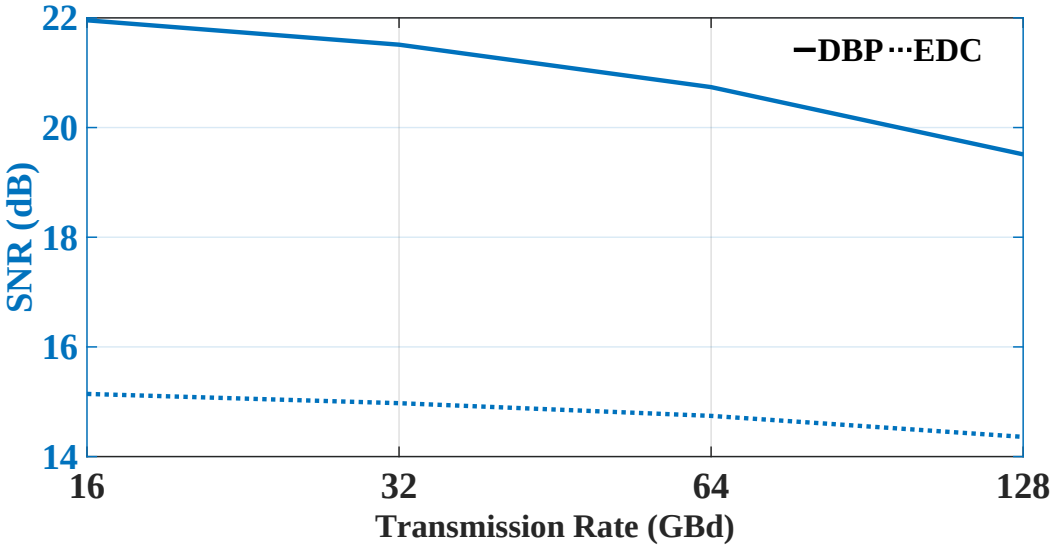

Figure 4.17: The central-channel SNR values in Nyquist-spaced WDM DP-16QAM nonlinear coherent fibre systems with transmission rates of 16, 32, 64 and 128 GBd, where transmission bandwidth is fixed at 4.5 THz.

Nyquist-spaced systems at their optimum powers is discussed as shown in Fig. 4.17. It is observed that with the increase of the transmission symbol rate and the decrease of the channel number, the performance of the $C-$band Nyquist-spaced nonlinear fibre transmission with 100 kHz linewidth LPN degrades gradually, when the overall transmission bandwidth is fixed at 4.5 THz.

Fig. 4.18 shows the center channel SNR taken at the optimum launch power values calculated by using the analytical model with varying transmission distances in the Nyquist-spaced 5-channel DP-16QAM nonlinear coherent fibre transmission, where transmission rates are 32 and 64 GBd. Fig. 4.19 shows the analytical results in the systems with transmission rates of 16, 32, 64, and 128 GBd (281, 141, 71, and 35 channels, respectively) at their optimum powers, where the transmission bandwidth is fixed at 4.5 THz. From both of Fig. 4.18 and Fig. 4.19, it can be found that the system SNRs decrease

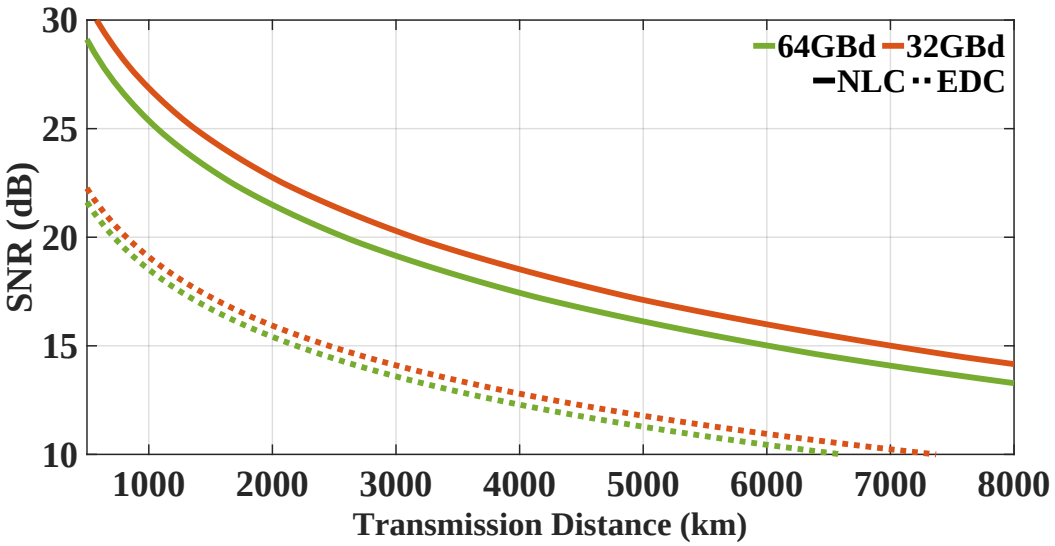

Figure 4.18: The central channel SNR with varying transmission distances in the Nyquist-spaced 5-channel DP-16QAM nonlinear coherent fibre system with symbol rates of 32 and 64 GBd at their optimum powers.

with the growth of transmission distance, and systems with higher transmission rates suffer from heavier distortions. The SNR threshold of $\sim$ 15 dB for 16QAM (the BER threshold of 4.5×10^{-3}). It can be observed from Fig. 4.18 that considering the 15 dB SNR threshold, the 32 GBd 5-channel system can transmit $\sim$ 1000 km further than the 64 GBd 5-channel system in the case of NLC. The SNR values of the system employing EDC are higher than 15 dB when propagation distances are less than 2000 km. It is observed again from Fig. 4.19 that with decreasing channel numbers and increasing symbol rate, the C-band Nyquist-spaced system shows the worse performance. It has also been observed from Fig. 4.19 that for $C-$band systems considering the SNR threshold of 15 dB, the 16 GBd system can reach a transmission distance $\sim$ 440 km longer than the 128-GBd 35-channel system. The SNR values of the $C-$band systems employing EDC are more than 15 dB when distances are

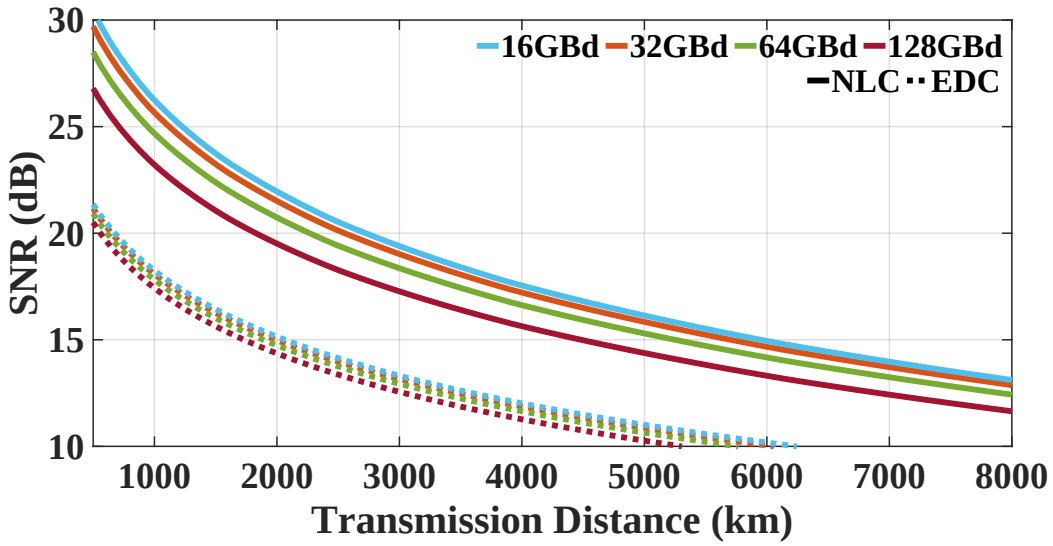

Figure 4.19: The central channel SNR with varying transmission distances in the wideband Nyquist-spaced DP-16QAM nonlinear coherent fibre system with transmission rates of 16, 32, 64, and 128 GBd at their optimum powers, where transmission bandwidth is fixed at 4.5 THz.

less than $\sim$ 1680 km.

4.8 Distributed Raman Amplified Systems Influenced by EEPN

The previous study concentrated on the lumped-EDFA-amplified system, but attention is turn to the impact of EEPN on Nyquist-spaced coherent optical transmission systems amplified by distributed Raman amplification. This section will utilise the analytical model and numerical simulations to examine the system's performance.

Distributed Raman amplification is a popular choice for long-haul transmission systems, owing to its advantages over lumped amplification, such as

lower noise figure and better gain flatness. However, in high-speed transmission systems, EEPN can still have a negative impact on system performance. Therefore, it is critical to assess the impact of EEPN on the system's performance.

The analytical model and numerical simulations were employed to investigate the effects of EEPN on the coherent optical transmission system's performance. The effects of EEPN on the system's parameters such as modulation formats, maximum reach, and error rate were considered.

This study aimed to provide valuable insights into the performance of distributed-Raman-amplified Nyquist-spaced coherent optical transmission systems in the presence of EEPN.

4.8.1 Analytical Model

The GN model considering the EEPN effects for a dispersion-unmanaged system has been given by Eq. (4.3). The contributions of distributed-Raman-amplification ASE noises and the variance of EEPN effects can be calculated by Eq. (2.28) and Eq. (2.47), respectively. The contributions of the signal-signal nonlinear interference and the signal-ASE interaction for backward-pumped distributed-Raman-amplified systems can be expressed by the following equations according to Section 2.5:

$$P_{\text{s-s}} = N^{1+\varepsilon} \eta_{\text{DRA}}\left(1, B\right) \cdot P^3 \,, \tag{4.16}$$

$$P_{\text{s-ASE}} \approx 3\,\xi_1\,\eta_{\text{DRA}}\left(1, B\right) \frac{P_{\text{ASE}}}{N} \cdot P^2 + 9\,\xi_2\,\eta_{\text{DRA}}\left(1, B\right)^2 \frac{P_{\text{ASE}}}{N} \cdot P^4 \,, \tag{4.17}$$

$$\eta_{\mathrm{DRA}}\left(1,B\right)=\frac{16\gamma^{2}}{27\,R^{2}}\int_{-B/2}^{B/2}\int_{-B/2}^{B/2}df_{1}df_{2}\,\left|\,\rho_{\mathrm{DRA}}\left(f,f_{1},f_{2}\,|\,L\right)\right|^{2}\,\mathrm{rect}\left(\frac{f_{1}+f_{2}}{B}\right),\tag{4.18}$$

where the expression of FWM efficiency factor for the backward-pumped DRA system $\rho\left(f,f_{1},f_{2}\,|\,L\right)$ has been given in Eq. (2.64), and $\mathrm{rect}\left(x\right)$ stands for the rectangular function.

4.8.2 Transmission System

To evaluate the impact of EEPN on system performance, numerical simulations were carried out using a 32-GBd DP-16QAM optical transmission system, as depicted in Fig.4.20. The transmitted signal symbol sequence in each channel at the Tx was completely random and independent. Non-return-to-zero pulse shaping with a roll-off of 0.1% was implemented. A recirculating fibre loop was employed in the transmission link, and SSFM with a span length of 80 km was utilised to simulate the signal propagation over the optical fibre, based on the split-step Fourier solution of the Manakov equation [102, 143]. Backward-pumped distributed Raman amplification was applied after each span of fibre using a coupler. At the Rx, coherent detection was performed by mixing the signal with a LO laser. LO laser linewidths of 0 and 100 kHz were considered for the simulations to analyse the impact of EEPN. The signals were detected using photodetectors and sampled by ADCs. At the Rx, a RRC filter was applied in DSP modules before the NLC (or EDC) module, and an FDE was utilised as the EDC module [21]. The Rx-side NLC was performed using the reverse split-step Fourier solution of the Manakov equation [144]. An ideal CPE was implemented to compensate for phase noise, achieved by conjugate

multiplication between the received signal and the extracted intrinsic LPN. An RRC filter with a roll-off factor of 0.1% was utilised as the matched filter to eliminate out-of-band noise. The simulation disregarded laser frequency offset and PMD, and Table 4.2 provides detailed parameters of the transmission system.

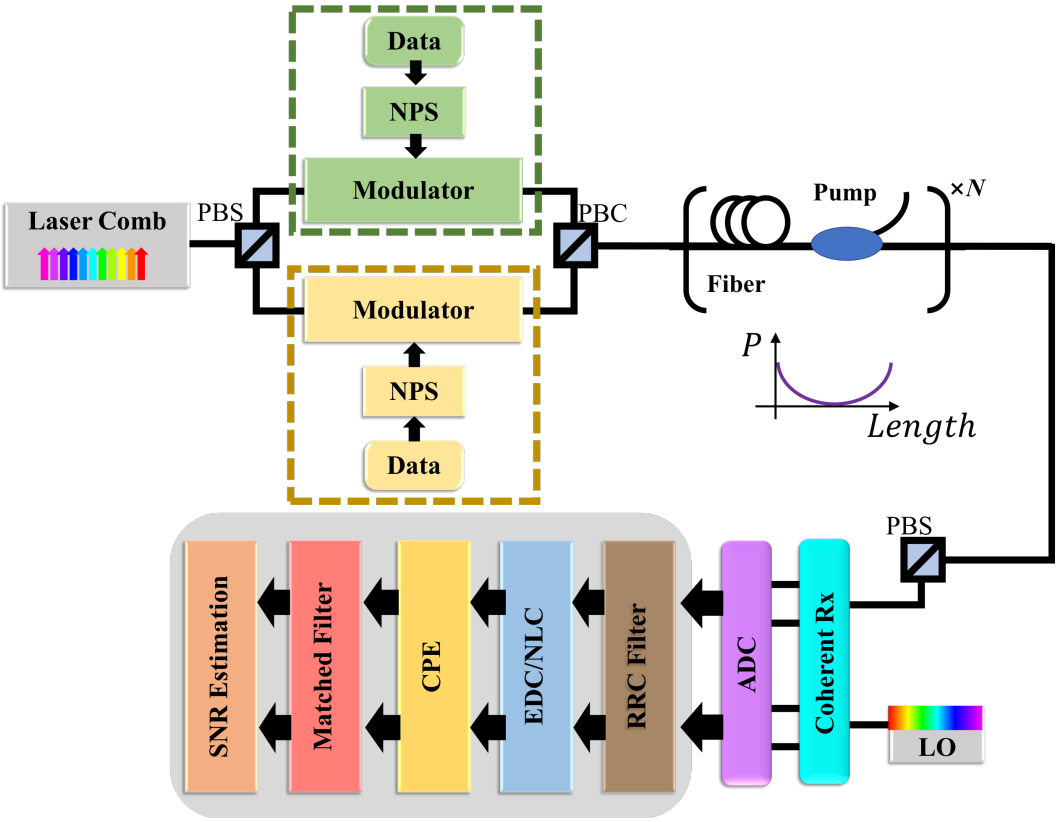

Figure 4.20: Simulation setup of DP-16QAM distributed-Raman-amplified transmission system using EDC or NLC.

4.8.3 Results and Discussion

The investigation was conducted to evaluate the performance of a distributed Raman-amplified single-channel DP-16QAM system over a transmission distance of 2000 km, which corresponds to 25 fibre spans. Both numerical sim-

Table 4.2: System Parameters

Parameters	Values
Attenuation coefficient @ 1550 nm (α_s)	0.2 [dB/km]
Attenuation coefficient @ 1450 nm (α_p)	0.25 [dB/km]
CD coefficient (D)	17 [ps/nm/km]
Nonlinear coefficient (γ).	1.2 [1/W/km]
Total fibre length ($N \times L$)	25×80 [km]
Symbol rate (R)	32 [GBd]
Channel spacing	32 [GHz]
Modulation format	DP-16QAM
Roll-off factor	0.1%
Number of symbols	2^{20}
LO laser linewidth	$\{0, 100\}$ [kHz]

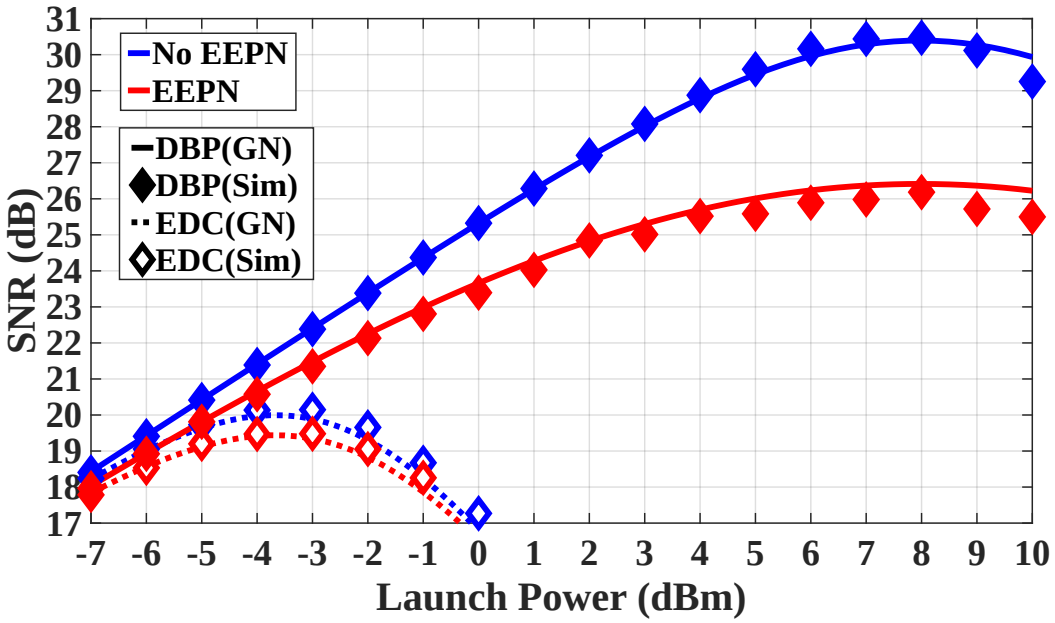

Figure 4.21: The SNR as a function of launch power in the DP-16QAM distributed Raman-amplified system.

ulations and analytical model predictions were utilised to obtain the results presented in Fig. 4.21, which indicate that the simulation outcomes were consistent with the proposed model expression in both EDC and NLC scenarios.

The study also highlighted the significant impact of EEPN on NLC performance. The findings suggest that the variance of EEPN is much smaller than the signal-signal interaction but significantly larger than the signal-ASE interaction for distributed Raman-amplified systems. Moreover, the study revealed that the EEPN effect decreased the SNR of the EDC-employed system by 0.67 dB. For the NLC case, the SNR with EEPN was 4.28 dB lower than that without EEPN at the optimal power of 8 dBm. These results underscore the importance of considering EEPN when designing and optimizing distributed-Raman-amplified systems to achieve optimal performance over long transmission distances.

The single-channel distributed-Raman-amplified system's achievable BER with and without the effect of EEPN (with LO laser linewidth of 100 kHz and 0 Hz, respectively) is presented as a function of transmission distance in Fig. 4.22, where (a) and (b) depict the EDC and NLC cases, respectively. The black dotted line represents the BER threshold of 4.5×10^{-3}, which corresponds to a 7% overhead FEC error-free threshold. Each SSMF span's length is 80 km. From the results presented in Figure 4.22 (a), it can be inferred that the EEPN effect degrades the performance of the EDC system. The maximum reach is reduced by 640 km (from 5840 km to 5200 km) for the 16QAM transmission and by 160 km (from 1600 km to 1440 km) for the 64QAM case due to EEPN. The QPSK system can support transmission over 8000 km even with the distortion caused by the EEPN effect. For the NLC system, the effect of EEPN is more pronounced, with a reduction of 2480 km (from 7840 km to 5360 km) in maximum reach for the 64QAM system. Nevertheless, the BER of the QPSK and 16QAM systems remains below the FEC threshold, regardless of the EEPN effect, within the transmission distance range of 0 to 8000 km.

The theoretical BER as a function of LO laser linewidth in the distributed-Raman-amplified system is shown in Fig.4.23 for QPSK, 16QAM, and 64QAM modulation formats at a transmission distance of 2000km. The black dotted line represents the BER threshold of 4.5×10^{-3}, and typical laser linewidths used in optical fibre communication systems, such as ECLs and DFB lasers, are considered [146]. Fig.4.23 (a) employs EDC, and Fig.4.23 (b) employs NLC. For the EDC case, it is observed that even without LPN, a 2000 km transmission cannot be ensured for the 64QAM modulation format. The BER value of the 16QAM case is less than the FEC threshold only when the LO laser linewidth is less than 1.58 MHz. In the case of NLC, Fig.4.23(b) shows that to ensure transmission over a 2000 km fibre link, the LO laser linewidths in 16QAM and 64QAM systems need to be less than 2.25 MHz and 0.53 MHz, respectively. The BER of QPSK remains well below the FEC threshold for any LO laser linewidth from 0 to 5 MHz for both EDC and NLC cases.

The achievable BER as a function of LO laser linewidth in a distributed-Raman-amplified system for the modulation formats of QPSK, 16QAM, and 64QAM with a transmission distance of 4000 km is presented in Fig.4.24. EDC is used for Fig.4.24(a), while NLC is used for Fig.4.24(b). Fig.4.24(a) reveals that DP-64QAM systems using only EDC cannot meet the FEC requirement at 4000 km even without the influence of EEPN. For the transmission of QPSK signals, the maximum allowable LO laser linewidth is 4.58 MHz for the EDC-employed system. For the 16QAM system, the LO laser linewidth should be less than 0.39 MHz. Fig. 4.24(b) indicates that the maximum allowable LO laser linewidths below the FEC threshold in 16QAM and 64QAM systems using NLC with a transmission distance of 4000 km are 1.06 MHz and 0.20 MHz, respectively. The DP-QPSK NLC-applied system can meet the FEC

requirement at such a long distance within the considered laser linewidths range of 0 to 5 MHz.

In Fig.4.25, the relationship between the LO linewidth and the maximum reach (under the 7% FEC threshold) is presented for both the EDC and NLC cases. Fig.4.25 (a) and (b) correspond to the EDC and NLC cases, respectively. From the data in Fig.4.25 (a), it can be observed that the achievable distance gradually decreases as the EEPN effect increases for 64QAM signals, whereas for QPSK and 16QAM signals, the decrease is much more pronounced and rapid. For a 16QAM system, a maximum reach of over 2000 km can be attained if the LO laser linewidth is less than 1.5 MHz, while a QPSK system with an LO linewidth below 4.5 MHz can transmit over 4000km. In the NLC case, Fig.4.25 (b) indicates that the maximum reach of 16QAM systems exceeds 4000 km, and 64QAM systems can transmit over 1000 km, when the LO linewidth is below 1 MHz. However, when the LO linewidth is less than 2 MHz, the maximum reaches of 16QAM and 64QAM systems decrease dramatically. Lastly, QPSK systems with an LO linewidth below 2.5 MHz can reach over 8000 km.

4.9 Summary

An analytical model accounting for the impact of EEPN has been presented for evaluating the performance of nonlinear Nyquist-spaced optical communication systems. The significance of the EEPN contribution in nonlinear optical transmission systems as well as the accuracy and effectiveness of the analytical approach were validated via split-step Fourier numerical simulations. In the case of NLC, an SNR reduction of 1.41 dB in a 5-channel system due to

EEPN was observed. Furthermore, it remained significant when a practical TRx limit noise and PMD are considered. Simulation results also showed substantial growth of the EEPN impact with increasing the transmission distance.

The performance of wideband Nyquist-spaced long-haul multichannel nonlinear fibre systems influenced by the EEPN effect was also analysed and discussed based on both numerical simulations and analytical models. The performance of C-band systems with different transmission symbol rates was also studied. The results indicate that the SNR of the C-band system using only EDC with 100 kHz linewidth LO LPN remains higher than 15 dB when the transmission distance is less than 1680 km, and that the 16 GBd system with NLC can reach a $\sim$440 km longer transmission distance than the 128 GBd system when considering an SNR threshold of 15 dB.

The impact of EEPN effects on the performance of the backwards-pumped distributed-Raman-amplified nonlinear system has also been investigated via analytical models and numerical simulations. The accuracy of the proposed model has again been validated. The results indicate that the EEPN effects can degrade the distributed-Raman-amplified system performance significantly.

This work extends the scope of conventional GN model applications and demonstrates the relevance and importance of including the contribution of the EEPN effect in the design and performance assessment of long-haul high-capacity optical communication systems with considerable laser linewidths for both lumped EDFA amplification and distributed Raman amplification. It also provides insightful discussions for the design of high-speed wideband Nyquist-spaced WDM long-haul nonlinear fibre systems with considerable LPN.

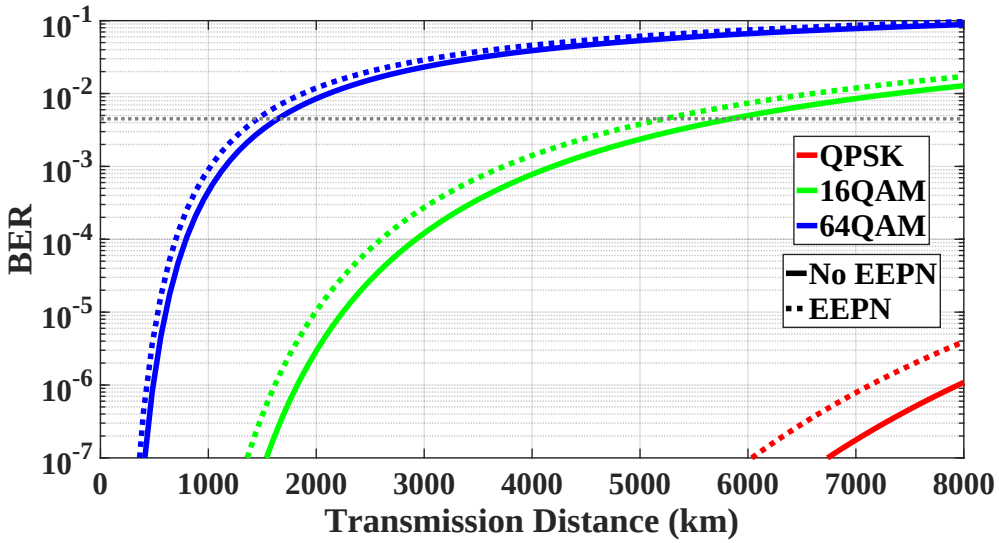

(a)

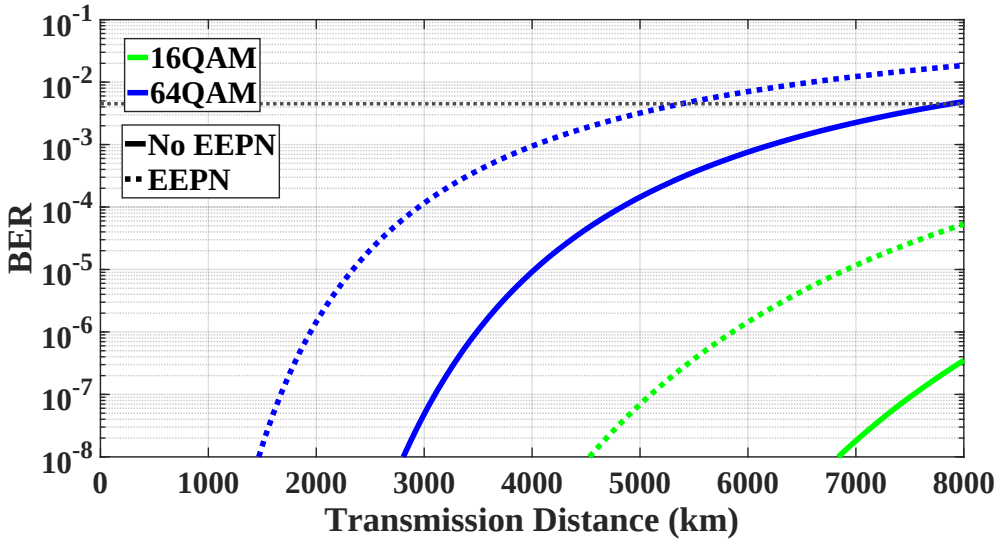

(b)

Figure 4.22: The theoretical BER as a function of transmission distance in the single-channel distributed-Raman-amplified system using EDC only (a) and NLC (b), with and without EEPN for the modulation format of 16QAM and 64QAM. The black dotted line indicates the FEC threshold (BER of 4.5×10^{-3}).

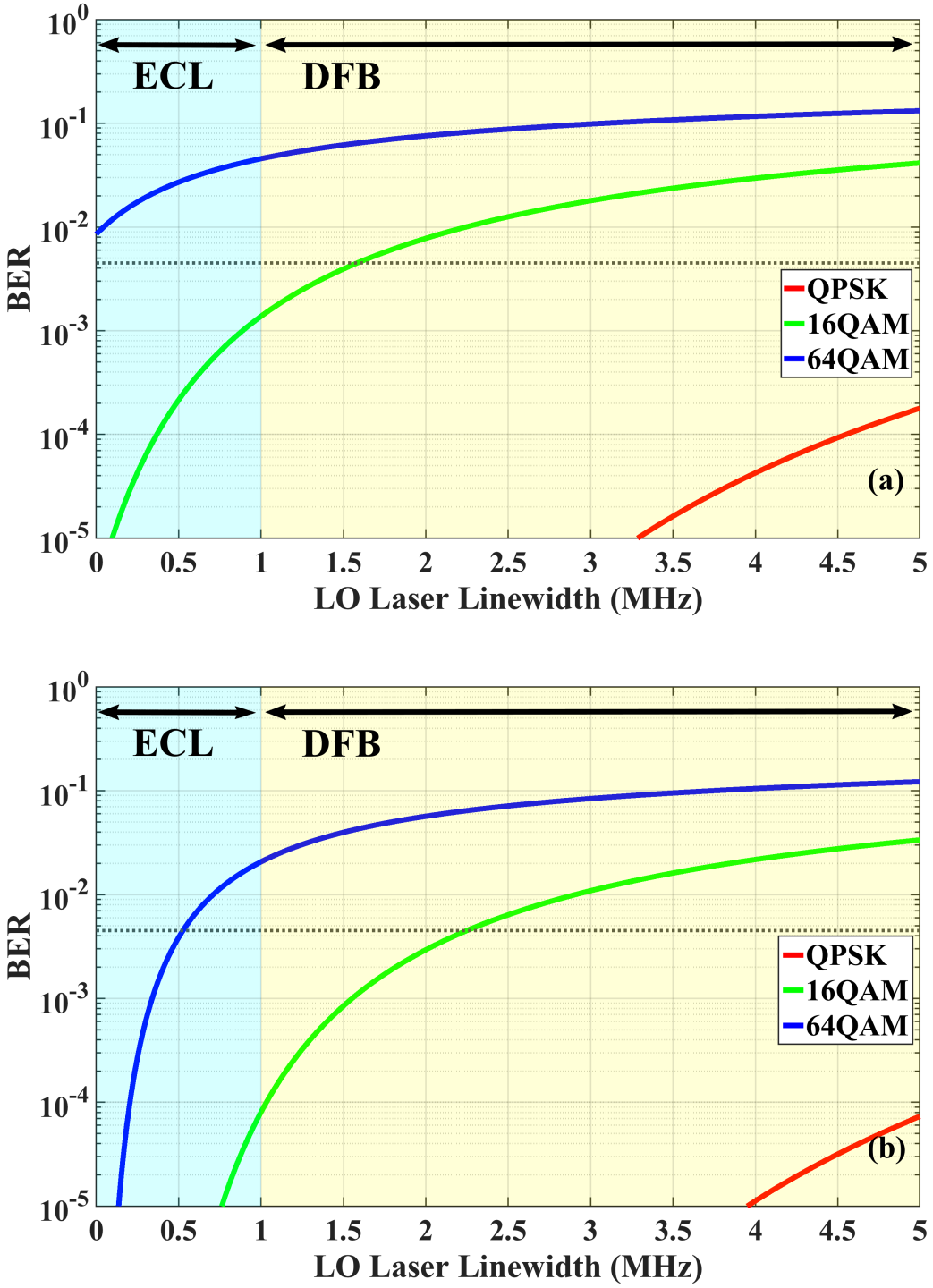

Figure 4.23: The analytical BER as a function of LO laser linewidth in the 2000 km distributed-Raman-amplified nonlinear optical fibre system with the modulation format of QPSK, 16QAM, and 64QAM using EDC (a) and NLC (b). The black dotted line indicates the FEC threshold (BER of 4.5×10^{-3}).

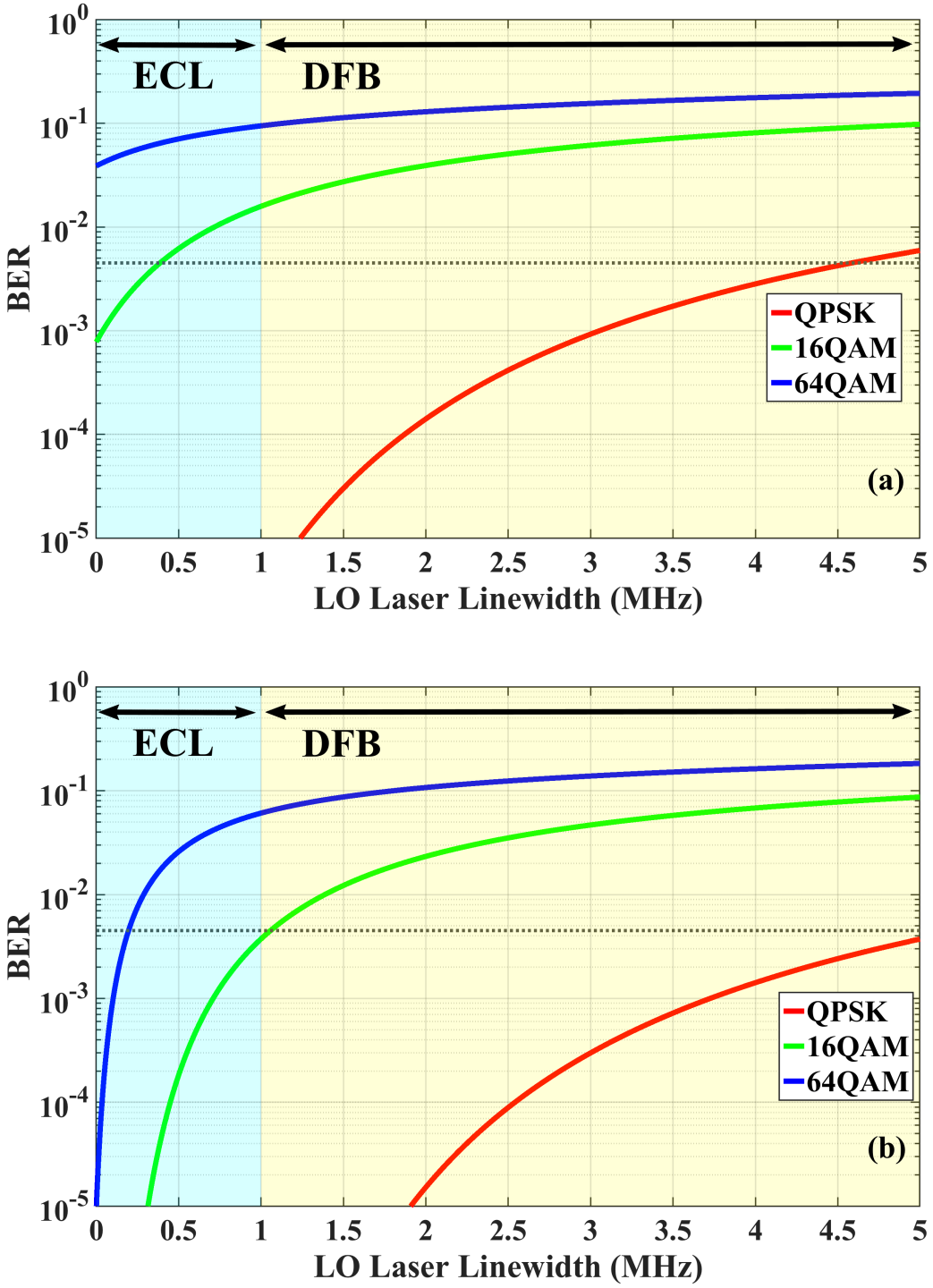

Figure 4.24: The analytical BER as a function of LO laser linewidth in the 4000 km distributed-Raman-amplified nonlinear optical fibre system with the modulation format of QPSK, 16QAM, and 64QAM using EDC (a) and NLC (b). The black dotted line indicates the FEC threshold (BER of 4.5×10^{-3}).

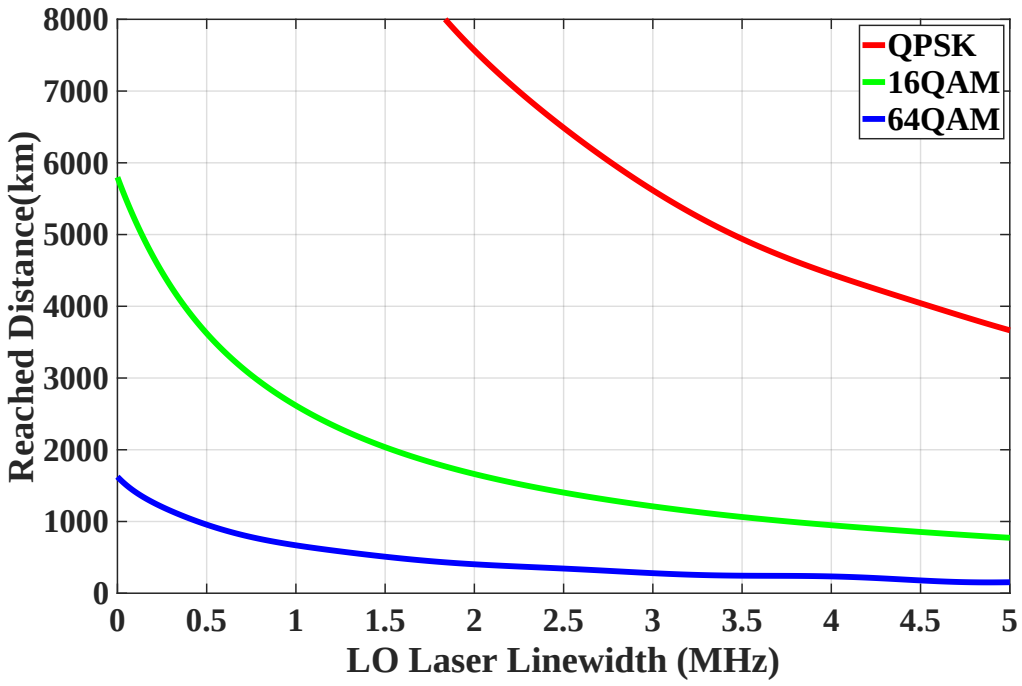

(a)

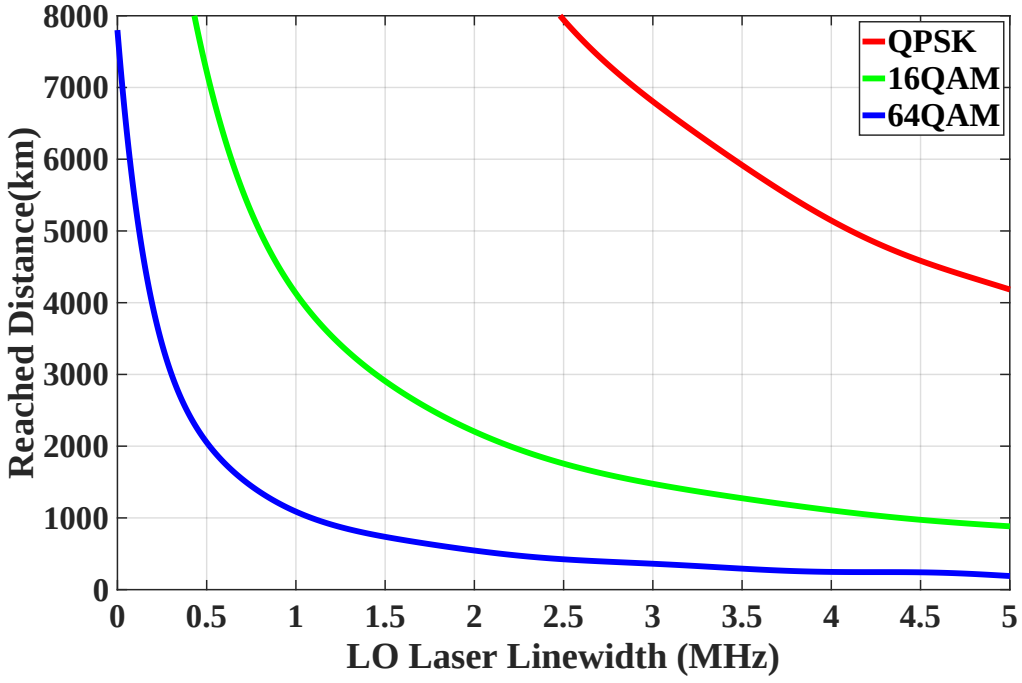

(b)

Figure 4.25: The achievable transmission distance as a function of LO laser linewidth in the distributed-Raman-amplified system using EDC (a) and NLC (b) for the modulation format of QPSK, 16QAM, and 64QAM under the FEC threshold (BER of 4.5×10^{-3}).

Chapter 5

Kalman-Filter-Based Phase Noise Estimation in Long-Haul Nonlinear Optical Communication Systems

In this chapter, a comprehensive investigation of the KF-based estimators has been performed under realistic long-haul optical link conditions, aiming to provide important insight into the application of the KF techniques to guarantee high-quality recovery of received signals during the design of long-haul coherent optical fibre communication systems. The performance of the KF in mitigating distortions from the effect of EEPN, ASE noise, LPN and fibre nonlinearity has been analysed in detail. Numerical simulations have been conducted in both dispersion-unmanaged and dispersion-managed nonlinear long-haul transmission systems. Both DP-QPSK and DP-16QAM are considered. A VV estimator has been implemented as a benchmark. A BPS has also

been employed for comparison in the QPSK systems. The application of the KF on top of an optimal full-field NLC has been explored. Furthermore, the transmission performance with reasonable TRx noise has also been studied.

The rest of this chapter is organized as follows: Section 5.1 introduces the principle of the VV, BPS, and KF-based estimators for compensating phase noise and joint phase and amplitude noise, respectively. Section 5.2 describes the transmission setup of the dispersion-unmanaged communication system, and corresponding results are discussed. Section 5.3 presents the transmission setup of the dispersion-managed submarine communication systems and the corresponding results. Section 5.4 is the summary.

5.1 Phase Noise Estimation Principle

5.1.1 System Model

Considering a nonlinear coherent optical communication system, the k^{th} received symbol r_k at the estimator can be formulated as follows

$$r_k = s_k \exp(j\theta_k) + n_k, \tag{5.1}$$

where $j \triangleq \sqrt{-1}$ is the imaginary unit, s_k denotes the k^{th} transmitted symbol from the modulator, θ_k involves the phase fluctuations induced by the LPN, the fibre nonlinearity and the signal-ASE noise interaction, and n_k includes the ASE noise, the EEPN, and the signal-EEPN interaction, depending on the specific transmission scheme. Note that, the EEPN and the signal-EEPN interaction noises are not applicable to in-line dispersion-managed systems.

5.1.2 Viterbi-Viterbi Carrier Phase Estimator

The VV algorithm eliminates signal phase modulation by taking the m^{th} power of m-PSK signals. The specific procedure of the VV CPE is to obtain the phase estimate of the central symbol in each block by taking the m^{th} power of each symbol in the processing unit of m-PSK signals and summing and averaging the computed phase over the entire block. The estimated phase noise of the k^{th} received symbol r_k using the VV CPE for an m-PSK transmission system can be calculated by [54, 150, 151]

$$\hat{\theta}_k = \frac{1}{m} \arg \left\{ \sum_{n=-(N_{\mathrm{V}}-1)/2}^{(N_{\mathrm{V}}-1)/2} r_{k+n}^m \right\}, \tag{5.2}$$

where $N_{\mathrm{V}} \in \{1, 3, 5, 7 \cdots\}$ is the block size of the VV CPE.

In order to improve the performance of the conventional VV CPE scheme for square-16QAM, the QPSK partition scheme has been applied in the VV CPE algorithm [152]. Fig. 5.1 shows a 16QAM constellation diagram for the illustration of the VV partitioning scheme. Two QPSK constellations with different amplitudes are formed by the symbols in the inner and outer rings (S_1). The symbols labelled as S_X and S_O in the middle ring of Fig.5.1 can be viewed as two separate groups of QPSK signals with different orientations. This partition scheme divides the 16QAM symbol points into subgroups of QPSK constellation points, which are S_1, S_X, and S_O as shown in Fig.5.1. The S_1 points can directly undergo VV CPE for QPSK. The symbols in the middle ring (S_X and S_O) can be rotated by either $+\theta_{rot}$ or $-\theta_{rot}$ ($\theta_{rot} = \pi/4 - \arctan(1/3)$) to correspond to QPSK constellations when using the VV estimator.

The flow chart of the 16-QAM VV CPE algorithm is shown in Fig. 5.2.

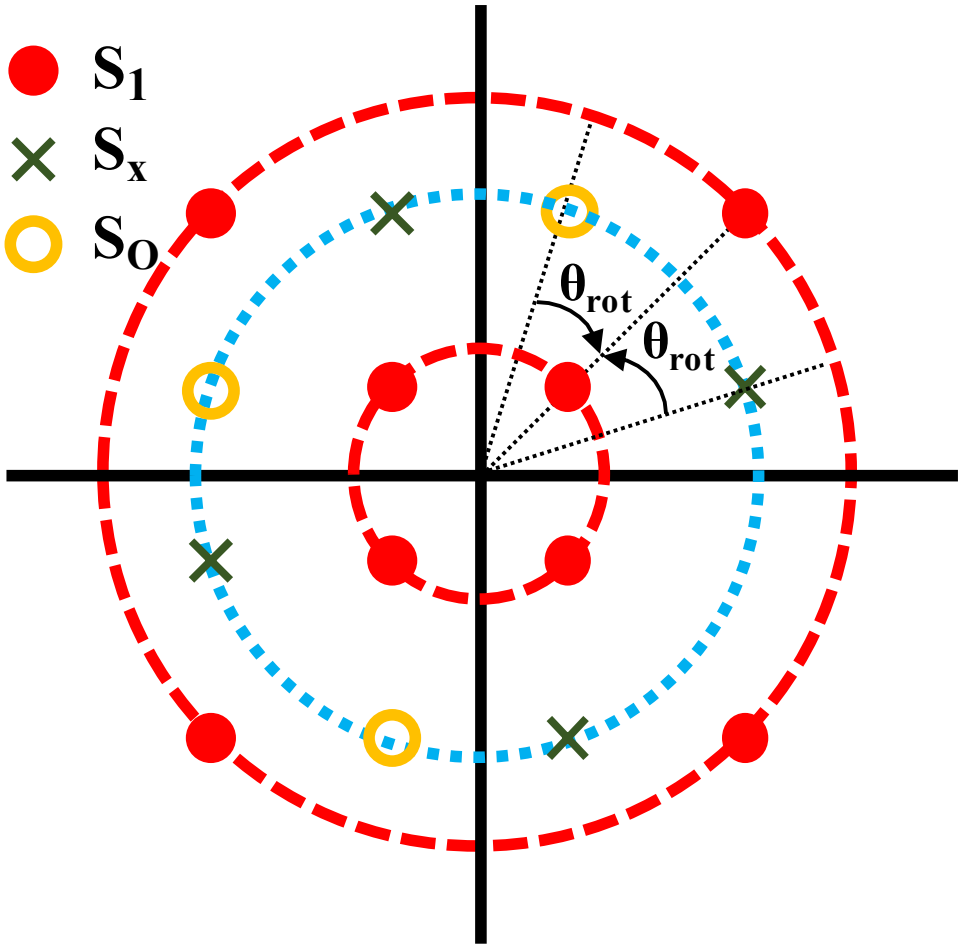

Figure 5.1: The partitioning scheme for the 16QAM VV CPE algorithm.

The algorithm works by first splitting the received signal into two different groups, S_1 and$S_{X,O}$, as shown in Fig. 5.1. Then, the symbol S_1 is directly quadratured to remove the phase modulation, and $S_{X,O}$ is rotated $\pm\theta_{rot}$ and quadratured to remove the phase modulation. To determine which of the two possible phase estimates of the symbols in the middle ring is correct, the mean estimate $< S_1^4 >$, which is the mean of all the S_1 symbols in the block is calculated. The mean estimate $< S_1^4 >$ and symbols in the block are normalized. Comparing $| < S_1^4 > -(S_{X,O}^+)^4|$ and $| < S_1^4 > -(S_{X,O}^-)^4|$ with the modulus operation $|\cdot|$, the symbols closest to $< S_1^4 >$ can be selected as the

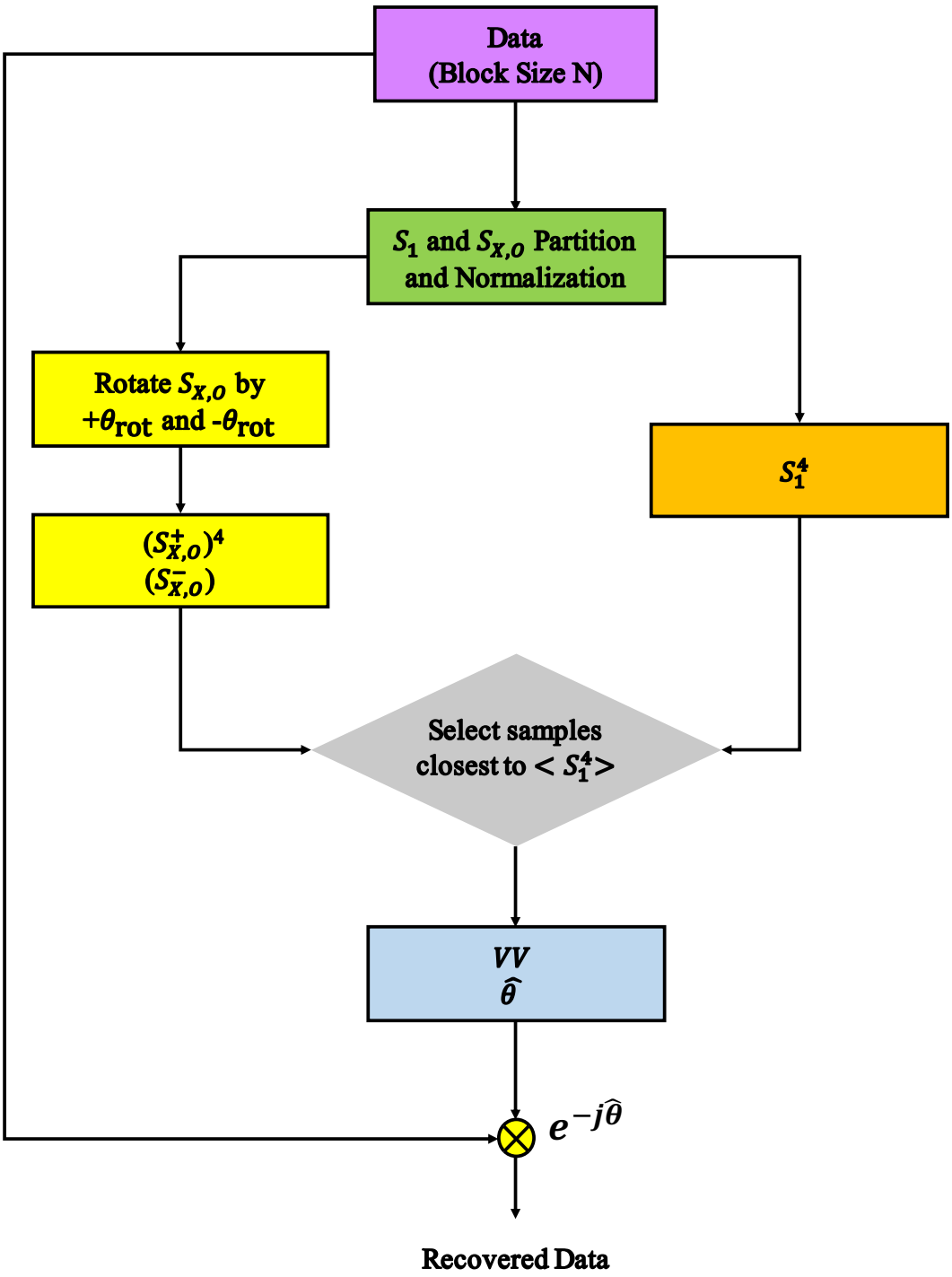

Figure 5.2: The processing steps of the 16QAM VV CPE algorithm.

phase noise estimate in the block of data. By removing the phase modulation for the 16QAM signals, the conventional VV CPE algorithm can be applied for the 16QAM for the phase estimate:

$$\hat{\theta}_k = \frac{1}{4} \arg \left\{ \sum_{n=-(N_V-1)/2}^{(N_V-1)/2} X_{k+n} \right\}, \tag{5.3}$$

where $X_k \in \left\{ S_1^4, \left(S_{X,O} \cdot e^{\pm j\theta_{rot}} \right)^4 \right\}$.

5.1.3 Blind Phase Search

The BPS carrier recovery algorithm was firstly proposed in [56], which can mitigate transmission phase noise effectively. The family of BPS has been widely investigated for phase noise estimation in recent years [55–60].

The principle of BPS is shown in Fig. 5.3. The received signal r_k at the input of the BPS is rotated by B test phase angles φ_b, which is given by

$$\varphi_b = \frac{b}{B} \cdot \frac{\pi}{2}, \; b \in \{0, 1, ..., B-1\}. \tag{5.4}$$

Then, the test symbols which have been rotated by B test phase angles are sent to a decision module and the squared distance $|d_{k,b}|^2$ between the test symbol and the nearest constellation point in the complex plane is calculated as

$$|d_{k,b}|^2 = \left| r_k \exp\{j\varphi_b\} - \hat{X}_{k,b} \right|^2, \tag{5.5}$$

where $\hat{X}_{k,b}$ is the nearest constellation point of the test symbol $r_k \exp\{j\varphi_b\}$, and is given by the decision circuit.

The squared distances of consecutive test symbols in a window with the

size of N_{BPS}, which are rotated by the same phase angle, are summed up as the following expression

$$s_{k,b} = \sum_{n=-(N_{\mathrm{BPS}}-1)/2}^{(N_{\mathrm{BPS}}-1)/2} |d_{k+n,b}|^2. \tag{5.6}$$

The optimum test phase angle for carrier phase noise compensation can be obtained by searching for the minimum value of $s_{k,b}$.

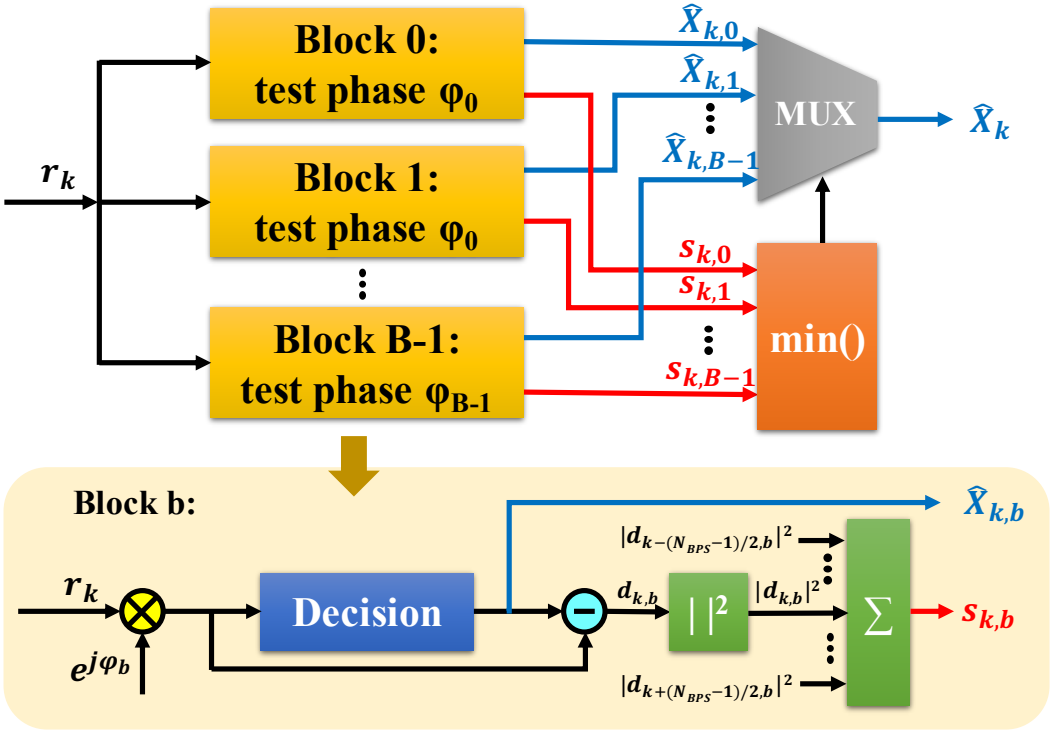

Figure 5.3: Block diagram of BPS estimator.

5.1.4 Kalman Filter Based Estimator

The KF is applied to estimate θ_k from the received symbol r_k [75] and feedback control is used to realize the estimation process. Specifically, the filter estimates the process state first and then uses the noise-corrupted measure-

ments as the feedback. Thus, the KF calculation procedure can be divided into two parts: the time update process and the measurement update process. The time update steps are used to project forward the state and the error covariance. The measurement update equations are used to obtain the feedback, and to improve the former state and error covariance estimate. The result of the time update process is an *a priori* estimate, and the result of the measurement update process is an *a posteriori* estimate.

The state space model for the KF can be represented as

$$\theta_k = \theta_{k-1} + w_k, \tag{5.7}$$

$$\widetilde{z}_k = \arg\left(r_k t_k^*\right) = \theta_k + v_k, \tag{5.8}$$

where w_k and v_k are the process and the measurement noise with covariances of $\widetilde{Q}$ and $\widetilde{R}$, respectively, $\widetilde{z}_k$ is the measurement variable, and t_k is the *decision* of $r_k e^{-j\hat{\theta}_{k|k-1}}$. In this work, the subscript $k|k-1$ denotes the *a priori* estimate at the k^{th} time instant, $\widehat{\cdot}$ denotes the estimate value, $\arg(\cdot)$ denotes the argument, and $(\cdot)^*$ is the complex conjugate.

The time update procedure of the KF-based estimator includes

$$\widehat{\theta}_{k|k-1} = \widehat{\theta}_{k-1}, \tag{5.9}$$

$$\widetilde{P}_{k|k-1} = \widetilde{P}_{k-1} + \widetilde{Q}, \tag{5.10}$$

where $\widetilde{P}$ denotes the error covariance.

The measurement update steps are defined as:

$$K_k \triangleq \frac{\widetilde{P}_{k|k-1}}{\widetilde{P}_{k|k-1} + \widetilde{R}}, \tag{5.11}$$

$$\widehat{\theta}_k = \widehat{\theta}_{k|k-1} + K_k \left(\widetilde{z}_k - \widehat{\theta}_{k|k-1} \right), \tag{5.12}$$

$$\widetilde{P}_k = (1 - K_k) \cdot \widetilde{P}_{k|k-1}, \tag{5.13}$$

with K_k being the Kalman gain.

The final symbol recovered by the KF-based estimator at the k^{th} time instant is given by

$$\widehat{s}_k = r_k \exp\left(-j\widehat{\theta}_k\right). \tag{5.14}$$

The block diagram of the KF-based estimator is shown in Fig. 5.4. Here, the initial values for $\widehat{\theta}_0$ and $\widetilde{P}_0$ are set as 0 and 1, respectively. Training symbols are used to initialize the phase estimation.

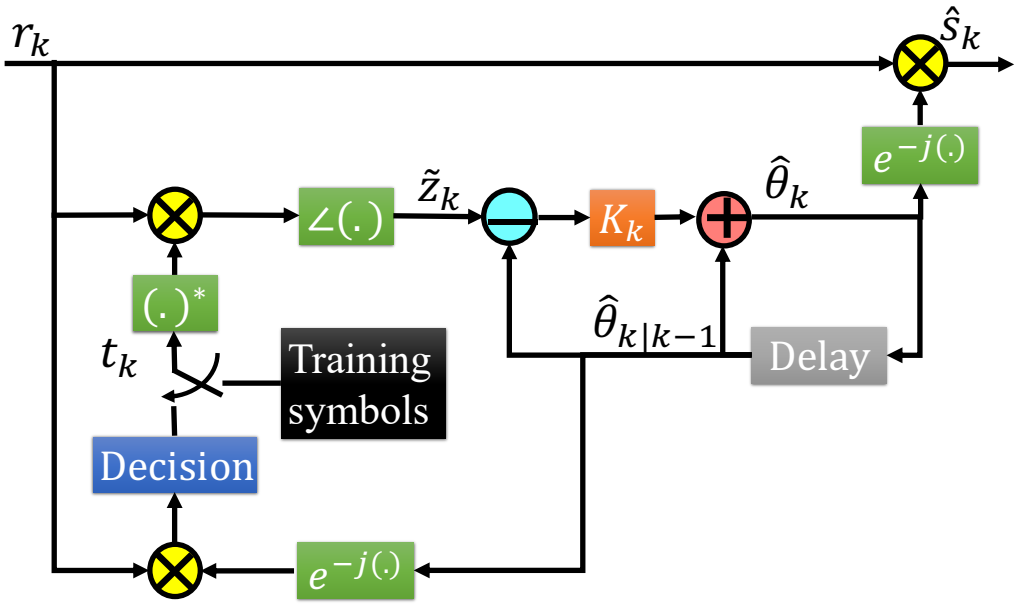

Figure 5.4: Block diagram of KF-based phase noise estimator.

Back-to-Back Communication Systems

In this section, the KF was preliminarily applied for tracking and compensating LPN in a 50-Gbaud DP-QPSK BTB transmission system. Simulation results show that KF can efficiently mitigate phase noise with 1-MHz laser linewidth.

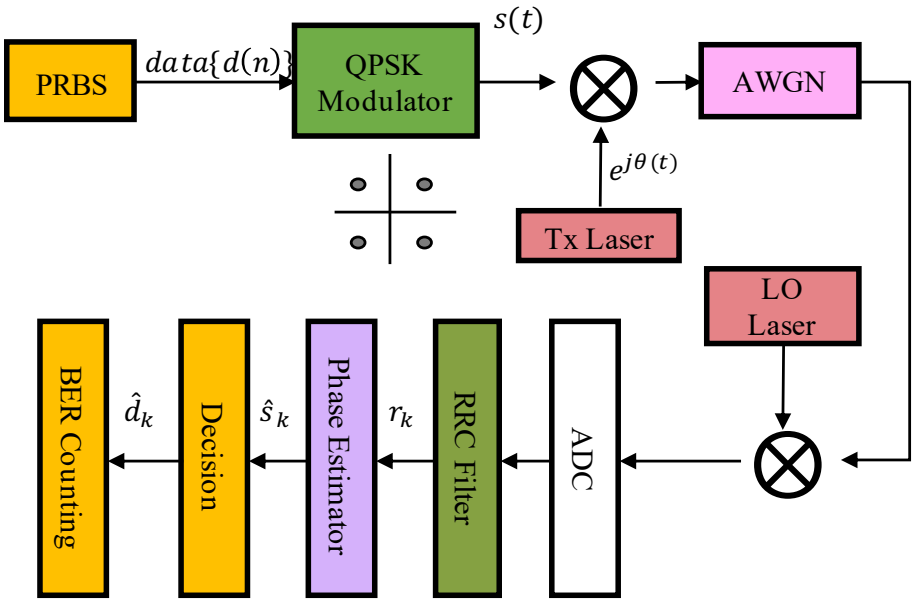

Figure 5.5: Schematic of QPSK modulation transmission system. PRBS: pseudo random bit sequence

Fig. 5.5 shows the coherent QPSK transmission system with KF used as a phase estimator. At the Tx, the symbols $d(n) \in \{1+j, 1-j, -1+j, -1-j\}$ were QPSK modulated and zero mean complex AWGN during the transmission process was added to this BTB system based on SNR. At the receiver, the received signal was mixed with a LO laser, which has the same frequency as the transmitter laser. The signal was down-converted using photodetectors and sampled by the ADCs. DSP modules included an RRC filter, phase estimator, symbol de-mapping, and BER measurement.

According to the detailed operation process of the KF-based phase esti-

mator in Fig. 5.4, the phase estimator consisted of a KF and a data detection stage. MATLAB was used to simulate the system shown in Fig. 5.5. At first, 100 training symbols were used to achieve convergence. Then the system was switched to decision-directed mode.

By simulation, the performance of tracking and compensating LPN with KF in a 50-Gbaud DP-QPSK BTB transmission system was investigated. As the performance of the Y polarisation was almost the same as that of the X polarisation, in this section only the X-polarisation results are presented and analysed. A total number of 2^{14} symbols were transmitted and the SNR was set to 30 dB. Fig. 5.6 (a)-(b) show the constellation diagrams for DP-QPSK without and with KF respectively, when Tx laser linewidth was set at 1 MHz and LO laser linewidth was 0 Hz. It can be found that the constellation diagram of the system without KF is closed due to the Tx LPN. After applying KF, the signal points are corrected to their original constellation positions, which indicates the efficient mitigation of the distortions. Fig. 5.6(c) shows the original and tracked phase noise trajectories with 1 MHz Tx laser linewidth and 30 dB SNR. It is observed that the tracked phase noise is almost completely coincident with the original phase noise, which indicates that KF can track the phase noise very well. In order to investigate the effectiveness of KF for tracking phase noise due to LO laser phase linewidth, performance for transmission with 1 MHz LO laser linewidth is shown in Fig. 5.7. Tx laser linewidth was set as 0 Hz. Other conditions were the same as those in Fig. 5.6. Similarly, it is observed that KF can also compensate and track phase noise due to LO laser linewidth as well.

Fig. 5.8 shows the X-polarisation constellation diagrams of DP-QPSK with KF when SNR was set to 30, 20, 10, and 5 dB respectively. It is found

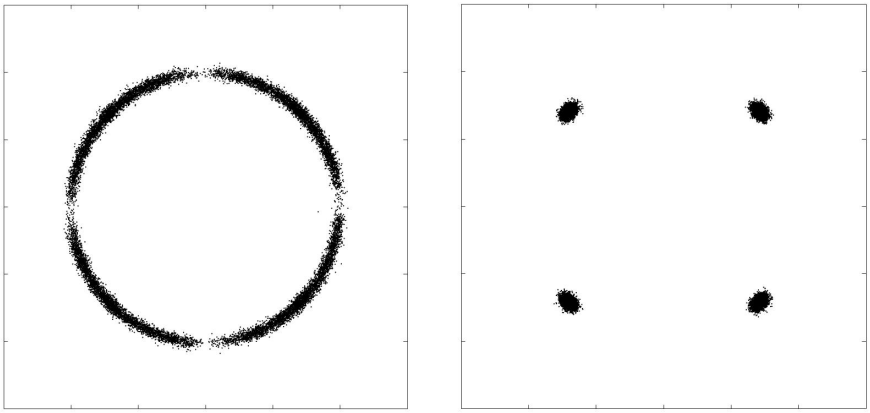

(a) (b)

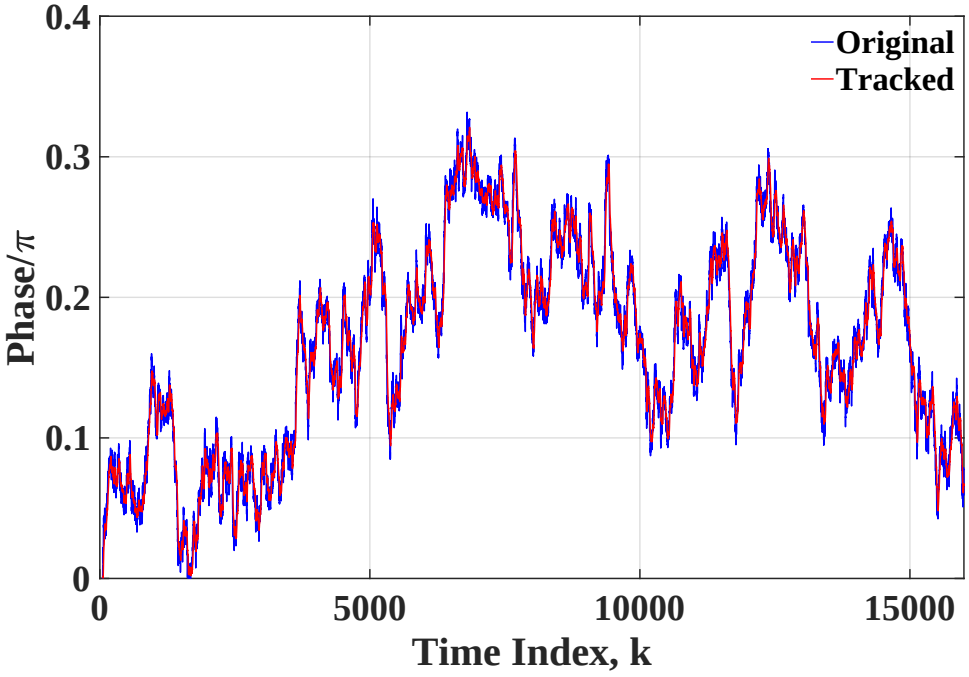

(c)

Figure 5.6: Performance for transmission with 1 MHz Tx laser linewidth at SNR=30dB. (a) Constellation diagram of DP-QPSK without KF. (b) Constellation diagram of DP-QPSK with KF. (c) Tracked phase noise at phase estimator output.

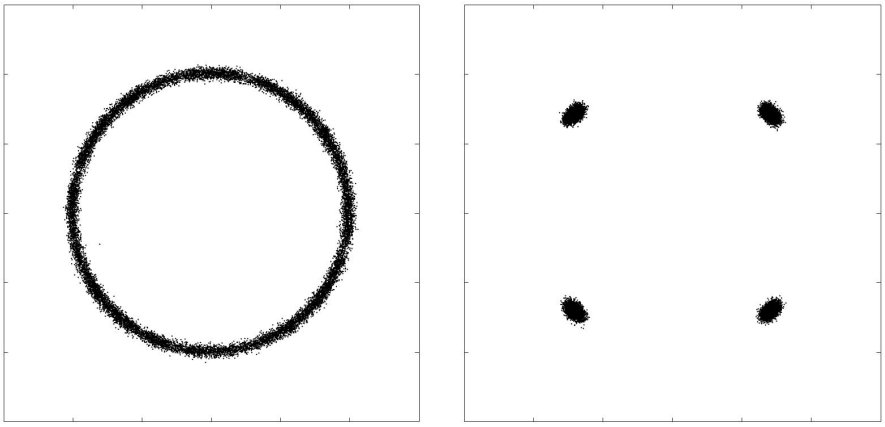

(a) (b)

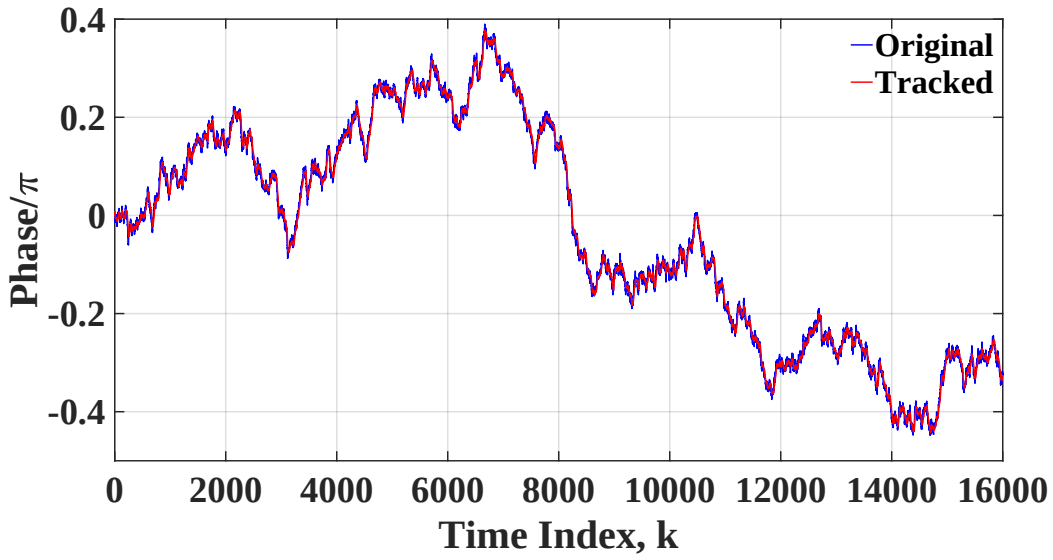

(c)

Figure 5.7: Performance for transmission with 1 MHz LO laser linewidth at SNR=30 dB. (a) Constellation diagram of DP-QPSK without KF. (b) Constellation diagram of DP-QPSK with KF. (c) Tracked phase noise at phase estimator output.

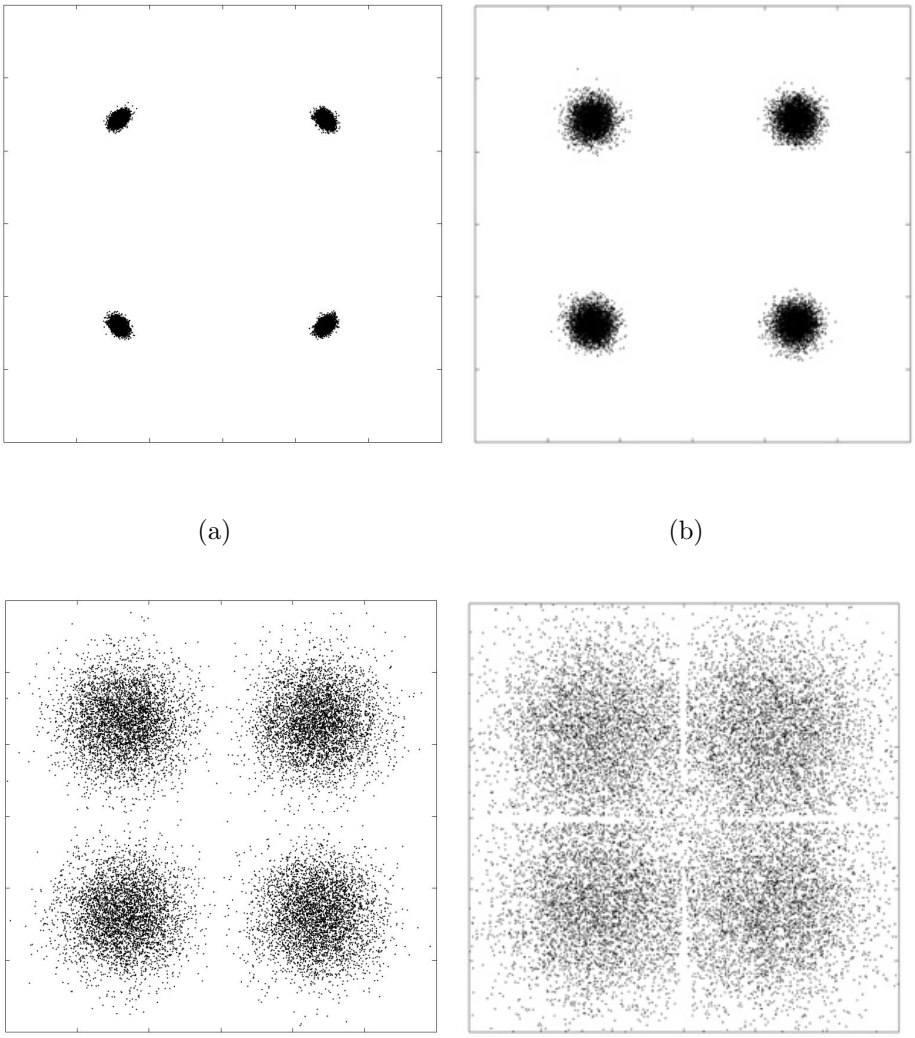

Figure 5.8: Constellation diagram of DP-QPSK with KF at SNR of (a) 30 dB, (b) 20 dB, (c) 10 dB, (d) 5 dB respectively.

that with the decrease of SNR, more signal points gradually deviate from their original positions, which leads to the increasing radius of constellation points. Fig. 5.9 shows BER as a function of SNR, for a 50-Gbaud DP-QPSK BTB transmission system with KF. As has been shown, with the growth of SNR from 0 to 12 dB, BER reduces dramatically, and after 12 dB SNR, the value

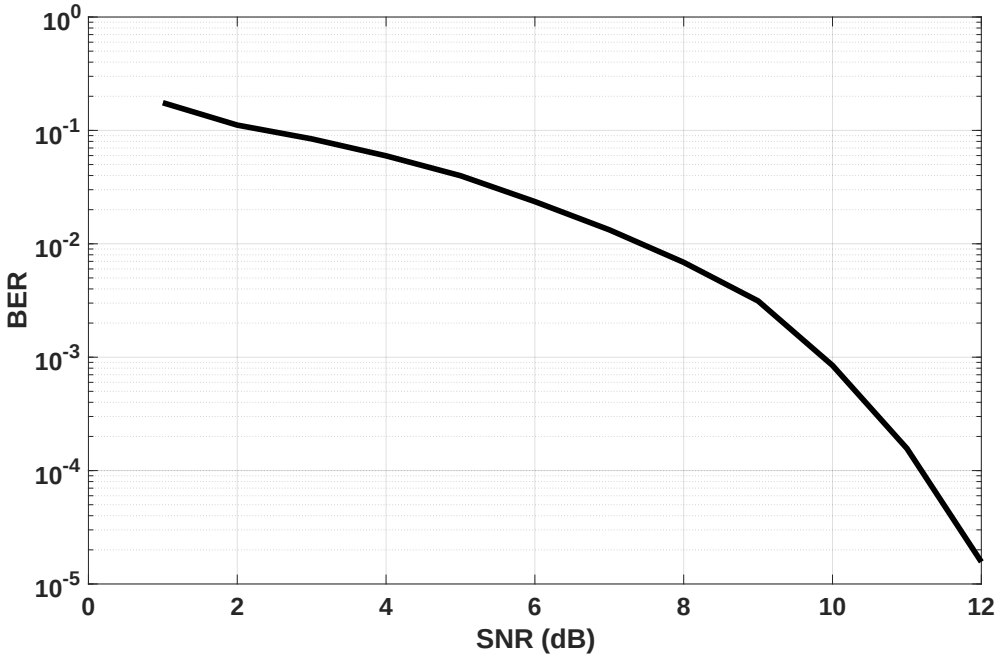

Figure 5.9: BER as a function of SNR, for 50-Gbaud DP-QPSK BTB transmission system with KF-based estimator.

of BER tends to zero. Tracked phase noise at phase estimator output when SNR was set as 10 dB, and 5 dB is shown in Fig. 5.10, which indicates that KF can track phase noise efficiently at a relatively low SNR.

5.2 Dispersion-Unmanaged Optical Communication Systems

5.2.1 Transmission System

To investigate the performance of the KF-based estimators on distortion compensation, numerical simulations have been carried out in both single- and 5-channel 32-GBd Nyquist-spaced dispersion-unmanaged optical fibre communication systems. The modulation formats DP-QPSK and DP-16QAM have

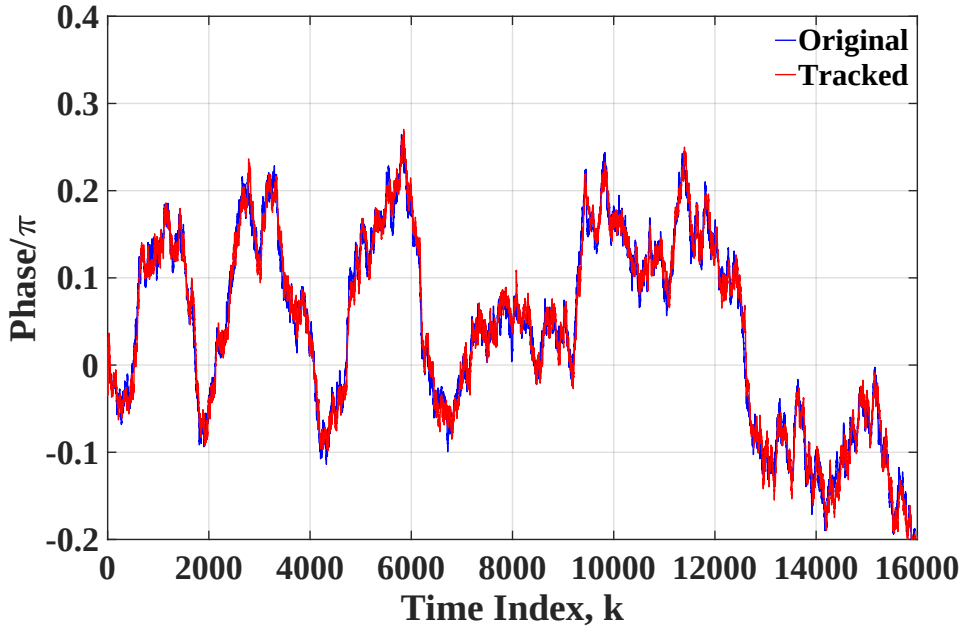

(a)

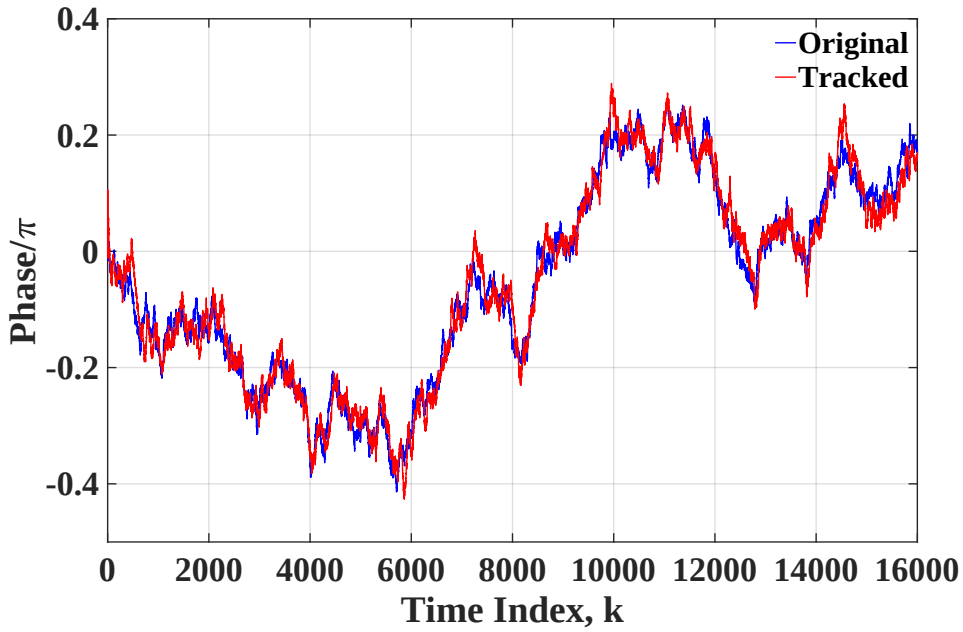

(b)

Figure 5.10: Tracked phase noise at phase estimator output at SNR of (a) 10 dB and (b) 5 dB.

been applied. The system setup is described in Fig. 5.11. At the Tx, a 32-GHz spaced laser comb was used as the source of the optical carrier. The transmitted symbol sequences were fully random and independent in different polarisations and channels. 0.1% RRC filters were employed for NPS. In the transmission channel, a 1600 km SSMF link was applied with a span length of 80 km. The signal propagation over the fibre was simulated based on the split-step Fourier solution of the Manakov equation [102,143]. After the transmission over each span, an EDFA with a noise figure of 4.5 dB was applied to compensate for the fibre loss.

At the coherent Rx, the received signals were mixed with a LO laser

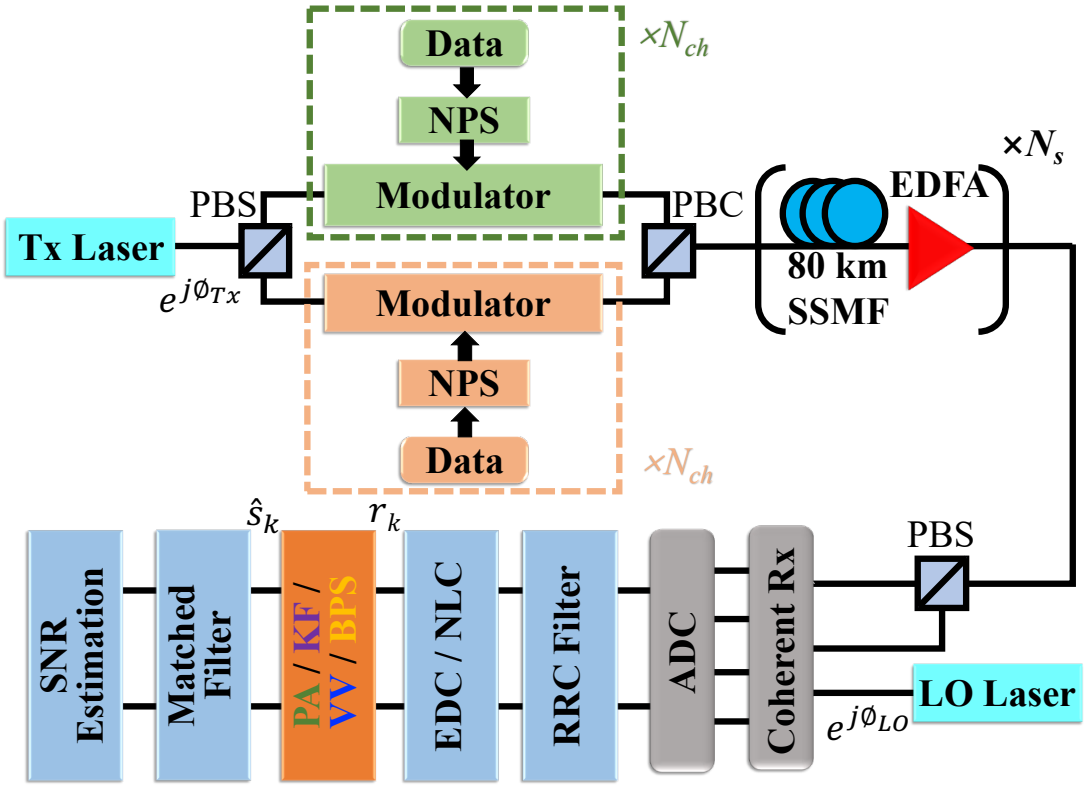

Figure 5.11: Schematic of the dispersion-unmanaged optical communication system.

carrier (with a 100 kHz linewidth). The signals were detected by photodiodes and were further sampled by ADCs. In the DSP modules, a 0.1% roll-off RRC filter was applied to select the bandwidth for the following module. An EDC or a full-field NLC module was chosen to compensate for CD only or both CD and fibre nonlinearity. An FDE was employed as the EDC module [21]. The NLC was implemented based on the reverse split-step Fourier solution of Manakov equation [144]. The pilot-aided (PA) CPE, the KF-based estimator, the VV algorithm and the BPS CPE have been applied, respectively, for the compensation of residual transmission distortions. The PA CPE has been widely employed for the LPN compensation [153–159], where a pilot carrier is generated and transmitted to record the Tx and the LO laser phase fluctuations. In numerical simulations of this chapter, the PA CPE was simply achieved using the conjugate multiplication between the received signal and the artificially recorded intrinsic LPN from both Tx and LO lasers. The PA CPE can fully remove the intrinsic LPN from Tx and LO lasers, and was applied here as a reference to investigate the capability of the KF in eliminating the impact of LPN, fibre nonlinearity, ASE noise as well as EEPN. The noise covariances for the KF and the tap length for VV CPE were set with optimal values to maximize the performance by exhaustive search. The observed channel was selected by the matched filter, which was also achieved by a 0.1% roll-off RRC filter. Finally, the performance of the selected channel is estimated in terms of the SNR, which was calculated by the ratio between the sum of the expectation and the sum of the variance of the received symbol within each constellation cluster [42, 160]. The laser frequency offset and the PMD were neglected in numerical simulations. Detailed parameters of the transmission systems are given in Table 5.1. SSMF parameters including the attenuation coefficient,

the CD coefficient and the nonlinear coefficient are listed in Table 5.2.

In this scenario, the received symbol r_k before the estimator was severely distorted by the effect of NLI, LPN, ASE noise, and EEPN. After the NLC module, since the NLI had been cancelled, the signal-ASE noise interaction and the signal-EEPN interaction became significant in addition to ASE noise, LPN and EEPN.

Table 5.1: Transmission System Parameters

Parameters	**Values**
Central wavelength (λ_0)	1550 nm
Symbol rate (R)	32 GBd
Channel spacing	32 GHz
Number of channels (N_{ch})	$\{1, 5\}$
Modulation format	{QPSK, 16QAM}
Roll-off factor	0.1%
EDFA noise figure (NF)	4.5 dB
LO laser linewidth	100 kHz
Number of spans (N)	20

Table 5.2: Fibre Parameters

Fibre Type	**SSMF**	**DCF**
Attenuation coefficient (α)	0.2 dB/km	0.5 dB/km
CD coefficient (D)	17 ps/nm/km	– 85 ps/nm/km
Nonlinear coefficient (γ)	1.2 /W/km	5.67 /W/km

5.2.2 Results and Discussions

Fig. 5.12 shows the results of SNR versus signal power for the single-channel DP-QPSK dispersion-unmanaged coherent optical communication system, where EDC and NLC are applied, respectively. The cases of using the PA CPE, the KF-based estimator, the VV algorithm and the BPS approach are taken into account. It is observed that all applied compensation schemes can effectively

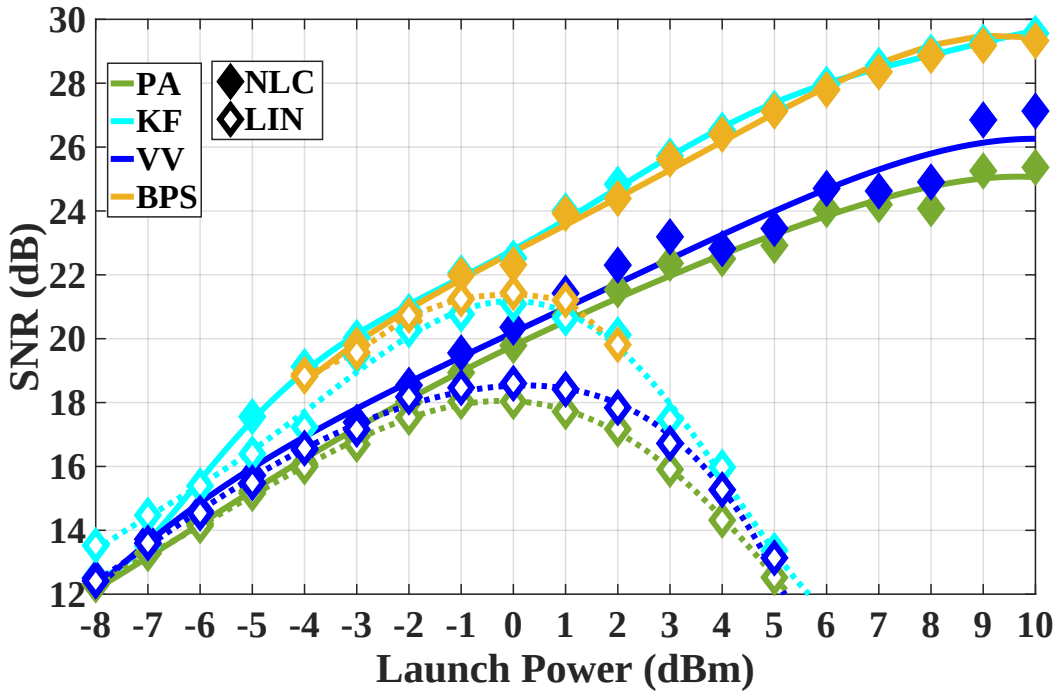

Figure 5.12: The SNR as a function of launch power per channel in the DP-QPSK dispersion-unmanaged system with the single-channel transmission. The transmission distance is fixed at 1600 km.

improve the system performance. The KF-based estimator schemes achieve higher SNRs than the PA CPE does, in systems both with and without the NLC. The VV CPE performs similarly to the PA CPE. The KF outperforms the VV scheme. The performance of the BPS is similar to that of the KF CPE. However, it could also be observed that the BPS works effectively only at the signal launch power of -4 dBm to 2 dBm in the linear compensation scenario, as the performance of BPS might falter when the distinction between the CPEs of adjacent symbols falls beyond the range of $[-\pi/4, \pi/4]$, resulting in the occurrence of phase cycle-slip in the case of square mQAM formats. This indicates that the operating margin of the BPS approach is less than that of the KF. It can be found that the KF scheme achieves 3.05 dB and 4.19 dB

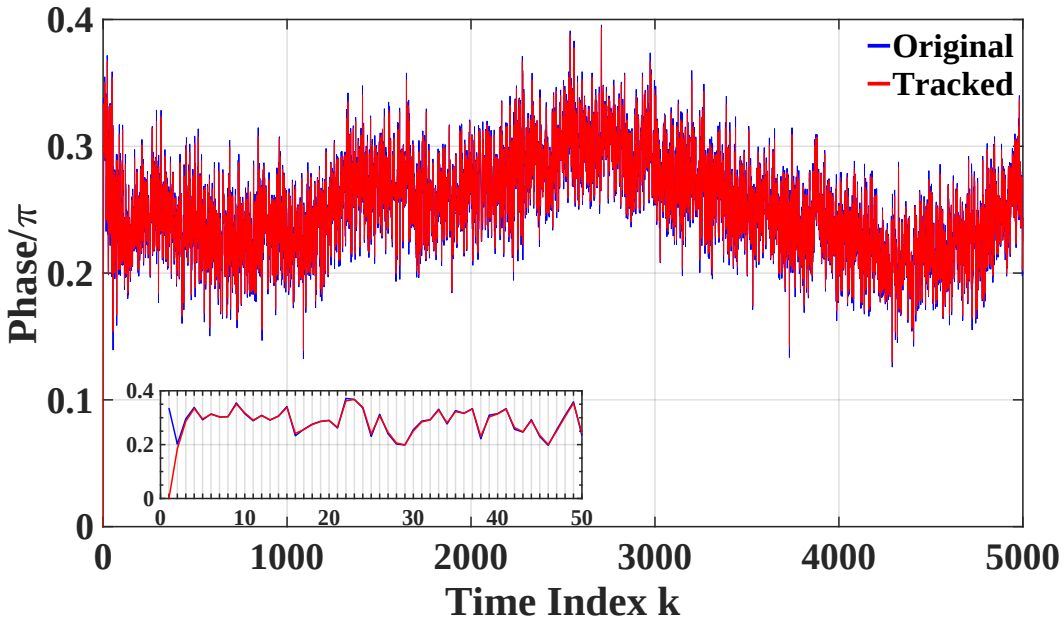

Figure 5.13: Comparison between tracked phase noise by KF CPE and original phase noise in the DP-QPSK single-channel 1600 km dispersion-unmanaged system at optimum power of 0 dBm (LIN)

higher SNRs compared to the PA CPE in systems with EDC and NLC, respectively. Moreover, the KF scheme can deliver 2.43 dB higher SNRs than the VV estimator in the NLC scenarios. The great performance improvement by employing the KF estimator in EDC and NLC scenarios indicates its strong capability in phase noise removal. In this chapter, (LIN) and (NLC) are used to represent the systems with linear dispersion compensation only and with NLC, respectively. Fig. 5.13 shows the tracked phase noise by the KF CPE and the total phase fluctuations in symbols in the DP-QPSK single-channel 1600 km dispersion-unmanaged system at the optimum power of 0 dBm (LIN). It indicates that KF can track the phase noise in the received symbols well. The inset indicates that the optimized KF can track the phase noise well after a few iterations only.

Fig. 5.14 shows the results for the single-channel DP-16QAM dispersion-

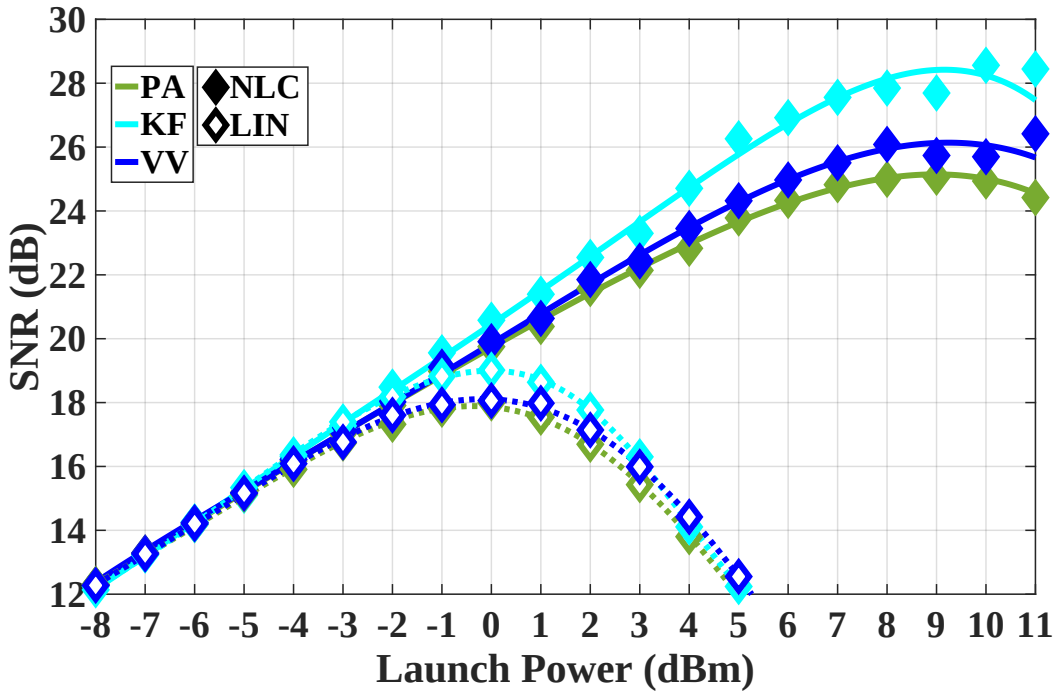

Figure 5.14: The SNR as a function of launch power per channel in the DP-16QAM dispersion-unmanaged system with the single-channel transmission. The transmission distance is fixed at 1600 km.

unmanaged coherent optical communication system in the cases of EDC and NLC. It is observed that the system including the KF-based estimators achieves higher SNRs than the system using the VV estimator and the PA CPE in both cases of EDC and NLC, which reveals that the KF also works effectively for phase noise estimation in 16-QAM systems. The constellation partitioning approach [152] has been employed in the VV estimation for the 16QAM system. The performance of the VV CPE is slightly better than that of the PA CPE in the NLI scheme. The KF scheme achieves a 3.62 dB and 1.07 dB higher SNR than the PA CPE scheme for the cases of NLC and EDC, respectively.

Fig. 5.15 shows the results for the 5-channel Nyquist-spaced DP-QPSK dispersion-unmanaged coherent optical communication system in the cases of

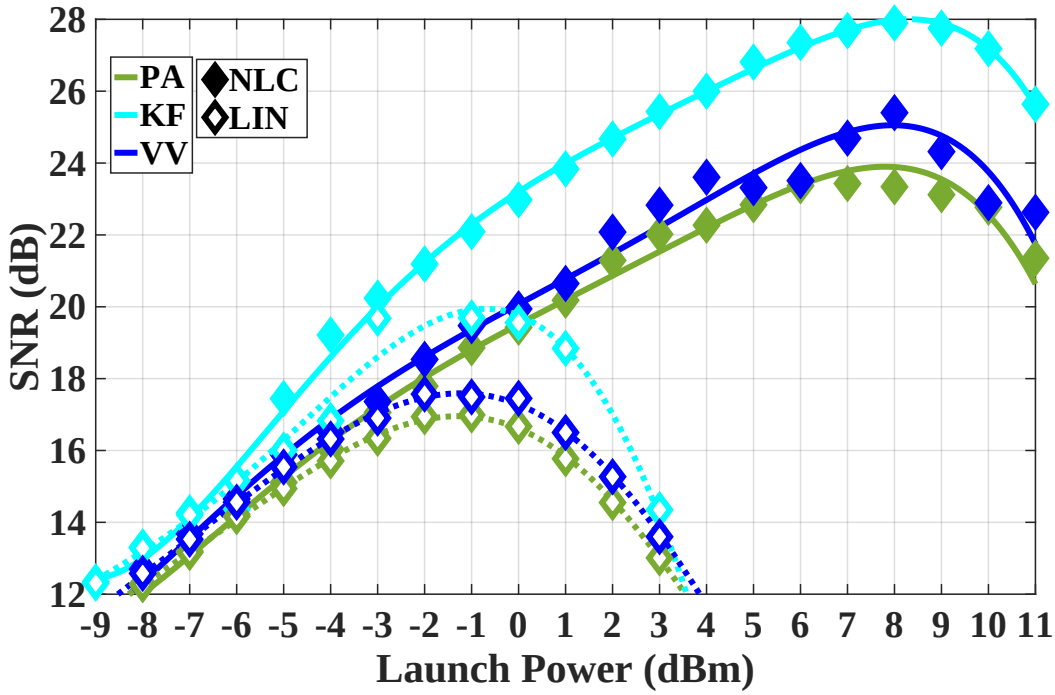

Figure 5.15: The SNR as a function of launch power per channel in the DP-QPSK Nyquist-spaced dispersion-unmanaged system with the 5-channel transmission. The transmission distance is fixed at 1600 km.

EDC and NLC. Similar to the results of the single-channel DP-QPSK system, the KF scheme outperforms the PA CPE and the VV estimator in both cases of EDC and NLC. As described in Fig. 5.15, the KF in the system with EDC achieves 2.70 dB and 2.20 dB higher SNRs than the PA CPE and the VV approach in the systems, respectively. Additionally, the SNR for the KF case is 2.49 and 4.56 dB higher than that for the VV and the PA scheme for the case of the NLC.

To further investigate the performance of the KF-based estimator in practical applications, the impact of TRx noise has also been taken into consideration. Fig. 5.16 shows the SNR as a function of launch power per channel in the 5-channel DP-QPSK Nyquist-spaced dispersion-unmanaged 1600 km

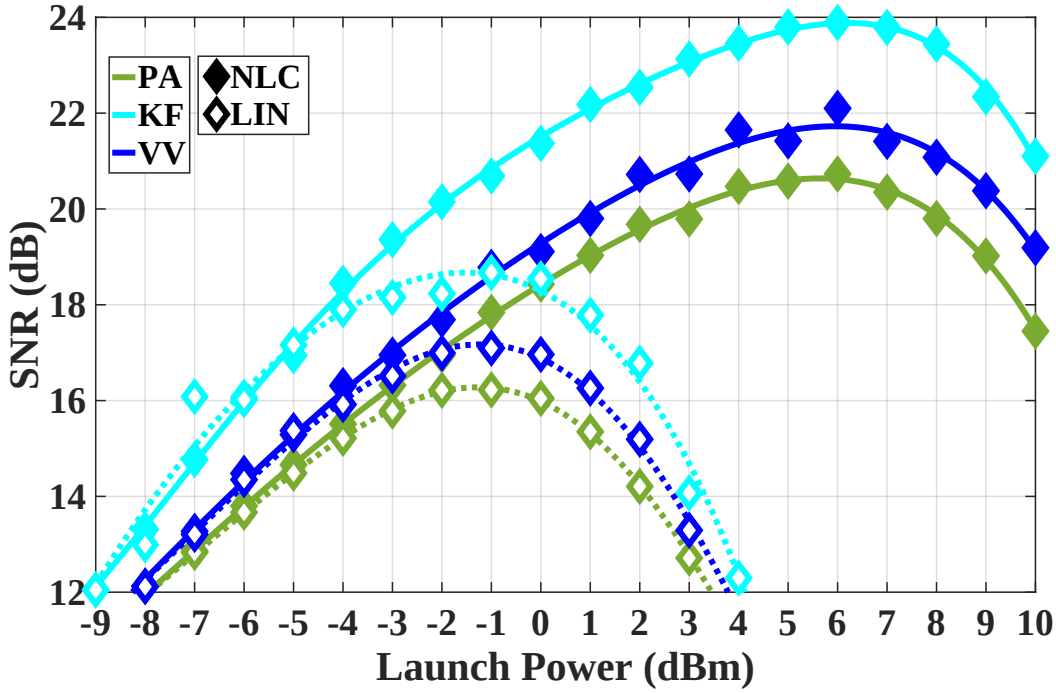

Figure 5.16: The SNR as a function of launch power per channel in the 5-channel DP-QPSK Nyquist-spaced dispersion-unmanaged system with 25 dB TRx noise. The transmission distance is fixed at 1600 km.

system with 25 dB TRx noise. TRx noise consists of distortions from Tx and Rx components including DACs and ADCs, linear electrical amplifiers, and some optical devices [34]. A similar tendency with that in Fig. 5.15 can be observed, while the overall system performance is compressed by TRx noise. Improvements of 1.58 dB and 1.79 dB in the system are obtained by the KF scheme compared with the VV CPE in this scenario applied with EDC and NLI, respectively. Compared with PA CPE, 2.45 dB and 3.16 dB higher SNRs have been achieved by the KF scheme for cases of EDC and NLC, respectively.

5.3 Dispersion-Managed Optical Communication Systems

5.3.1 Transmission System

Numerical simulations have also been carried out for DP-QPSK and the DP-16QAM Nyquist-spaced 32-GBd WDM optical dispersion-managed communication systems. Many installed long-haul transoceanic links employ in-line optical dispersion management by multi-span cascades of SSMF and DCF [20]. The simulation setup is described in Fig. 5.17. The Tx setup was the same as that employed in the dispersion-unmanaged transmission system as described in Section 5.2.1. In the transmission link, the SSMF was 50 km and the DCF

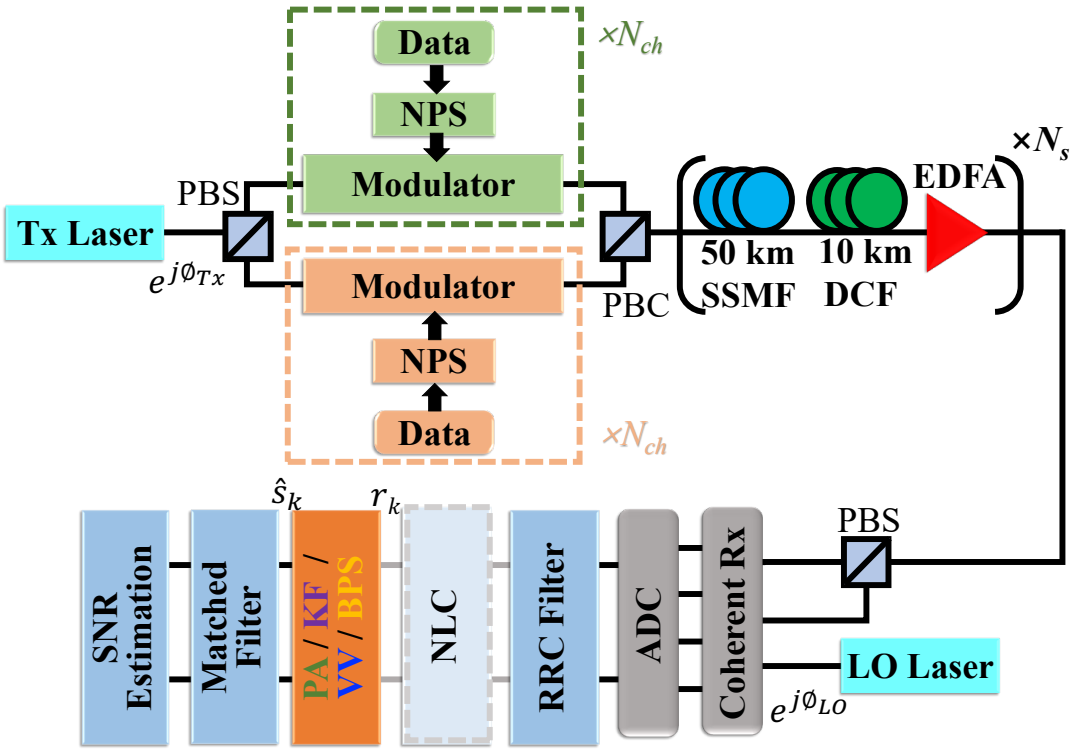

Figure 5.17: Schematic of the dispersion-managed optical communication system.

was 10 km at each fibre span. The CD generated in each SSMF could be fully mitigated in the cascaded DCF. This research assumed 20 spans (corresponding to 1000 km of SSMF, net of DCF). Each loop loss (both from SSMF and DCF) was exactly compensated by an EDFA with a 4.5 dB noise figure. At the coherent Rx, the received signals were mixed with the LO laser carrier having a 100 kHz linewidth. Rx-side full-field NLC was applied to remove fibre nonlinearities. Then a PA CPE, a KF-based estimator, or a VV CPE were employed. The observed channel was selected via the matched filter, and the performance was estimated by the value of the SNR. Laser frequency offset and PMD were again neglected. Detailed parameters of the dispersion-managed transmission system can also be seen in Table 5.1, and fibre parameters are provided in Table 5.2.

In this transmission scenario, the symbol r_k received at the estimator was severely distorted by the joint effects of the fibre nonlinearity, the LPN, the ASE noise, and the nonlinear interaction between signals and ASE noise [161]. In contrast to dispersion-unmanaged systems, the dispersion-managed system did not suffer from the EEPN effect, and the fibre nonlinearities in this scenario led to nonlinear phase distortion only due to the full inline compensation of the dispersion. The KF-based estimators described in Section 5.1.4 were applied to mitigate existing phase distortions in dispersion-managed systems.

5.3.2 Results and Discussions

Fig. 5.18 shows the results for the single-channel DP-QPSK in-line dispersion-managed coherent optical communication system with and without the NLC module. It is observed that the KF-based CPE, the VV CPE and the BPS

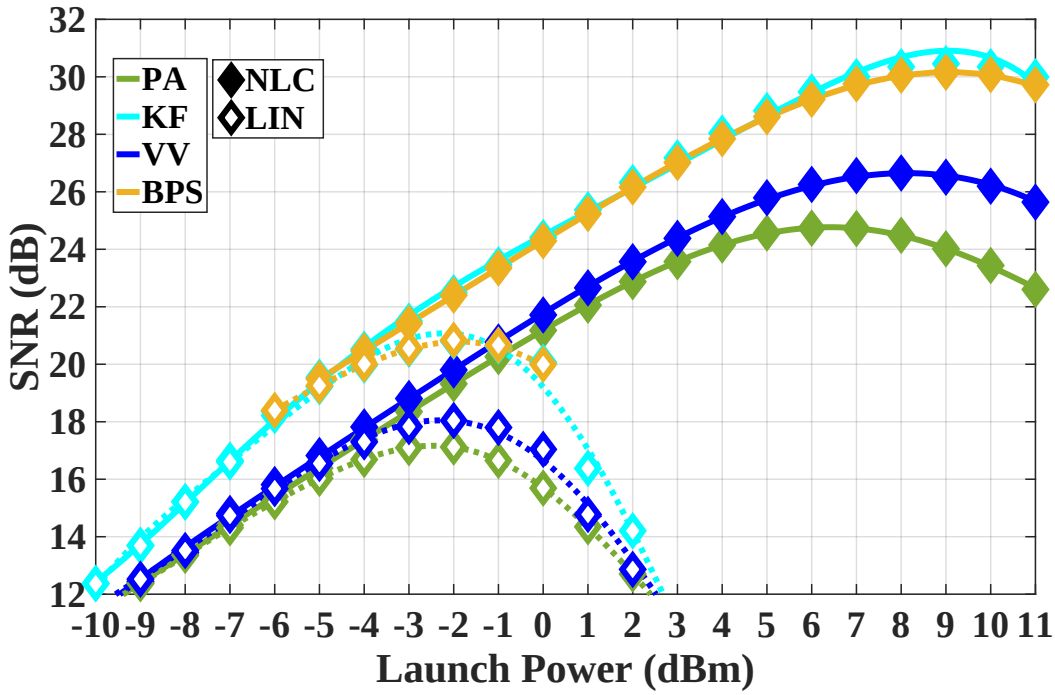

Figure 5.18: The SNR as a function of launch power per channel in the DP-QPSK dispersion-managed system with the single-channel transmission. The transmission distance is fixed at 1000 km.

algorithm can greatly improve the system performance, and all of them can achieve higher SNRs than the PA CPE, in both systems with and without the NLC. The performance of the VV CPE stays close to that of the PA CPE. Both of them can compensate well for the LPN. The BPS approach behaves similarly to the KF, while the KF has better tolerance to severe impairments than the BPS does. The KF scheme can achieve 3.72 dB and 2.79 dB higher SNRs than the PA CPE and the VV estimator in the EDC scenario at their optimum powers, and it can also obtain 3.95 dB and 6.44 dB higher SNRs than the PA CPE and the VV estimator in the NLC scenario, respectively. Fig. 5.19 shows the tracked phase noise by the KF CPE and the total phase fluctuations in symbols at the optimum power of -2 dBm (LIN). It indicates

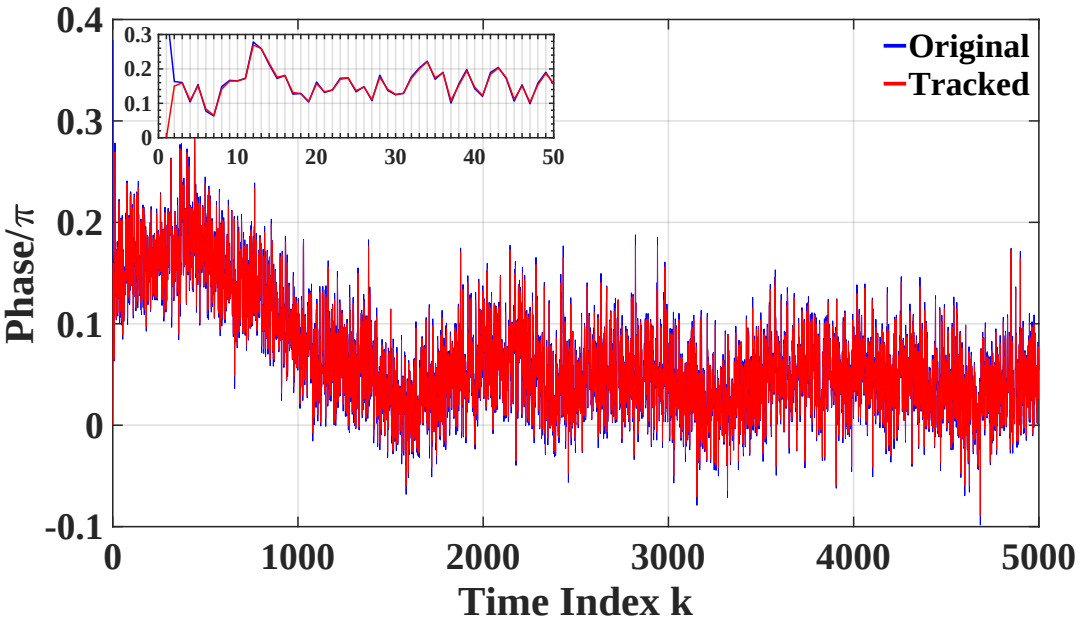

Figure 5.19: Comparison between tracked phase noise by KF CPE and original phase noise in the DP-QPSK single-channel 1000 km dispersion-managed system at optimum power of -2 dBm (LIN)

that KF can track the original phase noise in the received symbols well and KF has fast convergence to the correct operation.

Fig. 5.20 shows the results for the single-channel DP-16QAM dispersion-managed transmission system with and without the NLC module. It is found that in both NLC and LIN DP-16QAM systems, the KF-based CPE achieves better performance than the VV estimator and the PA CPE. It indicates the strong capability of the KF on the phase distortion mitigation for 16QAM systems. The VV CPE (based on the constellation partitioning) behaves the same as the PA CPE. At the optimum power in the case of NLC, the gap between the peak SNRs of the KF and the VV schemes is ~ 6 dB.

Fig. 5.21 shows the results for 5-channel DP-QPSK submarine dispersion-managed Nyquist-spaced optical communication systems with and without the NLC module. It can be found that the KF and the VV approaches perform

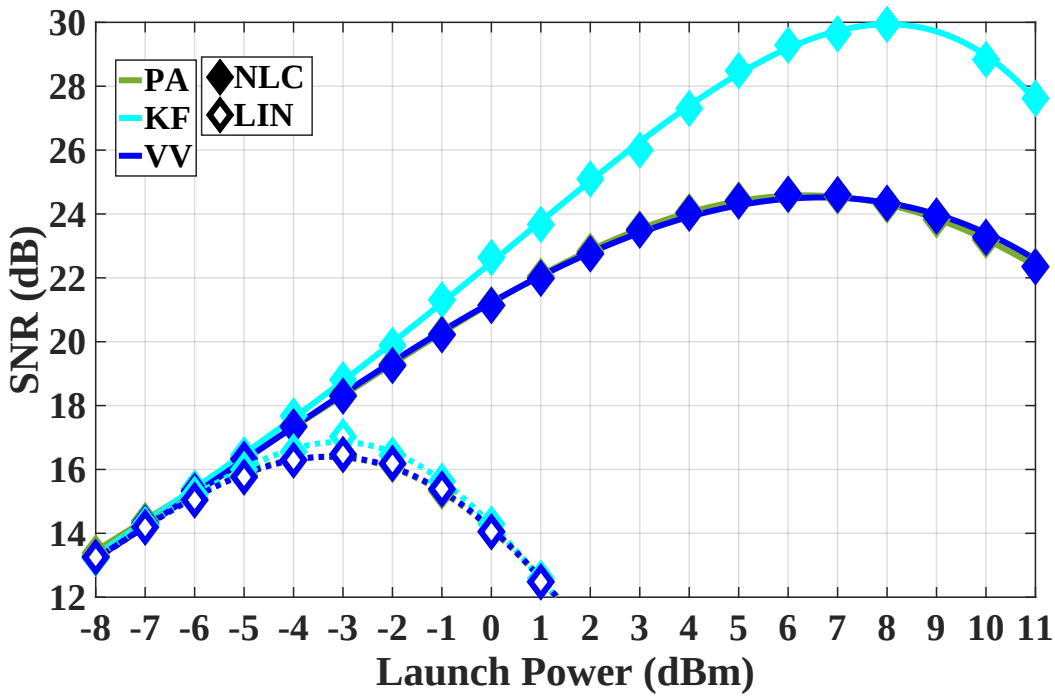

Figure 5.20: The SNR as a function of launch power per channel in the DP-16QAM dispersion-managed system with the single-channel transmission. The transmission distance is fixed at 1000 km.

better than PA CPE, and the KF obtained the best performance. The KF scheme achieves 2.00 dB and 3.22 dB higher SNRs than the VV CPE does for the cases of NLC and LIN, respectively. The KF (LIN) scheme attains 2.68 dB higher SNR than the PA CPE (LIN) does at their optimum powers.

A 5-channel DP-QPSK Nyquist-spaced dispersion-managed system with 25 dBm TRx noise is investigated as well for exploring the practical application of the KF. Results are as shown in Fig. 5.22. The KF presents excellent capability for system performance improvement despite the severe TRx noise, where SNR obtained by the KF scheme exceeds PA CPE by 2.34 dB and 4.27 dB for the cases of LIN and NLC, respectively.

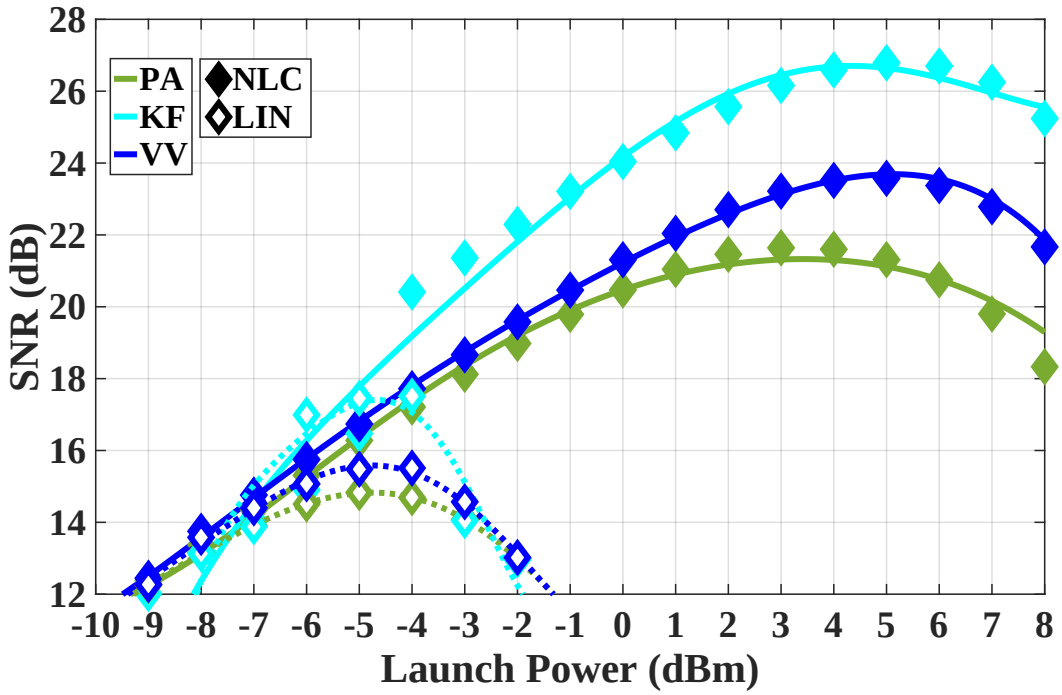

Figure 5.21: The SNR as a function of launch power per channel in the DP-QPSK Nyquist-spaced dispersion-managed system with the 5-channel transmission. The transmission distance is fixed at 1000 km.

5.4 Summary

Comprehensive investigations of KF-based estimators have been performed in BTB, dispersion-unmanaged and dispersion-managed long-haul nonlinear optical fibre transmission systems. The VV estimator, the PA CPE, and the BPS have been implemented as references for comparison. The impacts of TRx noise have been investigated in Nyquist-spaced WDM systems.The analysis of the results reveals the following insights:

- Great system performance improvement is observed, which indicates the capability of the KF to mitigate the phase impairments caused by LPN, EEPN, ASE noise, and NLI simultaneously.

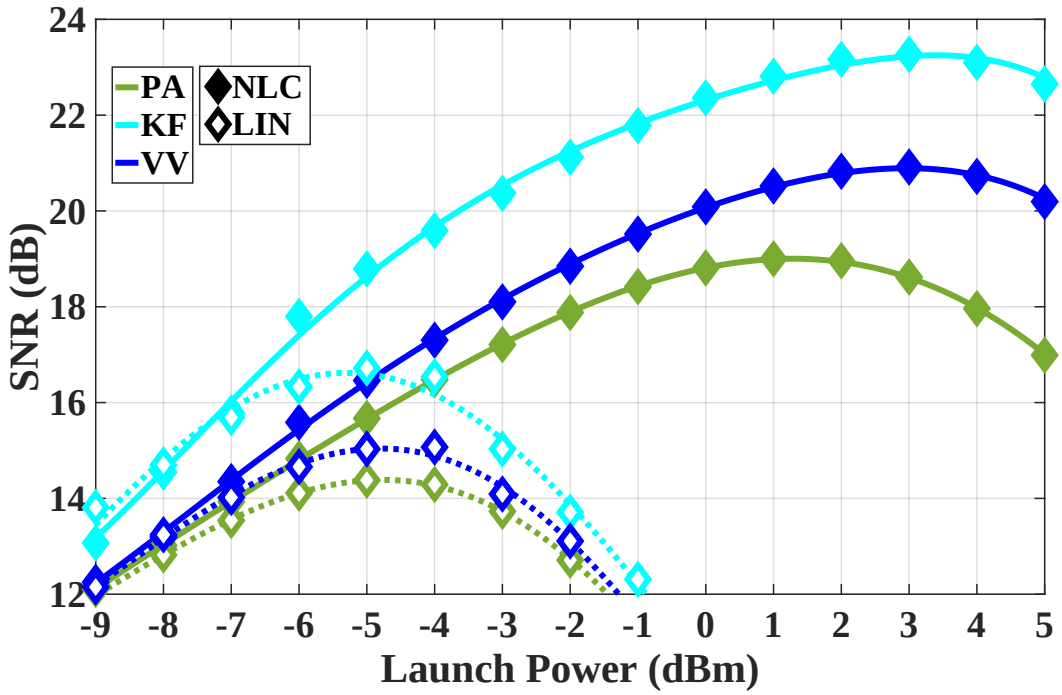

Figure 5.22: The SNR as a function of launch power per channel in the 5-channel DP-QPSK Nyquist-spaced dispersion-managed system with 25 dB TRx noise. The transmission distance is fixed at 1000 km.

- The KF scheme outperforms the VV scheme in both dispersion-unmanaged and dispersion-managed optical transmission systems, considering the modulation formats of DP-QPSK and DP-16QAM. This is true for both NLC and LIN.

- Joint application of the KF and the NLC can significantly improve the system performance. ∼4 dB higher SNRs were achieved by the KF scheme compared with the PA CPE in both the dispersion-unmanaged and the dispersion-managed WDM DP-QPSK and DP-16QAM systems applied with the NLC. This indicates that the KF can greatly mitigate phase distortions.

This work provides significant insight into the application of the KF-

based estimators in both dispersion-unmanaged terrestrial and dispersion-managed legacy submarine long-haul optical transmission systems, considering more practical limitations from fibre nonlinearity, LPN, TRx noise and EEPN. The results indicate that the KF can be an excellent solution for mitigating phase impairments caused by ASE noise, EEPN, NLI, signal-EEPN and signal-ASE noise interactions, simultaneously with a low computation complexity.

Chapter 6

Conclusions

This thesis extensively studies advanced modelling and signal processing in nonlinear coherent optical fibre systems, with the aim of predicting and improving the overall system performance, which is crucial to meeting the demands of high-capacity data transmission. Section 6.1 provides a summary of the significant findings obtained from the study. In addition, Section 6.2 outlines the potential areas that could be beneficial to explore in future research.

6.1 Summary of Research

To meet the ever-increasing demand for data, it is crucial to achieve higher information rates. However, the presence of optical Kerr nonlinearity in fibre poses a significant challenge to enhancing achievable information rates in optical fibre communication systems. This nonlinearity causes distortions in multi-channel WDM optical fibre communication systems, which greatly limit their capacity. The Kerr effect in optical fibres inherently limits the achievable information rates of optical communication systems, particularly

in systems with larger transmission bandwidths, closer channel spacing, and higher-order modulation formats. In Chapter 3 of this thesis, the effectiveness of NLC techniques, such as DBP and OPC, is examined for improving AIRs in fully-loaded $C-$band systems that use both lumped EDFA and distributed Raman amplification. The study takes into account practical TRx limitations and explores the performance of various modulation formats, including DP-QPSK, DP-16QAM, DP-64QAM, and DP-256QAM, over different transmission distances. The results indicate that the effectiveness of NLC techniques in enhancing achievable information rates depends heavily on the signal modulation formats and target transmission distances. NLC is more effective for higher-order modulation formats at shorter system distances. Particularly, for the analysed transmission distances up to 10,000 km, it is not necessary to use NLC for DP-QPSK systems. Moreover, TRx noise has a negligible effect on AIRs for DP-QPSK and DP-16QAM transmissions but limits the AIRs for DP-64QAM and DP-256QAM transmissions. This study offers insights into the implementation and improvement of digital and optical NLC techniques in both EDFA and Raman-amplified fully-loaded $C-$band transmission systems, while considering the practical limitations of transceivers.

Additionally, the interplay between LPN and EDC module can lead to EEPN, which significantly degrades the performance of uncompensated long-haul coherent optical fibre communication systems. In Chapter 4 of the thesis, the analytical model has been built based on a GN model with consideration of the EEPN effects to predict the performance of multi-channel optical communication systems applied with EDC and digital NLC. The nonlinear interaction between the signal and EEPN is analysed, and numerical simulations are performed in nonlinear Nyquist-spaced WDM coherent transmission sys-

tems. The simulation results show significant performance degradation due to EEPN. When using NLC, a reduction of 1.41 dB in SNR was observed in a 32-GBd 2000-km 5-channel system due to EEPN. This reduction remained significant even when considering practical limits on TRx noise and PMD. The accuracy of the analytical model is validated by the numerical simulations for both lumped EDFA and backwards-pumped distributed Raman amplification. The impact of EEPN was found to increase substantially as the transmission distance increased as demonstrated by simulation results. The study also considers the effect of transmission symbol rate, with symbol rates of 16, 32, 64, and 128 GBd being examined. The results indicate that increasing symbol rates exacerbate the distortions. Additionally, the performance of the C-band transmission with different transmission symbol rates is evaluated based on the analytical estimation. The research expands the conventional GN model and emphasizes the significance of considering the impact of EEPN when designing and evaluating the performance of high-capacity, long-distance optical communication systems with significant laser linewidths. This study also offers valuable insights into the development of Nyquist-spaced WDM high-speed wideband nonlinear fibre systems for long-haul applications with notable LPN.

Chapter 4 involved a thorough examination of how EEPN effects affect nonlinear optical fibre systems through numerical simulations and analytical models. In Chapter 5, a comprehensive analysis was conducted to study the performance of KF-based estimators under realistic long-haul optical link conditions. The purpose was to gain important knowledge about using KF techniques to ensure high-quality signal recovery in the design of long-haul coherent optical fibre communication systems. The effectiveness of KF CPE in mitigating phase distortions caused by various factors, such as EEPN, LPN,

and fibre nonlinearity, has been thoroughly analysed. Numerical simulations were conducted on both dispersion-unmanaged and dispersion-managed nonlinear long-haul transmission systems, using both DP-QPSK and DP-16QAM. A VV estimator was used as a benchmark, and a BPS was employed for comparison in the QPSK systems. Additionally, the transmission performance was studied under reasonable TRx noise. The analysis of the results led to the following insights: the KF has a great capability for mitigating phase impairments and led to a significant improvement in system performance; the KF scheme outperformed the VV and PA scheme in both dispersion-unmanaged and dispersion-managed optical transmission systems, using DP-QPSK and DP-16QAM modulation formats, and this was observed for both NLC and LIN; joint application of the KF and the NLC led to a significant improvement in system performance, with the KF scheme achieving approximately $\sim$4 dB higher SNRs compared with the PA CPE in both the dispersion-unmanaged and dispersion-managed WDM DP-QPSK and DP-16QAM systems.

6.2 Future Work

Regardless of the research presented in this thesis on advanced modelling and signal processing in nonlinear coherent optical fibre systems, there are still many areas that require further investigation. Here, potential research directions for future exploration are outlined.

Firstly, the research presented in Chapter 3 provides an insightful analysis of the long-haul system performance in perspective of AIRs by analytical models. However, it would be valuable to extend this analysis in the remaining chapters by studying the system performance in terms of AIRs. Moreover, the

performance of various DSP techniques, such as constellation shaping, error correction coding, advanced machine learning and deep learning algorithms, can also be explored for improving the AIRs. These extensions can provide a more comprehensive understanding of the impact of nonlinear effects on the system performance and the potential solutions for mitigating these effects.

Secondly, while Chapter 4 investigates the impact of PMD on the performance of a 32-GHz Nyquist-spaced 5-channel DP-16QAM system, there are still many scenarios that can be further explored for advanced DSP and modelling of practical transmissions. Specifically, the interplay between PMD and the Kerr effect in systems influenced by significant LPN requires further investigation in more detail. Additionally, the effect of frequency offset on the system performance can be added to the consideration, and the impact of EEPN on distributed-Raman-amplified WDM systems can be further investigated. By studying these scenarios, a more comprehensive understanding of the effects of different impairments on system performance can be achieved.

Thirdly, it is worth noting that in Chapters 4 and 5, only systems employing the FF-NLC have been investigated. In future work, it would be beneficial to explore different bandwidths of NLC for practical applications.

Fourthly, the impact of dispersion slope has not been taken into account in Chapter 4 and 5. It is crucial to consider the effect of dispersion slope on the prediction accuracy of analytical models for wideband systems. The EEPN can be affected by dispersion slope in the performance of the outer channel. Therefore, it is recommended to investigate the impact of dispersion slope on the performance of the systems analyzed in these chapters.

Additionally, a further investigation of the KF-based estimator can also be conducted in 400-Gbps long-haul terrestrial and submarine optical commu-

nication systems, where the impact of EEPN and fibre nonlinearity are more significant.

Finally, the performance of different modulation formats, including higher-order QAM, can be studied in more detail. These modulation formats have been shown to provide higher spectral efficiency but can also be more sensitive to nonlinear effects. Therefore, it is important to investigate their performance in nonlinear coherent optical fibre systems.

Overall, the research on advanced modelling and signal processing in nonlinear coherent optical fibre systems is of significant importance for the development of high-speed optical communication systems. The research presented in this thesis provides valuable insights into the impact of both linear and nonlinear effects on the performance of optical communication systems and the potential solutions for mitigating these effects. However, there are still many areas that require further investigation, and the potential research directions outlined here can provide important contributions to the development of high-performance optical communication systems.

Reference

[1] J. Hecht, *City of light: the story of fiber optics*. Oxford University Press on Demand, 2004.

[2] K. C. Kao and G. A. Hockham, "Dielectric-fibre surface waveguides for optical frequencies," in *Proceedings of the Institution of Electrical Engineers*, vol. 113, pp. 1151–1158, IET, 1966.

[3] F. Kapron, D. B. Keck, and R. D. Maurer, "Radiation losses in glass optical waveguides," *Applied Physics Letters*, vol. 17, no. 10, pp. 423–425, 1970.

[4] T. Miya, Y. Terunuma, T. Hosaka, and T. Miyashita, "Ultimate low-loss single-mode fibre at 1.55? m," *Electronics Letters*, vol. 4, no. 15, pp. 106–108, 1979.

[5] Z. Alferov, "Double heterostructure lasers: early days and future perspectives," *IEEE Journal of Selected Topics in Quantum Electronics*, vol. 6, no. 6, pp. 832–840, 2000.

[6] I. Hayashi, M. Panish, P. Foy, and S. Sumski, "Junction lasers which operate continuously at room temperature," *Applied Physics Letters*, vol. 17, no. 3, pp. 109–111, 1970.

[7] G. P. Agrawal, "Optical communication: its history and recent progress," *Optics in our time*, pp. 177–199, 2016.

[8] "Cisco. cisco visual networking index: Forecast and methodology 2017-2022." `https://www.cisco.com/c/dam/m/en_us/network-intelligence/service-provider/digital-transformation/knowledge-network-webinars/pdfs/1213-business-services-ckn.pdf`, 2018.

[9] P. Bayvel, R. Maher, T. Xu, G. Liga, N. A. Shevchenko, D. Lavery, A. Alvarado, and R. I. Killey, "Maximizing the optical network capacity," *Philosophical Transactions of the Royal Society A: Mathematical, Physical and Engineering Sciences*, vol. 374, no. 2062, p. 20140440, 2016.

[10] "Cisco visual networking index: Forecast and methodology 2016-2021.(2017) http://www.cisco.com/c/en/us/solutions/collateral/service-provider/visual- networking-index-vni/complete-white-paper-c11-481360.html. high efficiency video coding (hevc) algorithms and architectures https://jvet.hhi.fraunhofer.," 2017.

[11] G. P. Agrawal, *Nonlinear Fiber Optics*. New York, USA: Academic Press, 2013.

[12] C. Jin, N. A. Shevchenko, Z. Li, S. Popov, Y. Chen, and T. Xu, "Nonlinear coherent optical systems in the presence of equalization enhanced phase noise," *Journal of Lightwave Technology*, vol. 39, no. 14, pp. 4646–4653, 2021.

[13] A. P. T. Lau, T. S. R. Shen, W. Shieh, and K.-p. Ho, "Equalization-enhanced phase noise for 100 Gb/s transmission and beyond with coherent detection," *Optics Express*, vol. 18, pp. 17239–17251, Aug. 2010.

[14] E. Temprana, E. Myslivets, B.-P. Kuo, L. Liu, V. Ataie, N. Alic, and S. Radic, "Overcoming kerr-induced capacity limit in optical fiber transmission," *Science*, vol. 348, no. 6242, pp. 1445–1448, 2015.

[15] T. Xu, N. A. Shevchenko, Y. Zhang, C. Jin, J. Zhao, and T. Liu, "Information rates in kerr nonlinearity limited optical fiber communication systems," *Optics Express*, vol. 29, no. 11, pp. 17428–17439, 2021.

[16] A. Bononi, R. Dar, M. Secondini, P. Serena, and P. Poggiolini, *Fiber nonlinearity and optical system performance*, pp. 287–351. Cham: Springer, 2020.

[17] A. Ellis, M. McCarthy, M. Al Khateeb, M. Sorokina, and N. Doran, "Performance limits in optical communications due to fiber nonlinearity," *Advances in Optics and Photonics*, vol. 9, no. 3, pp. 429–503, 2017.

[18] E. Ip and J. M. Kahn, "Digital equalization of chromatic dispersion and polarization mode dispersion," *Journal of Lightwave Technology*, vol. 25, no. 8, pp. 2033–2043, 2007.

[19] G. Colavolpe, T. Foggi, E. Forestieri, and M. Secondini, "Impact of phase noise and compensation techniques in coherent optical systems," *Journal of Lightwave Technology*, vol. 29, no. 18, pp. 2790–2800, 2011.

[20] B. Karanov, T. Xu, N. A. Shevchenko, D. Lavery, G. Liga, R. I. Killey, and P. Bayvel, "Digital nonlinearity compensation considering signal

spectral broadening effects in dispersion-managed systems," in *Optical Fiber Communication Conference*, p. W2A.58, 2018.

[21] G. P. Agrawal, *Fiber-optic communication systems*. Hoboken, NJ, USA: Wiley, 3rd ed., 2012.

[22] P. Poggiolini, G. Bosco, A. Carena, V. Curri, Y. Jiang, and F. Forghieri, "The GN-Model of fiber non-linear propagation and its applications," *Journal of Lightwave Technology*, vol. 32, pp. 694–721, Feb. 2014.

[23] P. Poggiolini and Y. Jiang, "Recent advances in the modeling of the impact of nonlinear fiber propagation effects on uncompensated coherent transmission systems," *Journal of Lightwave Technology*, vol. 35, pp. 458–480, Feb. 2017.

[24] P. Poggiolini, Y. Jiang, A. Carena, and F. Forghieri, *Enabling Technologies for High Spectral-efficiency Coherent Optical Communication Networks (Chapter 7)*. US: Wiley, 2016.

[25] P. Poggiolini, A. Carena, V. Curri, G. Bosco, and F. Forghieri, "Analytical modeling of nonlinear propagation in uncompensated optical transmission links," *IEEE Photonics Technology Letters*, vol. 23, pp. 742–744, Jun. 2011.

[26] A. Carena, G. Bosco, V. Curri, Y. Jiang, P. Poggiolini, and F. Forghieri, "EGN model of non-linear fiber propagation," *Optics Express*, vol. 22, pp. 16335–16362, Jun. 2014.

[27] P. Poggiolini, G. Bosco, A. Carena, V. Curri, Y. Jiang, and F. Forghieri, "A simple and effective closed-form GN model correction formula ac-

counting for signal non-Gaussian distribution," *Journal of Lightwave Technology*, vol. 33, no. 2, pp. 459–473, 2015.

[28] P. Poggiolini, "The GN model of non-linear propagation in uncompensated coherent optical systems," *Journal of Lightwave Technology*, vol. 30, pp. 3857–3879, Dec. 2012.

[29] P. Poggiolini, M. R. Zefreh, G. Bosco, F. Forghieri, and S. Piciaccia, "Accurate non-linearity fully-closed-form formula based on the gn/egn model and large-data-set fitting," in *Optical Fiber Communication Conference*, pp. M1I–4, Optica Publishing Group, 2019.

[30] L. Galdino, D. Semrau, M. Ionescu, A. Edwards, W. Pelouch, S. Desbruslais, J. James, E. Sillekens, D. Lavery, S. Barnes, *et al.*, "Study on the impact of nonlinearity and noise on the performance of high-capacity broadband hybrid raman-edfa amplified system," *Journal of Lightwave Technology*, vol. 37, no. 21, pp. 5507–5515, 2019.

[31] S. Burtsev, S. Searcy, and S. Tibuleac, "Experimental study of closed-form gn model using real-time m-qam transceivers with symbol rate up to 69 gbd," in *Optical Fiber Communication Conference*, pp. M4K–6, Optical Society of America, 2020.

[32] N. A. Kaliteevskiy, V. Ivanov, P. Sterlingov, J. Downie, S. Makovejs, and J. Hurley, "Transponder implementation penalty-accounted gaussian-noise-based performance modeling of fiber-optic transmission systems," *Journal of Lightwave Technology*, vol. 38, no. 8, pp. 2253–2261, 2020.

[33] L. Galdino, D. Semrau, D. Lavery, G. Saavedra, C. B. Czegledi, E. Agrell, R. I. Killey, and P. Bayvel, "On the limits of digital back-propagation

in the presence of transceiver noise," *Optics Express*, vol. 25, no. 4, pp. 4564–4578, 2017.

[34] D. Semrau, L. Galdino, R. I. Killey, and P. Bayvel, "The impact of transceiver noise on digital nonlinearity compensation," *Journal of Lightwave Technology*, vol. 36, pp. 695–702, Feb. 2018.

[35] D. Semrau, R. I. Killey, and P. Bayvel, "The gaussian noise model in the presence of inter-channel stimulated raman scattering," *Journal of Lightwave Technology*, vol. 36, no. 14, pp. 3046–3055, 2018.

[36] L. Szczecinski and A. Alvarado, *Bit-interleaved coded modulation: fundamentals, analysis and design*. John Wiley & Sons, 2015.

[37] D. Semrau, T. Xu, N. A. Shevchenko, M. Paskov, A. Alvarado, R. I. Killey, and P. Bayvel, "Achievable information rates estimates in optically amplified transmission systems using nonlinearity compensation and probabilistic shaping," *Optics Letters*, vol. 42, no. 1, pp. 121–124, 2017.

[38] M. Secondini, E. Forestieri, and G. Prati, "Achievable information rate in nonlinear WDM fiber-optic systems with arbitrary modulation formats and dispersion maps," *Journal of Lightwave Technology*, vol. 31, no. 23, pp. 3839–3852, 2013.

[39] T. Fehenberger, A. Alvarado, P. Bayvel, and N. Hanik, "On achievable rates for long-haul fiber-optic communications," *Optics Express*, vol. 23, no. 7, pp. 9183–9191, 2015.

[40] R.-J. Essiambre and R. W. Tkach, "Capacity trends and limits of optical communication networks," *Proceedings of the IEEE*, vol. 100, no. 5, pp. 1035–1055, 2012.

[41] P. P. Mitra and J. B. Stark, "Nonlinear limits to the information capacity of optical fibre communications," *Nature*, vol. 411, no. 6841, pp. 1027–1030, 2001.

[42] T. Xu, N. A. Shevchenko, D. Lavery, D. Semrau, G. Liga, A. Alvarado, R. I. Killey, and P. Bayvel, "Modulation format dependence of digital nonlinearity compensation performance in optical fibre communication systems," *Optics Express*, vol. 25, pp. 3311–3326, Feb. 2017.

[43] R. Dar and P. J. Winzer, "On the limits of digital back-propagation in fully loaded WDM systems," *IEEE Photonics Technology Letters*, vol. 28, no. 11, pp. 1253–1256, 2016.

[44] T. Xu, N. A. Shevchenko, B. Karanov, D. Lavery, L. Galdino, A. Alvarado, R. I. Killey, and P. Bayvel, "Nonlinearity compensation and information rates in fully-loaded C-band optical fibre transmission systems," in *2017 European Conference on Optical Communication (ECOC)*, pp. 1–3, IEEE, 2017.

[45] R. Maher, T. Xu, L. Galdino, M. Sato, A. Alvarado, K. Shi, S. J. Savory, B. C. Thomsen, R. I. Killey, and P. Bayvel, "Spectrally shaped DP-16QAM super-channel transmission with multi-channel digital back-propagation," *Scientific Reports*, vol. 5, p. 8214, 2015.

[46] A. Ellis, S. Le, M. Al-Khateeb, S. Turitsyn, G. Liga, D. Lavery, T. Xu, and P. Bayvel, "The impact of phase conjugation on the nonlinear-

shannon limit: The difference between optical and electrical phase conjugation," in *2015 IEEE Summer Topicals Meeting Series (SUM)*, pp. 209–210, IEEE, 2015.

[47] M. Stephens, M. Tan, I. Phillips, S. Sygletos, P. Harper, and N. J. Doran, "1 THz-bandwidth polarization-diverse optical phase conjugation of 10×114Gb/s DP-QPSK WDM signals," in *Optical Fiber Communication Conference*, pp. W3F–6, Optical Society of America, 2014.

[48] T. Umeki, T. Kazama, A. Sano, K. Shibahara, K. Suzuki, M. Abe, H. Takenouchi, and Y. Miyamoto, "Simultaneous nonlinearity mitigation in 92×180-Gbit/s PDM-16QAM transmission over 3840 km using PPLN-based guard-band-less optical phase conjugation," *Optics Express*, vol. 24, no. 15, pp. 16945–16951, 2016.

[49] S. J. Savory, "Digital filters for coherent optical receivers," *Optics Express*, vol. 16, pp. 804–817, Jan. 2008.

[50] L. Beygi, N. V. Irukulapati, E. Agrell, P. Johannisson, M. Karlsson, H. Wymeersch, P. Serena, and A. Bononi, "On nonlinearly-induced noise in single-channel optical links with digital backpropagation," *Optics Express*, vol. 21, no. 22, pp. 26376–26386, 2013.

[51] D. Rafique and A. D. Ellis, "Impact of signal-ase four-wave mixing on the effectiveness of digital back-propagation in 112 Gb/s PM-QPSK systems," *Optics Express*, vol. 19, no. 4, pp. 3449–3454, 2011.

[52] C. Fougstedt, L. Svensson, M. Mazur, M. Karlsson, and P. Larsson-Edefors, "ASIC implementation of time-domain digital back propaga-

tion for coherent receivers," *IEEE Photonics Technology Letters*, vol. 30, no. 13, pp. 1179–1182, 2018.

[53] J. C. Cartledge, F. P. Guiomar, F. R. Kschischang, G. Liga, and M. P. Yankov, "Digital signal processing for fiber nonlinearities [Invited]," *Optics Express*, vol. 25, pp. 1916–1936, Feb. 2017.

[54] A. J. Viterbi and A. M. Viterbi, "Nonlinear estimation of psk-modulated carrier phase with application to burst digital transmission," *IEEE Transactions on Information Theory*, vol. 29, no. 4, pp. 543–551, 1983.

[55] S. T. Le, P. A. Haigh, A. D. Ellis, and S. K. Turitsyn, "Blind phase noise estimation for co-ofdm transmissions," *Journal of Lightwave Technology*, vol. 34, no. 2, pp. 745–753, 2016.

[56] T. Pfau, S. Hoffmann, and R. Noé, "Hardware-efficient coherent digital receiver concept with feedforward carrier recovery for M-QAM constellations," *Journal of Lightwave Technology*, vol. 27, no. 8, pp. 989–999, 2009.

[57] D. A. Mello, F. A. Barbosa, and J. D. Reis, "Interplay of probabilistic shaping and the blind phase search algorithm," *Journal of Lightwave Technology*, vol. 36, no. 22, pp. 5096–5105, 2018.

[58] X. Zhou, C. Lu, A. P. T. Lau, and K. Long, "Low-complexity carrier phase recovery for square M-QAM based on S-BPS algorithm," *IEEE Photonics Technology Letters*, vol. 26, no. 18, pp. 1863–1866, 2014.

[59] X. Zhou, K. Zhong, Y. Gao, C. Lu, A. P. T. Lau, and K. Long, "Modulation-format-independent blind phase search algorithm for co-

herent optical square M-QAM systems," *Optics Express*, vol. 22, no. 20, p. 24044, 2014.

[60] J. R. Navarro, A. Kakkar, R. Schatz, X. Pang, O. Ozolins, A. Udalcovs, S. Popov, and G. Jacobsen, "Blind phase search with angular quantization noise mitigation for efficient carrier phase recovery," *Photonics*, vol. 4, no. 2, 2017.

[61] A. Kakkar, J. R. Navarro, R. Schatz, H. Louchet, X. Pang, O. Ozolins, G. Jacobsen, and S. Popov, "Comprehensive study of equalization-enhanced phase noise in coherent optical systems," *Journal of Lightwave Technology*, vol. 33, pp. 4834–4841, Dec. 2015.

[62] W. Shieh and K.-P. Ho, "Equalization-enhanced phase noise for coherent-detection systems using electronic digital signal processing," *Optics Express*, vol. 16, p. 15718, Sept. 2008.

[63] A. Arnould and A. Ghazisaeidi, "Equalization enhanced phase noise in coherent receivers: DSP-aware analysis and shaped constellations," *Journal of Lightwave Technology*, vol. 37, pp. 5282–5290, Oct. 2019.

[64] J. Ding, T. Xu, Y. Zhang, Z. Liu, C. Jin, J. Zhao, and T. Liu, "Influence of equalization enhanced phase noise on digital nonlinearity compensation in nyquist-spaced superchannel transmission systems," in *Semiconductor Lasers and Applications XI*, vol. 11891, pp. 38–45, SPIE, 2021.

[65] P. Qin, C. Bai, H. Xu, L. Yang, W. Sun, X. Yu, X. Lv, X. Tang, Y. Bi, and X. Luo, "Analysis and compensation of equalization-enhanced phase noise in carrier assisted differential detection system," in *Asia Commun. Photonics Conf.*, pp. W4B–3, OSA, 2021.

[66] M. A. Z. Al-Khateeb, M. McCarthy, C. Sánchez, and A. Ellis, "Effect of second order signal–noise interactions in nonlinearity compensated optical transmission systems," *Optics Letters*, vol. 41, no. 8, pp. 1849–1852, 2016.

[67] N. A. Shevchenko, T. Xu, D. Lavery, G. Liga, D. J. Ives, R. I. Killey, and P. Bayvel, "Modeling of nonlinearity-compensated optical communication systems considering second-order signal-noise interactions," *Optics Letters*, vol. 42, no. 17, pp. 3351–3354, 2017.

[68] R. Dar, M. Feder, A. Mecozzi, and M. Shtaif, "Inter-channel nonlinear interference noise in wdm systems: modeling and mitigation," *Journal of Lightwave Technology*, vol. 33, no. 5, pp. 1044–1053, 2014.

[69] A. Carena, V. Curri, G. Bosco, P. Poggiolini, and F. Forghieri, "Modeling of the impact of nonlinear propagation effects in uncompensated optical coherent transmission links," *Journal of Lightwave Technology*, vol. 30, no. 10, pp. 1524–1539, 2012.

[70] R. Dar, M. Feder, A. Mecozzi, and M. Shtaif, "Properties of nonlinear noise in long, dispersion-uncompensated fiber links," *Optics Express*, vol. 21, no. 22, pp. 25685–25699, 2013.

[71] R. Dar, M. Feder, A. Mecozzi, and M. Shtaif, "Accumulation of nonlinear interference noise in fiber-optic systems," *Optics Express*, vol. 22, no. 12, pp. 14199–14211, 2014.

[72] K.-P. Ho, A. P. T. Lau, and W. Shieh, "Equalization-enhanced phase noise induced timing jitter," *Optics Letters*, vol. 36, pp. 585–587, Feb. 2011.

[73] K.-P. Ho and W. Shieh, "Equalization-enhanced phase noise in mode-division multiplexed systems," *Journal of Lightwave Technology*, vol. 31, pp. 2237–2243, Jul. 2013.

[74] T. Xu, G. Jacobsen, S. Popov, J. Li, S. Sergeyev, A. T. Friberg, T. Liu, and Y. Zhang, "Analysis of chromatic dispersion compensation and carrier phase recovery in long-haul optical transmission system influenced by equalization enhanced phase noise," *Optik*, vol. 138, pp. 494–508, Jun. 2017.

[75] A. Jain and P. K. Krishnamurthy, "Phase noise tracking and compensation in coherent optical systems using kalman filter," *IEEE Communications Letters*, vol. 20, no. 6, pp. 1072–1075, 2016.

[76] L. Pakala and B. Schmauss, "Extended kalman filtering for joint mitigation of phase and amplitude noise in coherent qam systems," *Optics Express*, vol. 24, pp. 6391–6401, Mar 2016.

[77] Q. Zhang, N. Cui, X. Li, X. Zhang, and L. Xi, "Kalman filter polarization demultiplexing algorithm based on diagonalized matrix treatment," *Optics Express*, vol. 30, no. 2, pp. 2803–2816, 2022.

[78] K. Shibahara, T. Mizuno, and Y. Miyamoto, "Mimo carrier phase recovery for carrier-asynchronous sdm-mimo reception based on the extended kalman filter," *Optics Express*, vol. 29, no. 11, pp. 17111–17124, 2021.

[79] N. Zhang, W. Yi, Z. Zheng, N. Cui, R. Guo, L. Qiu, X. Zhang, L. Xi, W. Zhang, and H. Xu, "Joint equalization of linear impairments using two-stage cascade kalman filter structure in coherent optical communication systems," *Optics Communications*, vol. 453, p. 124398, 2019.

[80] G. Huang, D. Wu, J. Luo, Y. Huang, and Y. Shen, "Retrieving the optical transmission matrix of a multimode fiber using the extended Kalman filter," *Optics Express*, vol. 28, no. 7, pp. 9487–9500, 2020.

[81] Y. Liu, Y. Li, H. Zhou, Z. Zhao, L. Yue, H. Guo, J. Qiu, X. Hong, W. Li, Y. Zuo, and J. Wu, "Performance analysis of extended kalman filter in kramers-kronig receiver," in *OECC/PSC*, pp. 1–3, 2019.

[82] T. T. Nguyen, S. T. Le, T. Yakusheva, and P. MÉGRET, "Simplified extended kalman filter phase noise estimation for co-ofdm transmissions," *Optics Express*, vol. 25, no. 22, pp. 6391–6401, 2017.

[83] T. Inoue and S. Namiki, "Carrier recovery for M-QAM signals based on a block estimation process with Kalman filter," *Optics Express*, vol. 22, no. 13, p. 15376, 2014.

[84] T. Marshall, B. Szafraniec, and B. Nebendahl, "Kalman filter carrier and polarization-state tracking," *Optics Letters*, vol. 35, no. 13, p. 2203, 2010.

[85] J. Jignesh, B. Corcoran, C. Zhu, and A. Lowery, "Unscented kalman filters for polarization state tracking and phase noise mitigation," *Optics Express*, vol. 24, no. 19, pp. 22282–22295, 2016.

[86] Y. Yang, G. Cao, K. Zhong, X. Zhou, Y. Yao, A. P. T. Lau, and C. Lu, "Fast polarization-state tracking scheme based on radius-directed linear Kalman filter," *Optics Express*, vol. 23, no. 15, p. 19673, 2015.

[87] R. E. Kalman, "A new approach to linear filtering and prediction problems," *Transactions of the ASME: Journal of Basic Engineering*, vol. 82, no. 1, pp. 35–45, 1960.

[88] C. Jin, M. Tan, N. A. Shevchenko, Z. Liu, Z. Li, S. Popov, Y. Chen, and T. Xu, "High-speed long-haul multi-channel nonlinear optical communication systems influenced by equalization enhanced phase noise," in *2022 IEEE 14th International Conference on Advanced Infocomm Technology (ICAIT)*, pp. 103–106, IEEE, 2022.

[89] C. Jin, N. A. Shevchenko, J. Wang, Y. Chen, and T. Xu, "Wideband multichannel nyquist-spaced long-haul optical transmission influenced by enhanced equalization phase noise," *Sensors*, vol. 23, no. 3, p. 1493, 2023.

[90] C. Jin, M. Tan, Y. Chen, and T. Xu, "Kalman filter based impairment mitigation in nonlinear optical systems with equalization enhanced phase noise," in *2022 IEEE Photonics Conference (IPC)*, pp. 1–2, IEEE, 2022.

[91] Benedetto, Sergio and Biglieri, Ezio, *Principles of digital transmission: with wireless applications*. Springer Science & Business Media, 1999.

[92] K. Kikuchi, T. Okoshi, and J. Kitano, "Measurement of bit-error rate of heterodyne-type optical communication system-a simulation experiment," *IEEE Journal of Quantum Electronics*, vol. 17, no. 12, pp. 2266–2267, 1981.

[93] C. Behrens, *Mitigation of nonlinear impairments for advanced optical modulation formats*. PhD thesis, UCL (University College London), 2012.

[94] R. Olshansky, "Noise figure for erbium-doped optical fibre amplifiers," *Electronics Letters*, vol. 24, pp. 1363–1365, 1988.

[95] R. Laming and D. Payne, "Noise characteristics of erbium-doped fibre amplifier pumped at 980nm," *IEEE Photonics Technology Letters*, vol. 2, no. 6, pp. 418–421, 1990.

[96] K. Kikuchi, "Generalised formula for optical-amplifier noise and its application to erbium-doped fibre amplifiers," *Electronics Letters*, vol. 22, no. 26, pp. 1851–1853, 1990.

[97] A. Yariv, "Signal-to-noise considerations in fiber links with periodic or distributed optical amplification," *Optics Letters*, vol. 15, no. 19, pp. 1064–1066, 1990.

[98] H. Kogelnik and A. Yariv, "Considerations of noise and schemes for its reduction in laser amplifiers," *Proceedings of the IEEE*, vol. 52, no. 2, pp. 165–172, 1964.

[99] J. Bromage, "Raman amplification for fiber communications systems," *Journal of Lightwave Technology*, vol. 22, no. 1, pp. 79–93, 2004.

[100] Wai, P.K.A. and Menyak, C.R., "Polarization mode dispersion, decorrelation, and diffusion in optical fibers with randomly varying birefringence," *Journal of Lightwave Technology*, vol. 14, no. 2, pp. 148–157, 1996.

[101] H. Kogelnik, R. M. Jopson, and L. E. Nelson, "Polarization-mode dispersion," in *Optical Fiber Telecommunications IV-B*, pp. 725–861, Elsevier, 2002.

[102] D. Marcuse, C. R. Manyuk, and P. K. A. Wai, "Application of the Manakov-PMD equation to studies of signal propagation in optical fibers with randomly varying birefringence," *Journal of Lightwave Technology*, vol. 15, pp. 1735–1746, Sept. 1997.

[103] K. Petermann, *Laser diode modulation and noise*, vol. 3. Springer Science & Business Media, 1991.

[104] U. Madhow, *Fundamentals of digital communication*. Cambridge university press, 2008.

[105] C. Henry, "Theory of the linewidth of semiconductor lasers," *IEEE Journal of Quantum Electronics*, vol. 18, no. 2, pp. 259–264, 1982.

[106] S. Bennetts, G. D. McDonald, K. S. Hardman, J. E. Debs, C. C. Kuhn, J. D. Close, and N. P. Robins, "External cavity diode lasers with 5khz linewidth and 200nm tuning range at 1.55 μm and methods for linewidth measurement," *Optics Express*, vol. 22, no. 9, pp. 10642–10654, 2014.

[107] B. J. Puttnam, R. Luis, J.-M. Delgado-Mendinueta, J. Sakaguchi, W. Klaus, Y. Awaji, N. Wada, A. Kanno, and T. Kawanishi, "High-capacity self-homodyne pdm-wdm-sdm transmission in a 19-core fiber," *Optics Express*, vol. 22, no. 18, pp. 21185–21191, 2014.

[108] T. Xu, G. Liga, D. Lavery, B. C. Thomsen, S. J. Savory, R. I. Killey, and P. Bayvel, "Equalization enhanced phase noise in Nyquist-spaced superchannel transmission systems using multi-channel digital back-propagation," *Scientific Reports*, vol. 5, p. 13990, Sept. 2015.

[109] G. Jacobsen, M. Lidón, T. Xu, S. Popov, A. T. Friberg, and Y. Zhang, "Influence of pre- and post-compensation of chromatic dispersion on equalization enhanced phase noise in coherent multilevel systems," *Journal of Optical Communications*, vol. 32, pp. 257–261, Dec. 2011.

[110] R. H. Hardin, "Application of the split-step fourier method to the numerical solution of nonlinear and variable coefficient wave equations," *Siam Review*, vol. 15, p. 423, 1973.

[111] T. R. Taha, "A numerical scheme for the nonlinear schrödinger equation," *Computers & Mathematics with Applications*, vol. 22, no. 9, pp. 77–84, 1991.

[112] G. H. Weiss and A. A. Maradudin, "The baker-hausdorff formula and a problem in crystal physics," *Journal of Mathematical Physics*, vol. 3, no. 4, pp. 771–777, 1962.

[113] J. A. Fleck, J. Morris, and M. Feit, "Time-dependent propagation of high energy laser beams through the atmosphere," *Applied physics*, vol. 10, pp. 129–160, 1976.

[114] X. Li and E. al, "Electronic post-compensation of WDM transmission impairments using coherent detection and digital signal processing," *Optics Express*, vol. 16, no. 2, pp. 880–888, 2008.

[115] W. Shieh, H. Bao, and Y. Tang, "Coherent optical OFDM: theory and design," *Optics Express*, vol. 16, no. 2, pp. 841–859, 2008.

[116] W. Jiang, Y. Yang, Q. Zhang, Y. Sun, K. Zhong, X. Zhou, and Y. Yao, "Application of kalman filter in frequency offset estimation for coherent

optical quadrature phase-shift keying communication system," *Optical Engineering*, vol. 55, no. 9, p. 096102, 2016.

[117] S. Zhang, P. Y. Kam, C. Yu, and J. Chen, "Frequency offset estimation using a kalman filter in coherent optical phase-shift keying systems," in *Conference on Lasers and Electro-Optics*, p. CThDD4, Optica Publishing Group, 2010.

[118] L. Pessoa, H. Salgado, and I. Darwazeh, "Efficient implementation of a phase estimation algorithm in coherent optical systems," *IEEE LEOS, STM*, pp. 1–3, 2008.

[119] D. Zibar, L. H. H. de Carvalho, M. Piels, A. Doberstein, J. Diniz, B. Nebendahl, C. Franciscangelis, J. Estaran, H. Haisch, N. G. Gonzalez, *et al.*, "Application of machine learning techniques for amplitude and phase noise characterization," *Journal of Lightwave Technology*, vol. 33, no. 7, pp. 1333–1343, 2015.

[120] B. Szafraniec, T. S. Marshall, and B. Nebendahl, "Performance monitoring and measurement techniques for coherent optical systems," *Journal of Lightwave Technology*, vol. 31, no. 4, pp. 648–663, 2012.

[121] L. Pakala and B. Schmauss, "Joint compensation of frequency offset, phase and amplitude noise using two stage extended kalman filtering," in *Photonic Networks; 18. ITG-Symposium*, pp. 1–4, 2017.

[122] G. Bosco, P. Poggiolini, A. Carena, V. Curri, and F. Forghieri, "Analytical results on channel capacity in uncompensated optical links with coherent detection," *Optics Express*, vol. 19, no. 26, pp. B440–B451, 2011.

[123] W. Zeiler, F. Di Pasquale, P. Bayvel, and J. E. Midwinter, "Modeling of four-wave mixing and gain peaking in amplified wdm optical communication systems and networks," *Journal of Lightwave Technology*, vol. 14, no. 9, pp. 1933–1942, 1996.

[124] R. E. Caflisch *et al.*, "Monte Carlo and quasi-Monte Carlo methods," *Acta numerica*, vol. 1998, pp. 1–49, 1998.

[125] T. Tanimura, M. Nölle, J. K. Fischer, and C. Schubert, "Analytical results on back propagation nonlinear compensator with coherent detection," *Optics Express*, vol. 20, no. 27, pp. 28779–28785, 2012.

[126] D. Lavery, D. Ives, G. Liga, A. Alvarado, S. J. Savory, and P. Bayvel, "The benefit of split nonlinearity compensation for single channel optical fiber communications," in *2016 IEEE Photonics Conference (IPC)*, pp. 799–802, IEEE, 2016.

[127] N. A. Shevchenko, T. Xu, D. Semrau, G. Saavedra, G. Liga, M. Paskov, L. Galdino, A. Alvarado, R. I. Killey, and P. Bayvel, "Achievable information rates estimation for 100-nm Raman-amplified optical transmission system," in *ECOC 2016; 42nd European Conference on Optical Communication*, pp. 1–3, VDE, 2016.

[128] D. Zwillinger and A. Jeffrey, *Table of integrals, series, and products*. Elsevier, 2007.

[129] D. F. Semrau, *Physical layer modelling of optical fibre communication systems in the nonlinear regime*. PhD thesis, UCL (University College London), 2020.

[130] P. Johannisson and M. Karlsson, "Perturbation analysis of nonlinear propagation in a strongly dispersive optical communication system," *Journal of Lightwave Technology*, vol. 31, no. 8, pp. 1273–1282, 2013.

[131] K. Shi, E. Sillekens, and B. C. Thomsen, "246 ghz digitally stitched coherent receiver," in *Optical Fiber Communication Conference*, pp. M3D–3, Optical Society of America, 2017.

[132] R.-J. Essiambre and R. W. Tkach, "Capacity trends and limits of optical communication networks," *Proceedings of the IEEE*, vol. 100, no. 5, pp. 1035–1055, 2012.

[133] D. Rafique, M. Mussolin, M. Forzati, J. Mårtensson, M. N. Chugtai, and A. D. Ellis, "Compensation of intra-channel nonlinear fibre impairments using simplified digital back-propagation algorithm," *Optics Express*, vol. 19, no. 10, pp. 9453–9460, 2011.

[134] G. Liga, A. Alvarado, E. Agrell, and P. Bayvel, "Information rates of next-generation long-haul optical fiber systems using coded modulation," *Journal of Lightwave Technology*, vol. 35, no. 1, pp. 113–123, 2016.

[135] A. Alvarado and E. Agrell, "Four-dimensional coded modulation with bit-wise decoders for future optical communications," *Journal of Lightwave Technology*, vol. 33, no. 10, pp. 1993–2003, 2015.

[136] A. Alvarado, T. Fehenberger, B. Chen, and F. M. Willems, "Achievable information rates for fiber optics: Applications and computations," *Journal of Lightwave Technology*, vol. 36, no. 2, pp. 424–439, 2017.

[137] H. Hu, R. Jopson, A. Gnauck, M. Dinu, S. Chandrasekhar, C. Xie, and S. Randel, "Parametric amplification, wavelength conversion, and phase conjugation of a 2.048-tbit/s wdm pdm 16-qam signal," *Journal of Lightwave Technology*, vol. 33, no. 7, pp. 1286–1291, 2015.

[138] H. Hu, R. M. Jopson, A. H. Gnauck, S. Randel, and S. Chandrasekhar, "Fiber nonlinearity mitigation of WDM-PDM QPSK/16-QAM signals using fiber-optic parametric amplifiers based multiple optical phase conjugations," *Optics Express*, vol. 25, no. 3, pp. 1618–1628, 2017.

[139] B. Karanov, T. Xu, N. A. Shevchenko, D. Lavery, R. I. Killey, and P. Bayvel, "Span length and information rate optimisation in optical transmission systems using single-channel digital backpropagation," *Optics Express*, vol. 25, no. 21, pp. 25353–25362, 2017.

[140] P. Rosa, S. T. Le, G. Rizzelli, M. Tan, and J. D. Ania-Castanón, "Signal power asymmetry optimisation for optical phase conjugation using raman amplification," *Optics Express*, vol. 23, no. 25, pp. 31772–31778, 2015.

[141] P. Rosa, G. Rizzelli, and J. D. Ania-Castañón, "Link optimization for dwdm transmission with an optical phase conjugation," *Optics Express*, vol. 24, no. 15, pp. 16450–16455, 2016.

[142] G. Rizzelli, P. Rosa, P. Corredera, and J. D. Ania-Castañón, "Transmission span optimization in fiber systems with cavity and random distributed feedback ultralong raman laser amplification," *Journal of Lightwave Technology*, vol. 35, no. 22, pp. 4967–4972, 2017.

[143] G. Bosco, A. Carena, V. Curri, R. Gaudino, P. Poggiolini, and S. Benedetto, "Suppression of spurious tones induced by the split-step method in fiber systems simulation," *IEEE Photonics Technology Letters*, vol. 12, pp. 489–491, May 2000.

[144] E. Ip and J. M. Kahn, "Compensation of dispersion and nonlinear impairments using digital backpropagation," *Journal of Lightwave Technology*, vol. 26, no. 20, pp. 3416–3425, 2008.

[145] F. Chang, K. Onohara, and T. Mizuochi, "Forward error correction for 100 G transport networks," *IEEE Communications Magazine*, vol. 48, pp. S48–S55, Mar. 2010.

[146] "ECL, DFB, VHG-Stabilized, DBR, and Hybrid Single-Frequency Lasers." accessed 13-August-2020.

[147] M. P. Paskov, *Algorithms and Subsystems for Next Generation Optical Networks*. PhD thesis, University College London, London, UK, 2015.

[148] C. B. Czegledi, G. Liga, D. Lavery, M. Karlsson, E. Agrell, S. J. Savory, and P. Bayvel, "Polarization-mode dispersion aware digital backpropagation," in *ECOC 2016; 42nd European Conference on Optical Communication*, pp. 1–3, VDE, 2016.

[149] C. B. Czegledi, G. Liga, D. Lavery, M. Karlsson, E. Agrell, S. J. Savory, and P. Bayvel, "Digital backpropagation accounting for polarization-mode dispersion," *Optics Express*, vol. 25, no. 3, pp. 1903–1915, 2017.

[150] Q. Zhang and C. Shu, "Viterbi and Viterbi Algorithm based Phase Recovery for Probabilistically Shaped Signals," *Journal of Lightwave Technology*, vol. 39, no. 5, pp. 1364–1370, 2021.

[151] T. Xu, G. Jacobsen, S. Popov, J. Li, A. T. Friberg, and Y. Zhang, "Carrier phase estimation methods in coherent transmission systems influenced by equalization enhanced phase noise," *Optics Communications*, vol. 293, pp. 54–60, 2013.

[152] I. Fatadin, D. Ives, and S. J. Savory, "Laser linewidth tolerance for 16-qam coherent optical systems using qpsk partitioning," *IEEE Photonics Technology Letters*, vol. 22, no. 9, pp. 631–633, 2010.

[153] M. Nakamura, Y. Kamio, and T. Miyazaki, "Pilot-carrier based linewidth-tolerant 8psk self-homodyne using only one modulator," in *33rd European Conference and Exhibition of Optical Communication*, pp. 1–2, 2007.

[154] S. L. Jansen, I. Morita, N. Takeda, and H. Tanaka, "20-Gb/s OFDM transmission over 4,160-km SSMF enabled by RF-pilot tone phase noise compensation," in *Optical Fiber Communication Conference and Exposition and The National Fiber Optic Engineers Conference*, p. PDP15, Optica Publishing Group, 2007.

[155] M. Nakamura, Y. Kamio, and T. Miyazaki, "Linewidth-tolerant 10-Gbit/s 16-QAM transmission using a pilot-carrier based phase-noise cancelling technique," *Optics Express*, vol. 16, no. 14, pp. 10611–10616, 2008.

[156] G. Jacobsen, T. Xu, S. Popov, J. Li, A. T. Friberg, and Y. Zhang, "Receiver implemented RF pilot tone phase noise mitigation in coherent optical nPSK and nQAM systems," *Optics Express*, vol. 19, no. 15, pp. 14487–14494, 2011.

[157] X. Liu, A. Chraplyvy, P. Winzer, R. Tkach, and S. Chandrasekhar, "Phase-conjugated twin waves for communication beyond the kerr nonlinearity limit," *Nature Photonics*, vol. 7, no. 7, pp. 560–568, 2013.

[158] X. Liu, S. Chandrasekhar, P. J. Winzer, R. W. Tkach, and A. R. Chraplyvy, "Fiber-nonlinearity-tolerant superchannel transmission via nonlinear noise squeezing and generalized phase-conjugated twin waves," *Journal of Lightwave Technology*, vol. 32, no. 4, pp. 766–775, 2014.

[159] J. Yang, E. Sillekens, W. Yi, P. Bayvel, and R. I. Killey, "Joint estimation of dynamic polarization and carrier phase with pilot-based adaptive equalizer in PDM-64 QAM transmission system," *Optics Express*, vol. 29, no. 26, pp. 43136–43147, 2021.

[160] D. J. Elson, G. Saavedra, K. Shi, D. Semrau, L. Galdino, R. Killey, B. C. Thomsen, and P. Bayvel, "Investigation of bandwidth loading in optical fibre transmission using amplified spontaneous emission noise," *Optics Express*, vol. 25, no. 16, pp. 19529–19537, 2017.

[161] A. Ghazisaeidi, "A theory of nonlinear interactions between signal and amplified spontaneous emission noise in coherent wavelength division multiplexed systems," *Journal of Lightwave Technology*, vol. 35, no. 23, pp. 5150–5175, 2017.